Millimetre wave devices for high frequency mobile, space and IoT applications

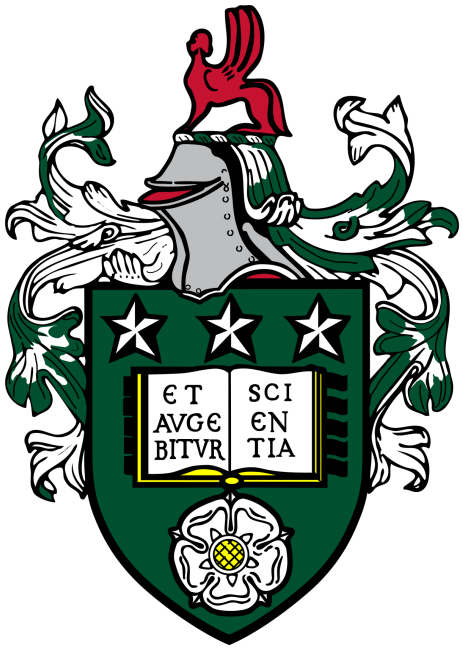

Giorgos Savvides

Submitted in accordance with the requirements for the degree of
Doctor of Philosophy

University of Leeds
School of Electrical and Electronic Engineering
May 2023

Abstract

In this thesis, Hollow Substrate Integrated Waveguides (HSIW) for microwave and millimetre-wave applications are thoroughly analyzed and investigated. New millimetre wave device fabrication techniques, a new HSIW transmission line, and a curved HSIW structure are all presented. The three previously published journals that form the basis of the thesis, make major contributions to the field of HSIW technology. An innovative technique for constructing HSIWs using a cheap, readily available material and a streamlined production process is covered in the first journal paper. The article outlines a step-by-step fabrication process and assesses the HSIW structures' performance in terms of bandwidth, insertion loss, and return loss.

Later on, the new HSIW structure is analyzed and it shown that, it offers considerable benefits over standard HSIWs in terms of performance characteristics, including propagation loss and bandwidth. It is based on the manufacturing approach discussed previously. The thesis presents the novel HSIW structure's design, manufacturing, performance assessment and a comparison to other existing HSIWs.

After the straight sections presentation, the design, production and performance assessment of a novel curved HSIW structure are analyzed. This structure has a number of possible uses in microwave and millimetre-wave systems. In terms of performance characteristics, the thesis contrasts the curved HSIW structure's performance with that of previously designed straight section HSIW structures.

The thesis in overall, provides a comprehensive review of the fundamental concepts and design principles of HSIWs, including their electromagnetic characteristics, propagation modes, and transmission properties. The research presented in this thesis can contribute to the development of advanced HSIW-based devices and systems for high-frequency communication and other emerging applications. In conclusion, this thesis presents significant contributions to the field of HSIW technology, drawing on three previously published journal articles and a comprehensive investigation of HSIWs' fundamental concepts, design principles, and potential applications.

Publications

0.1 Thesis Rationale and Brief Summary

This thesis is submitted as an alternative style of doctoral thesis including published material. This format is appropriate for the thesis because two out of the three data chapters have already been published in peer-reviewed journals, and a third is currently in review. There is one chapter for each of the three manuscripts, therefore Chapter 2,3 and 4 include the published material. The three manuscripts are preceded by an introduction (Chapter 1), which includes a review of the literature to give context to the work, the rationale for the project and an outline of the main research questions. The novelty of the research will also be highlighted here. A discussions section (Chapter 5) follows the research articles, and weaves together the findings of all three manuscripts, placing them in the context of the literature and providing further in-depth critical analysis. Overarching conclusions from the work are also included in this section. This format adheres to the Faculty of Engineering and Physical Sciences (School of Electronic and Electrical Engineering) protocol for the format and presentation of an alternative style of doctoral thesis including published material.

0.2 List of Publications and author contributions

Chapter 2 : Harmonized Rapid Prototyping of Millimeter-Wave Components Using Additive and Subtractive Manufacturing. Nonchanutt Chudpooti, Member, IEEE, Giorgos Savvides, Nattapong Duangrit, Member, IEEE, Prayoot Akkaraekthalin, Member, IEEE, Ian D. Robertson, Fellow, IEEE, and Nutapong Somjit, Senior Member, IEEE Published in IEEE TRANSACTIONS ON COMPONENTS, PACKAGING AND MANUFACTURING TECHNOLOGY

GS (candidate) has fabricated samples to prove the working principle and the feasibility of fabricating materials by using Additive and Subtractive manufacturing. The GS (candidate) conducted all the data analysis and made the figures and wrote

the manuscript. NC, ND, PA helped with guidance in measurements setup as well manuscript modifications. NS provided training in how to use the spectrum analyser and helped guide the process. IR provided advice and guidance throughout and gave feedback on several drafts of the manuscript.

Chapter 3: 3D Rapid-Prototyped 21-31-GHz Hollow SIWs for Low-Cost 5G IoT and Robotic Applications GIORGOS SAVVIDES, NATTAPONG DUANGRIT, (Member, IEEE), NONCHANUTT CHUDPOOTI, (Member, IEEE), PRAYOOT AKKARAEKTHALIN, (Member, IEEE), ULRIK IMBERG, IAN D. ROBERTSON, (Fellow, IEEE), AND NUTAPONG SOMJIT, (Senior Member, IEEE) Published in IEEE ACCESS

GS (candidate) has fabricated samples to prove the working principle and has done the measurements that proof that the specific HSIW is a good candidate for 5G and IoT applications, based on the performance obtained. GS (candidate) conducted all the data analysis and made the figures and wrote the manuscript. NC, ND, PA, UI helped with guidance in measurements setup as well manuscript modifications. NS provided training in how to use the spectrum analyser and helped guide the process. IR provided advice and guidance throughout and gave feedback on several drafts of the manuscript.

Chapter 4: 22-32-GHz Curved Hollow SIWs for Advanced Millimeter-Wave Applications GIORGOS SAVVIDES,NONCHANUTT CHUDPOOTI, JOACHIM OBERHAMMER, IAN D. ROBERTSON and NUTAPONG SOMJIT Under Review in IEEE ACCESS

GS (candidate) has fabricated samples to prove the working principle and has done the measurements that proof that the specific curved HSIW is a good candidate for 5G and IoT applications, based on the performance obtained. GS (candidate) conducted all the data analysis and made the figures and wrote the manuscript. NC, JO helped with guidance in measurements setup as well manuscript modifications. NS provided training in how to use the spectrum analyser and helped guide the process. IR provided advice and guidance throughout and gave feedback on several drafts of the manuscript.

Acknowledgements

Firstly I want to thank my supervisors, Nutapong Somjit and Ian Robertson, for their critical insights, encouragement, and skilled support over the past four years. And of course, this PhD could not be feasible without the EPSRC (DTP) scholarship.

Nick Sulollari and Viktor Doychinov, were particularly helpful to me through various writing processes and provided lab support when required. I learned a lot from each of you and appreciate your support. Thanks to all my colleagues and friends in the School of Electronic Engineering and at the University of Leeds.

I'm grateful for the support I've received from my friends and loved ones. Thanks to my family, for always being there at the end of the phone with love, support, and belief in me. And thanks to all the rest of my friends for keeping me grounded and encouraging me along the way.

Thanks, Philokypros Ioulianou, Stephanie Perdiou and all my other close friends who encouraged working on the PhD thesis writing when I was procrastinating and made me relax when I'd been working too much, and generally helped keep me sane!

And finally I would like to thank Kyveli Napoleontos and her family. I can't thank you enough for your care, support, understanding, and love. You have been there when I've needed you most.

Declaration

The candidate confirms that the work submitted is her own and that appropriate credit has been given where reference has been made to the work of others. This copy has been supplied on the understanding that it is copyright material and that no quotation from this work may be published without proper acknowledgement.

List of Figures

List of Tables

List of Abbreviations

WLAN - Wireless Local Area Network

1G - First Generation Mobile Network

FDMA - Frequency Division Multiple Access

2G - Second Generation Mobile Network

GSM - Global System for Mobile Communications

SMS - Short Message/Messaging Service

MMS - Multimedia Messaging

HTML - Hyper Text Markup Language

HD - High Definition

3G - Third Generation Mobile Network

4G - Fourth Generation Mobile Network

LTE - Long Term Evolution

ITU - International Telecommunication Union

5G - Fifth Generation Mobile Network

6G - Sixth Generation Mobile Network

RF - Radio Frequencies

IEEE - Institute of Electrical and Electronics Engineers

WiFi - Wireless Fidelity

OFDM - Orthogonal frequency-division multiplexing

Mbps - Megabits per second

LEO - Low Earth Orbit

MEO - Medium Earth Orbit

GEO - Geostationary orbit

NASA - National Aeronautics and Space Administration

ISL - Inter Satellite Links

RWG - Rectangular Waveguide

PCB - Printed Circuit Board

MMIC - Monolithic microwave integrated circuit

SIW - Substrate Integrated Waveguide

EM - Electromagnetic

HSIW - Hollow Substrate Integrated Waveguide

EDC - Effective Dielectric Constant

GCPW - grounded coplanar waveguide

CPW - Coplanar Waveguide

ESICL - empty substrate-integrated coaxial line

SM - Subtractive Manufacturing

3D - 3 dimensions

MIMO - Multiple input multiple output

AI - Artificial Intelligence

ESIW - Empty Substrate Integrated Waveguide

AFSIW - Air Filled Substrate Integrated Waveguide

APHC - Average Power Handling Capability

Contents

Chapter 1

Introduction

1.1 Wireless Network Demands

In wireless communications sector, the ever-increasing demand for a higher data rate and network capacity has always posed a challenge for wireless design engineers; and this will be further demonstrated after seeing the evolution of cellular radio, WLAN and satellite networks which have become indispensable components of our modern lives.

1.2 Wireless Cellular Networks Evolution

Nippon Telegraph and Telephone provided 1G network to Tokyo residents for the first time in 1979. By 1984, the first generational network covered the entirety of Japan, making it the first nation to offer countrywide 1G service.Ameritech did not launch 1G in the United States until March 6, 1983. Canada received the 1G coverage in the mid-1980s [1, 2].

The main features of 1G technology are frequency between 800 MHz and 900 MHz, bandwidth of 10 MHz, analogue switching and frequency modulation and access technique of FDMA (Frequency Division Multiple Access).

Despite being a groundbreaking technology at the time, 1G had significant shortcomings by today's standards. It was tough to listen to someone over a 1G network, due to interference, owing to the poor sound quality. The coverage was also poor and no roaming support was provided. The 1G channel lacked security since there was no encryption method, thus anybody with a radio scanner could listen in on a call. The download speed over 1G was likewise exceedingly poor, reaching around 2.4kbps. Although innovative for its day, 1G had significant space for improvement.

In 1991, following the success of 1G, 2G was introduced in Finland's GSM (Global System for Mobile Communications). The 2G brought a major breakthrough in mobile communications by allowing encrypted calls (no one can listen to a call). During its existence, 2G download speeds were around 0.2Mbps. This was much faster than 1G speed, but still very slow by modern standards for mobile device networks. The 2G network also enabled the transfer of data between devices, allowing access to media such as images on mobile devices. [1, 2]

However, that was not the most advanced element of this data transmission function. In reality, the introduction of text messages (SMS) and multimedia messaging (MMS) as new modes of communication as a result of 2G data transfer radically altered the way we communicate.[1, 2]

SMS and MMS messages are sent in packets of data from one mobile phone to a tower and then to a receiving phone using the same control channels as voice calls.[1, 2]

As texting, downloading, and phone conversations grew in popularity, the 2G network facilitated the tremendous consumer and commercial adoption of cellphones. Nonetheless, as more and more people used cell phones, the need for data exploded. NTT DoCoMo introduced the 3G to the Japanese market in 2001, with a focus on standardizing manufacturers' network protocols. Users were thereafter able to access data from anywhere, allowing international roaming services to commence.[1, 2]

In comparison to 2G, the 3G data transmission speeds averaged 2 Mbps, which is four times faster than 2G. As a result of this expansion, video streaming, video conferencing, and live video chat became a reality. Emails become another typical method of mobile device communication.[1, 2]

The ability to browse the internet on basic HTML pages and stream music on mobile devices made 3G revolutionary. In terms of download speed, although 2G offered the same functionality as 3G, it was less sophisticated.[1, 2] As the 3G era evolved, network enhancements enhanced network speeds and support. Today, download speeds in Canada are almost 6 Mbps.

A few years after the widespread use of smartphones, the desire for faster data and enhanced network capabilities emerged. Near the end of 2009, 4G network was introduced for commercial usage in Norway and supplied today's typical services.

Beginning at a minimum of 12.5 Mbps, 4G offered high-quality video streaming/chat, rapid mobile web access, HD video, and online gaming[1, 2].

When 4G initially began, however, it was not genuinely 4G. When the ITU-R established the minimum needed speed for 4G (12.5 Mbps), it was not achievable. The ITU-R determined that LTE (Long-term evolution) may be labeled as 4G in response to the amount of money invested by technology companies in reaching this objective.

The first 4G release gave speeds little under 12.5 Mbps branding it 4G LTE. Today, though, the offered speeds have increased. In 2020, the median 4G download speed in Canada was 55.50 Mbps.[1, 2]

Since its introduction in 2009, 4G data transfer rates have nearly reached their maximum. With new technologies being released at a rapid rate, the globe needs a quicker network. In March of 2019, South Korea was the first nation to introduce 5G. South Korean telecom carriers KT, LG Uplus, and SK Telecom released the fifth generation. It is currently widely deployed in many countries.It provides speeds 20 times faster than 4G, at around an average of 150 Mbps. [1, 2]

Another significant distinction between 4G and 5G is their latency and bandwidth. Incredible reductions in 5G latency enhance download and upload speeds. Comparatively, 4G has an average latency of around 50 milliseconds and 5G latency can achieve latency to less than 1 millisecond.

Additionally, 5G has a wider frequency range (between 30GHz and 300GHz), allowing it to handle more technologies and devices. 5G is vital to support the IoT technology for device hosting, which are necessary for smart cities and other businesses [1, 2].

Although the 5th generation of mobile communication technology is still in the process of being implemented , it has many limitations, such as latency, security, energy efficiency, and frequency bands. As a result, researchers have already begun developing the 6th generation (6G) system, which will include innovations and technologies that 5G and its predecessors lack. When networks are required to transfer more data at a faster rate, machine-to-machine communication will advance, connecting not only people but also vehicles, devices, and sensors. Due to the concept of pervasive artificial intelligence (AI), there is little doubt that 6G is becoming a popular topic in the scientific community. The emergence of AI's vast usefulness will be the primary driver of 6G's roll-out. It is anticipated that 6G would become the primary necessity for customers by 2030. There are a number of 6G technologies that are expected to fit the needs for system enhancement. These essential technologies comprise Terahertz Communications, Visible Light Communication, Artificial Intelligence (AI), Quantum Network Communications, Space-Airground Integrated Network (SAGIN), Intelligent Healthcare and Intelligent Transportation.[3, 4]

Terahertz communication is emerging as the main groundbreaking technology in 6G network, offering Terabits per second links (Tbps) with notable features like high throughput and minimal latency. It will be able to generate terahertz waves. It is located between the microwave and infrared bands in the electromagnetic spectrum, ranging from 0.1 THz to 3 THz.[3]

Researchers are emphasizing the integration of AI into the 6G network. The deployment of AI in the real world, is anticipated to solve numerous optimization problems. Unlike its predecessors, 6G will leverage collaborative AI, revolutionizing various sectors and paving the way for a new era of communication technology. [3]

Apart from AI, the Visible Light Communication (VLC) holds significant promise as a key technology for 6th generation wireless communication systems. VLC has the potential to bridge the efficiency gap between existing VLC and 5G technology, which already operates at Gbps speeds and is set to achieve Tbps speeds with 6G technology. Utilizing the visible spectrum for communication, VLC enables wireless data transmission through modulation of light waves within the range of 380nm to 750nm wavelengths. This approach is based on intensity modulation of light-emitting diodes (LEDs) and provides a substantial bandwidth of approximately 300 THz, surpassing traditional radio-frequency access networks. [3]

Furthermore, the widespread implementation of Quantum networks and quantum internet is going to revolutionize communication, offering not only faster speeds but also significantly enhanced security compared to current systems. Key features such as high data rates and robust security will play an important role in integrating quantum communication into 6G technology. Researchers have harnessed the principle of entanglement, utilizing tangled photons to transfer information between nodes. [3]

The novel Space-Airground Integrated Network (SAGIN) architecture will support the 6G requirement, by integrating satellites, airborne platforms, and terrestrial networks to achieve ubiquitous coverage and support diverse applications.[5]

The capabilities of 6G technology, including high speed, low latency, and ultra-wide connectivity, can indeed revolutionize healthcare and lead to a shift from treatment-oriented approaches to preventive healthcare. The human system could be monitored continuously to provide early evidence of anything malfunctioning. Also the patients with chronic conditions can be continuously monitored from their homes. [4]

1.3 Wireless Local Area Networks Evolution

Wireless technologies have been developed in the last few decades to provide either internet connectivity or interconnection between wireless devices.[6] These technologies adhere to a variety of standards and provide a range of security options. Wi-Fi technology, HiperLAN1/2, HomeRF, and Bluetooth are the commonly utilised standards. 802.11, 802.11a, 802.11b/g/n, and/or 802.11ac wireless standards fall under the umbrella of Wi-Fi technologies.[6] The IEEE created the 802.11 standard to provide wireless networking technology comparable to Ethernet's conventional counterpart, which has been available for decades. Then the IEEE 802.11a standard uses OFDM technology to operate in the licensed 5 GHz range. Using direct sequence spread-spectrum technology, the popular 802.11b standard works in the unlicensed 2.4 GHz–2.5 GHz Industrial, Scientific, and Medical (ISM) frequency zone. The ISM band has gained popularity for wireless communications due to its global availability. The 802.11b WLAN standard enables transmission rates of up to 11 Megabits per second. It is significantly faster than the original IEEE 802.11 standard (which transmits data at up to 2 Mbps) and marginally faster than regular Ethernet. [6] All of the aforementioned standards are widely used to provide internet connectivity to end devices.

Reliable coverage ranges for 802.11 WLANs depend on various parameters, including necessary data rate and capacity, RF interference sources, physical area and characteristics, power, connectivity, and antenna use. The theoretical ranges for 11 Mbps in a closed office range from 29 meters to 485 meters in an open space. However, empirical investigation indicates that the typical indoor range of 802.11 equipment is roughly 50 meters (about 162 feet). WLAN's range of 400 meters, or roughly a quarter mile, makes it excellent for campus applications.[6]

Over the past 24 years, Wi-Fi, or IEEE 802.11, has progressed from 2 Mbps to multi-gigabit speeds, representing a 1,000-fold increase in throughput. By releasing new protocols such as 802.11n, 802.11ac, and 802.11ax, the standard has consistently progressed to Wi-Fi 6, which can provide speeds of up to 10 Gbps. [1]

1.4 Satellites Evolution

In 1945, Arthur C. Clarke described the fundamentals of satellite communication using geostationary satellites. Clarke argued that the period of a circular orbit with a radius of 42,000 kilometers is precisely 24 hours. A body in such an orbit would appear motionless to an observer on the surface of the Earth. Clarke suggested that three satellites positioned equidistantly around the earth would provide global cov-

erage and could be used to transmit radio or television signals. Telstar, was the first active communications satellite, that was launched into LEO orbit in July 1962. Telstar was capable of relaying up to 600 telephone channels or one television channel over the Atlantic Ocean. As proposed by Clarke, the Syncom mission demonstrated the ability to launch and retain satellites in GEO orbit. In July 1963, Syncom-2 was successfully launched. The orbital period of the satellite was 24 hours, despite the orbital plane's 33-degree inclination. Launched in August 1964, Syncom-3 assisted the transmission of television broadcasts from the Tokyo Olympic Games [7–9]. The choice to develop a global satellite communication system was helped by the practicality of point-to-point satellite communications. Hence, in 1964, the organization INTELSAT was established to provide commercial satellite-based telecommunications services (INTernational TELecommunications SATellite). Early Bird, the company's first satellite, was launched in April 1965 and created links between Europe and the United States, supplementing those provided by transatlantic cables. INTELSAT provided 240 voice channels and one television channel. [7–9]

With the deployment of two Marisat satellites across the Atlantic and Pacific oceans in 1976, the commercial offering of mobile services commenced. These satellites were utilized primarily by the United States Navy and other maritime customers. With the addition of a third satellite above the Indic, the system became globalized. INMARSAT (INTERNATIONAL MARINE SATELLITE) was created in 1979 as the body responsible for the management of a maritime communications system. INMARSAT utilized the Marisat F1, F2, and F3 and Marecs A and B2 satellites until the deployment of its own satellites in the 1990s. During the 1980s and 1990s, technological breakthroughs in antennas, solid-state amplifiers, and satellite tracking systems enabled the development of non-GEO satellite-based global mobile satellite systems. The global coverage capability of the Iridium system is provided by a constellation of 66 satellites in six polar orbits at an altitude of 780 kilometers (shown in Figure 1a). This system is designed to always have at least one satellite visible from any location on Earth. Each satellite emits 48 beams, resulting in a 48-cell structure on Earth, for a total of 3168 cells supplied by the system. [7–9]

For mobile satellite communication systems, LEO, MEO, and GEO orbits have been investigated. All of them have advantages and downsides, making it tough to determine the ideal candidate for each case. The selection of the orbit depends on the communications services, satellite capacities, network structure, and economic variables such as the worldwide cost. [7–9] GEO orbit is a circular orbit on the equatorial plane at a height of 35,786 kilometers. This orbital altitude results in an orbital period equal to one sidereal day. As a result, satellites in GEO orbits seem stationary when observed from Earth. To establish radio contact, it is sufficient

to direct the user's antenna toward the satellite's precise location. With only three satellites, GEO satellites can deliver uninterrupted communications to all customers within their service region. Today, the bulk of spacecraft in space are in the Clarke orbit, with few degrees of separation between satellites. LEO orbits are typically circular and range in altitude from 500 to 2000 kilometers. These values result from the fact that the orbital height must be below the peaks of the inner Van Allen radiation band and above the upper atmosphere to prevent atmospheric drag. To offer simultaneous global coverage of Earth with LEOs, a huge number of satellites are necessary. The number of satellites is contingent upon the needed coverage and the minimum elevation angle. [7–9]

LEO satellites travel quickly relative to the surface of the Earth and the terminals on the ground with which they communicate. Visibility of only a few minutes prior to satellite hand-off is typical, as are significant Doppler shifts. Typically, the propagation delay between the ground and LEO is less than 15 ms, and it fluctuates rapidly when the satellite approaches and exits the local ground terminal zenith. The price paid for decreased delay is the enormous cost of installing such a huge constellation in conjunction with the engineering hurdles presented by frequent handover and ISL (Inter Satellite Links). [7–9]

MEO satellites represent a compromise between LEO's and GEO's with orbit altitudes ranging from 9.000 km to 18.000 km, between the inner and outer Van Allen belts. The orbital period of a MEO satellite is around 6 hours. These orbits permit full Earth coverage with fewer, large satellites. The satellites have larger coverage footprints and also an increased delay. Movement is slower with visibility of few minutes before handover takes place. Signal propagation delay is typically less than 40 ms. [7–9]

1.5 Planar and Non-Planar Components in Wireless Networks

With the recent rapid development of mobile communication systems, as explained in previous sections and also the need for high speed data transfer in sectors of satellite communications, wireless local area networks and cellular networks, the demand for miniaturized and integrated high-performance devices has increased. [10, 11]

For the propagation of RF signals, reliable RF components are necessary, especially for high power applications. The design of RF circuitry requires the use of either planar and non-planar transmission mediums. Some of these transmission mediums

are going to be analyzed in this section.[10, 11]

The Rectangular Waveguide (RWG), shown in Fig.1.1 is a non-planar device and is a great option for the development of low-loss, high-Q factor, and high-power-handling filters. But it is also challenging to fabricate and integrate with other electrical circuits because to its size and complexity. [10, 11]

Typically, rectangular waveguide has a cross section with an aspect ratio of 1:2, with the width being roughly twice as tall as the height. For operating in the frequency range of 3.7 to 4.2 GHz, the big inside dimension is 2.29 inches(5.8 cm). The range between 10.7 to 11.7 GHz has a width of 0.91 inches(2.3 cm). Waveguide is labelled WR- (waveguide, rectangular) followed by numerals indicating the big dimension (i.e., WR-229). The standard unit of measurement is the width without the decimal point.[10, 11]

In a rectangular guide, the dominating mode is TE01, the transverse electric mode, where the electric vector is perpendicular to the propagation direction. In this instance, the vector of the electric wave travels from one wall of the vast dimension to the other.[12]

The loss of a waveguide is influenced by the smoothness of the guide walls and the material from which it is constructed. Typically, the waveguide is formed from copper, brass, or aluminum billets. At 4.2 GHz, copper has a loss of less than 2 dB per 100 feet. Bits of waveguide or components made from waveguide are linked by flanges on mating parts that have been meticulously machined.[12]

Planar microwave structures, such as the microstrip lines, stripline and coplanar waveguide, are simple to build and can connect easily with other electronic systems, but they are more lossy than rectangular waveguides, particularly at relatively high frequencies.[10, 11] The above connection mediums can be realized on radio frequency printed circuit boards (RF PCBs).

RF PCBs are a dynamic and rapidly expanding segment of the PCB manufacturing industry. By using the PCB technology, we can fabricate planar RF components, namely microstrip lines, co-planar waveguides, combiners, circulators and other. [11]

The microstrip lines is the most widely used transmission medium used in RF PCB design. Compared to other planar transmission lines, the microstrip line constitutes approximately ninety percent of MMIC applications. [11, 13]

RF circuit boards and Microwave PCBs are significantly more challenging to design than standard PCB layouts. This is due to potential problems with receiving or transmitting radio signals. Among the most significant issues are noise sensitivity

and narrower impedance tolerances.[11]

Radio and microwave signals are extremely susceptible to noise and require significantly tighter impedance tolerances compared to standard circuit boards. Using ground designs and a large bend radius on impedance-controlled traces is the optimal method for resolving these issues. Ultimately, these solutions will enable the RF/Microwave PCB to attain the highest performance.[11]

There are numerous uses for RF boards, namely the wireless technologies also mentioned in previous sections, specifically smart phones, sensors, robotics, and security. With the introduction of new technologies that push the boundaries of electronics, the need for RF boards is increasing.[11]

To meet the more stringent requirements of contemporary communication systems, it is necessary to develop advanced waveguide configurations that can be easily fabricated and integrated with other devices, while maintaining low loss, excellent stop-band performance, high selectivity, and high power handling.[10, 11]

1.5.1 Substrate Integrated Waveguide (SIW)

One of the solutions invented recently to overcome the above challenges faced by RWG and microstrip PCB board transmission lines, is the SIW technology. As mentioned earlier, bulky metallic structures such as waveguides and coaxial lines have been frequently employed for decades, since they offer low loss and well-behaved electromagnetic qualities. However, low-cost, small-sized, and highly-integrated circuits are gaining popularity as they better match modern applications like mobile and wearable technologies. [11, 14, 15]

The SIW approach is an alternative solution to the existing transmission line options. It may integrate planar structures such as microstrip lines with nonplanar structures such as rectangular waveguide. Through the use of metalized vias or holes on dielectric substrates, the traditional waveguide structure can now be achieved in a planar form. It not only possesses the benefits of a conventional microstrip circuit, such as low cost, ease of manufacture, and small size, but also gives waveguide qualities that were previously only attainable with a bulky structure. [11, 14, 15]

It also enables the integration of passive components such as antennas and active components such as amplifiers on a single substrate, hence minimizing losses and parasitic effects. The japanese researcher K.Wu has first used the term "SIW" and reported numerous SIW-based circuits and antennas.[14, 15] After that, SIW technology began to gain people's attention, resulting in its widespread application in all fields of microwave engineering. Many of its invaluable qualities have been

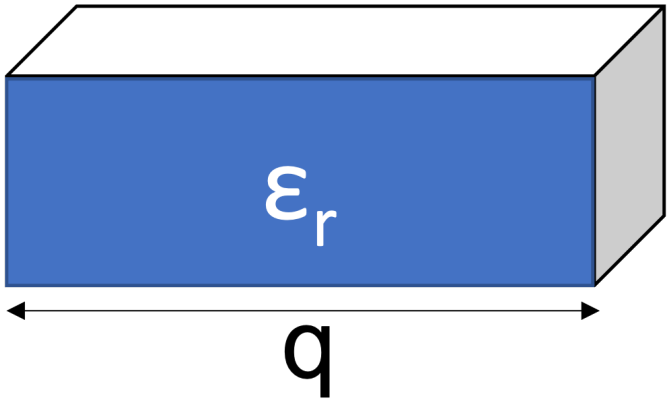

Figure 1.1: Rectangular Waveguide dielectric parameters

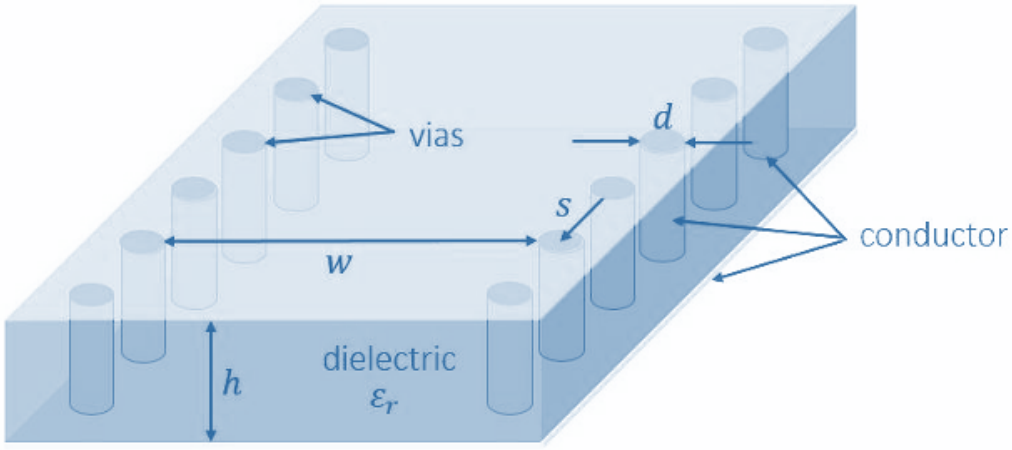

Figure 1.2: Substrate Integrated Waveguide reproduced from [14]

conceptually and mathematically explained after extensive research.[11, 14, 15]

In general, an SIW is built on a solid dielectric substrate with two parallel rows of metallic posts (vias) that replace the side walls of a RWG. It consists of a top and bottom metallic layer enclosure on both sides of the dielectric substrate, as shown in Figure 1.2.

1.5.1.1 The SIW Equations

This section gives an overview of the most important equations of SIW as presented in [16, 17]. For the calculation of the cut-off frequency of arbitrary mode of the SIW, the rectangular waveguide equation is used as reference as shown in Equation 1.1.

$$f_c = \frac{c}{2\pi}\sqrt{\left(\frac{m\pi}{a}\right)^2 + \left(\frac{n\pi}{b}\right)^2} \tag{1.1}$$

Then for the TE10 mode of operation, equation 1.1, is eliminated into equation 1.2.

$$f_c = \frac{c}{2a} \tag{1.2}$$

where α is dependent on the dielectric constant ($\sqrt{\varepsilon_R}$) and width of the waveguide q as shown in Equation 1.3.

$$a = q\sqrt{\varepsilon_R} \tag{1.3}$$

The width dimension q, of the rectangular waveguide can be related to the width dimension w of the SIW, as shown in equation 1.4.

$$w = q + \frac{d^2}{0.95s} \tag{1.4}$$

Empirically, it was estimated that the vias diameter should be smaller than 1/5 of the guided wavelength and also that the pitch between adjacent vias should be less than 2 times the diameter dimensions as shown in equations 1.5 and 1.6

$$d < \frac{\lambda_g}{5} \tag{1.5}$$

$$s < 2d \tag{1.6}$$

1.5.1.2 SIW losses

The SIW total losses[18], are attributed to many loss factors. These include losses from the dielectric, the metallic conductors and EM wave leakage radiation.

From propagation constant equation 1.7, the attenuation constant can be separated into different parameters of attenuation, namely attenuation due to metal conductivity a_c, due to dielectric loss tangent a_d and due to radiation a_R, shown in equation 1.8. These can be illustrated analytically with mathematical equations shown below as in 1.9, 1.10 and 1.13.

$$\gamma = \alpha + \beta \tag{1.7}$$

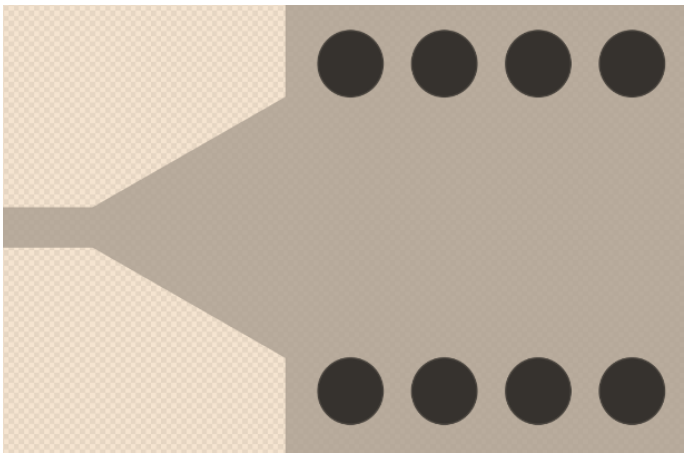

Figure 1.3: Substrate Integrated Waveguide to microstrip transition

$$\alpha = \alpha_c + \alpha_D + \alpha_R \tag{1.8}$$

$$\alpha_{\mathrm{d}} = \frac{\mathrm{k}^2 \tan\delta}{2\beta} \tag{1.9}$$

$$\alpha_c = R_s \frac{(2h\pi^2 + l^3k^2)}{l^3 h\beta k\eta} \tag{1.10}$$

where

$$\eta = \sqrt{\frac{\mu_0}{\varepsilon_0\varepsilon_r}} \tag{1.11}$$

and

$$R_s = \sqrt{\frac{\omega\mu_0}{2\sigma}} \tag{1.12}$$

$$\alpha_R = \frac{\frac{1}{w}\left(\frac{d}{w}\right)^{2.84}\left(\frac{s}{d}-1\right)^{6.28}}{4.85\sqrt{\left(\frac{2w}{\lambda}\right)^2 - 1}} \tag{1.13}$$

1.5.1.3 SIW transitions

In order to integrate an SIW with other planar circuits, transitions need to be employed. The most widely used SIW transitions are from SIW to co-planar waveguide and from SIW to microstrip, both can be seen in Figures 1.3 and 1.4.These interconnections enhance the pros of using SIW, since this makes it easier to integrate the SIW structure with other PCB based RF devices.[19]

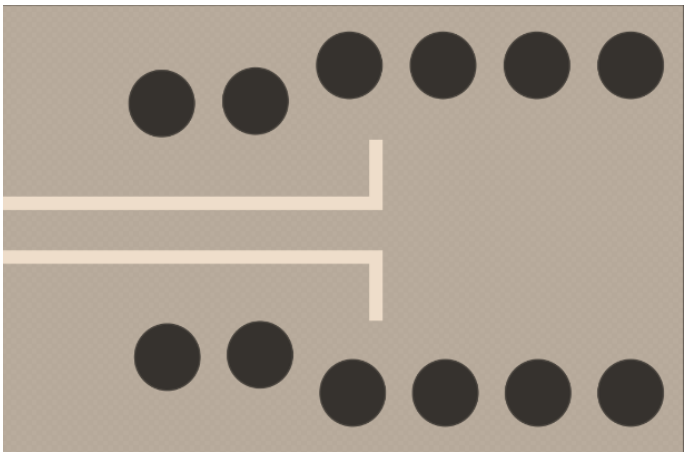

Figure 1.4: Substrate Integrated Waveguide to co-planar waveguide transition

1.6 Literature Review

This section presents the literature review, carried out in this thesis. It examines publications and works related to Substrate Integrated Waveguides with dielectric substrate and also related to Hollow SIWs, with empty or air-filled substrates.

Initially a detailed analysis of SIWs was performed to examine their characteristics before examining hollow and empty SIWs. In [20], the author is examining the SIW's conductor, dielectric, and radiation losses and this work has provided an outline of the modeling of SIW components.

SIW has shown to have many applications for many passive and active devices. It is analyzed, in this section, the wide range of devices that it can be applied, along with its industrial applications.

The work in [21], describes an X- and Ku-band application-compatible SIW filter design with microstrip transmission. Mathematical expressions are used to discuss its design parameters. The return loss (RL) is found to be higher than 10 dB in the whole pass-band in the simulation and measurements, while the insertion loss (IL) is often lower than 3 dB in the entire pass-band. The correlation between simulation results and measured values is strong enough. It is shown that, the Rogers 4003C substrate seems to be an excellent choice for SIW circuits.

The study in [22] has provided the most recent developments in the field of passive components, active components and antennas used in SIW technology. These developments have been detailed and debated. The various technological methods used for the implementation of SIW components and circuits have been described, along with issues related to the modeling and design of SIW components.

In work [23] , a wide frequency range SIW Y-type divider is suggested. The proposed

design altered the coupling regions' dimensions to change the phase difference between the TE 10 and TE 30 modes, unlike to a conventional Y-type divider, which has an in-band stop peak limiting the bandwidth available. The proposed structure is created on the panel using typical fabrication techniques, and measurements match those predicted by the simulation. From 11.10 to 18.64 GHz, the measured reflection loss is better than 10 dB, resulting in a fractional bandwidth of 50.26%.

The work in [24], goes a step further and makes use of hexagonal cavities in multilayer substrate integrated waveguide (SIW) filters. The bandpass filter's design benefits from the hexagonal SIW cavity's ability to combine the flexibility of a rectangular cavity with the effectiveness of a circular one. Low temperature co-fired ceramic (LTCC) technology is used to build and create three different experimental configurations with the same central frequency of 10 GHz and bandwidth of 6%, including third-order and four-order cross-coupling topologies. Both theoretical and experimental results are provided in that work.

Also the publisher in [25], demonstrates the basic structures of SIW filters. It discusses the design guidelines that are crucial for the creation of SIW filters. In terms of trade-offs between loss and cost, the designed SIW resonator is contrasted with other microwave resonators in literature. Different input/output excitation topologies are examined, along with the corresponding unloaded quality factors. By enabling parameter extraction for circuit modeling from field computation, a numerical TRL calibration technique is shown to be effective for accurate modeling and efficient design for the direct-coupled SIW cavity resonator filter, one of the most common filter topologies. The authors demonstrate several methods for enhancing the stopband performance of direct-coupled SIW cavity resonator filters.

As it can be seen from above literature review, the area of SIW technology is constantly expanding and hence, this pushes research towards improved solutions on SIW technology. That is the reason, this thesis is going to investigate the HSIW technology that is an improvement of the SIW device. There are many publication works, that present a hollow, empty or air-filled SIW.

1.6.1 Air-filled or Hollow SIW

1.6.1.1 Introduction

One of the well-known SIW performance constraints is the dielectric substrate, which is responsible for the dielectric loss that, in most situations, constitutes the biggest portion of its transmission loss.

As illustrated in Fig. 1.5, a unique HSIW is presented in which an air cavity is carved

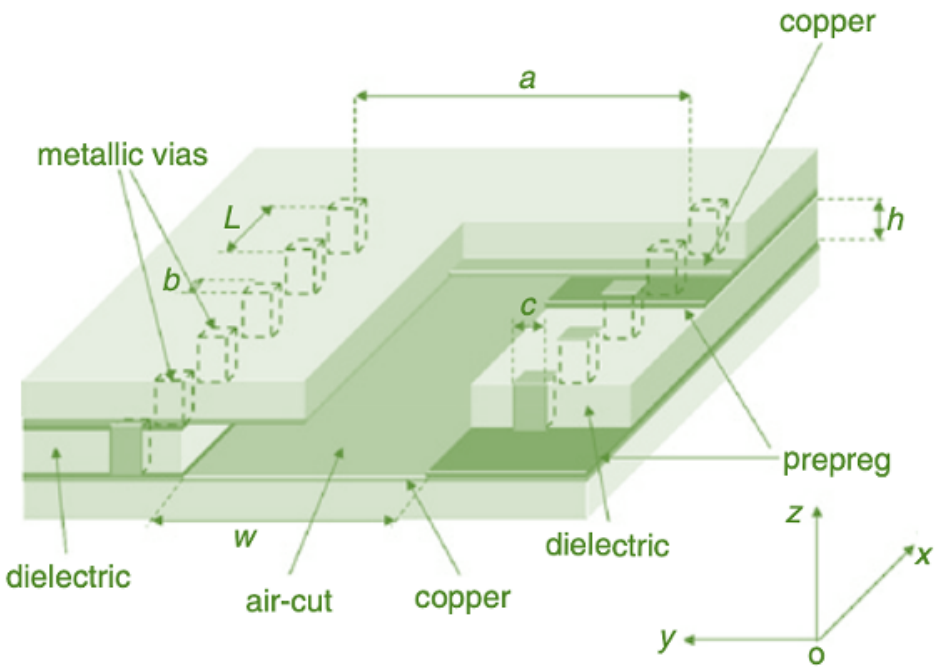

Figure 1.5: Hollow Substrate Integrated Waveguide reproduced from [26]

into the conventional SIW. The main benefit of removing the dielectric substrate can be illustrated in equations 1.7 and 1.8, shown in previous section and that is, the minimization of dielectric losses.

A multi-layer PCB-based modified SIW with an air-cut in the center part has been presented in [26] to minimize dielectric loss and achieve reduced transmission loss. After that, many publication works have employed the air-filled or hollow SIW approach. By doing so, the authors managed to decrease the overall attenuation constant of the SIW transmission line and achieve the required performance.

1.6.2 State-of-the-art dielectric-less (hollow) SIW publications

In [27], an air-filled substrate integrated waveguide (AFSIW) is presented. The performance of the air-filled SIW in terms of energy loss and handling has been investigated in this paper and compared to a conventional SIW filled with dielectric. It was proven that the air-filled SIW outperforms its dielectric-filled counterpart in terms on transmission loss, Q-factor and Average Power Handling Capability (APHC). For interfacing this air-filled SIW with other devices, an air-to-dielectric filled SIW transition is studied theoretically and experimentally. It has a bandwidth limitation that is attributed to manufacturing tolerances. All presented theoretical, simulation and experimental results are in good agreement. The designed AFSIW, gives a very good performance of 4.41 dB/m measured at 33 GHz. The designed structure of

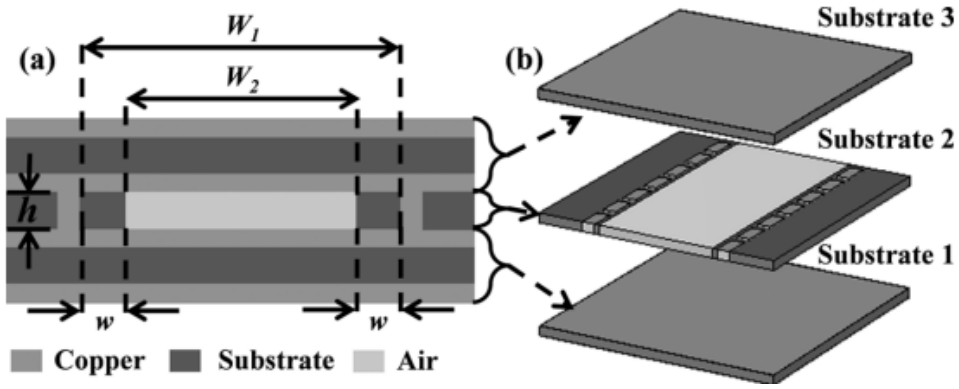

Figure 1.6: Air-filled substrate integrated waveguide (AFSIW) from [27]

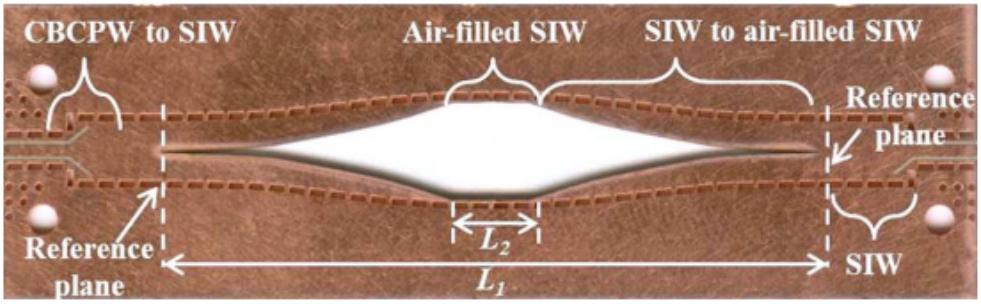

Figure 1.7: Fabricated Air-filled substrate integrated waveguide (AFSIW) from [27]

AFSIW is shown at Fig. 1.6. The fabricated structure can be seen in Fig. 1.7. The proposed low-cost transmission line is being considered by authors for deployment in applications where low-noise, efficient, or high-powered embedded user interfaces are desired, such as emerging millimetre wave detection, telecommunications and energy transfer systems.

The study in [28], describes an AFSIW based fifth-order T-chebyshev bandpass filter. The implementation of the filter makes use of the iris inductive coupling topology. A design concept built on the K-inverted model and Marcuvitz design flow is also presented. To demonstrate the higher performance of AFSIW transmission lines, a comparison between the traditional dielectric-filled substrate integrated waveguide (DFSIW) and the improved AFSIW technology is presented. At 27.92 GHz, the filter's relative bandwidth (BW) is 2.98%. In the passband, the insertion losses are less than -1.15 dB. Applications involving the upcoming 5G, 6G network or space can make use of this bandpass filter.

In work [29], a new integrated line, Empty Substrate Integrated Waveguide (ESIW), is presented. It consists of an empty rectangular waveguide integrated in a flat circuit, attributed to an innovative transition that connects the microstrip line to the empty waveguide. This taper has been successfully implemented for several

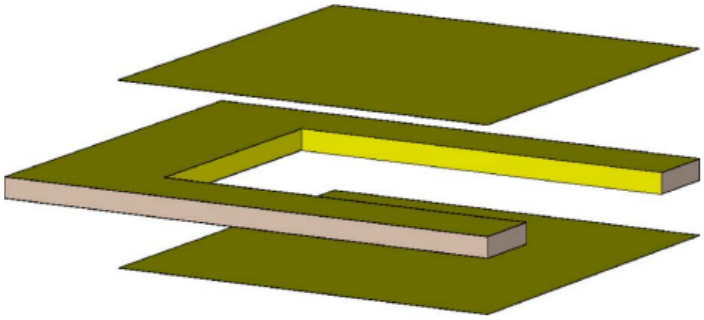

Figure 1.8: Empty SIW layout as in [29]

substrate thicknesses, thus confirming its usefulness for all types of substrates. The manufacturing of this ESIW, requires only standard manufacturing processes for the PCB (drilling, milling and cutting), as well as soldering the top and bottom walls. If a thin copper plate is used for the upper and lower walls, the configuration of the ESIW is nearly identical to that of the equivalent SIW. This means that the new integrated waveguide can be produced at low cost in any laboratory with standard facilities for PCB production. The ESIW layout can be seen in Fig. 1.8.To test the performance of ESIW, two identical filters were manufactured using SIW and ESIW technology. To prove the ESIW concept, the author of [27], designs four-pole Chebyshev filters based on ESIW fabrication method. Two sets of filters were designed, one for 11 GHz and another at 19.5 GHz. These can be seen in Fig.1.9. The measurement of the filter response is in good agreement with the simulation results. The insertion loss of the filters are 0.5 dB for 11 GHz, and 0.8 dB for 19.5 GHz. The measurements of ESIW also show that, the new technology delivers lower loss and better quality factor (measured quality factor is 4.5 times higher for filters at 11 and 19.5 GHz). This quality factor is not better or equivalent as the standard rectangular waveguides, but it is much better than SIW, while retaining the advantage of being integrated into conventional PCB circuits and its cost is low for production. ESIW devices are not as compact as equivalent SIW devices due to the lack of dielectric. The proposed device achieves a very good performance of 0.8 dB/m measured at 19.5 GHz. Furthermore, at high frequencies, ESIW has superior performance in terms of loss and its quality factor increases. Therefore, it can be concluded that this ESIW is a very promising alternative to a standard SIW, especially for high frequency applications.

A hollow substrate integrated waveguide (HSIW) is presented in [30], that is may be used to create low-loss millimetre-wave (mm-wave) transmission lines. By approaching HSIW as a fusion of a dual dielectric-loaded rectangle waveguide (RWG) and a typical integrated substrate waveguide, a novel analytical technique for HSIW is

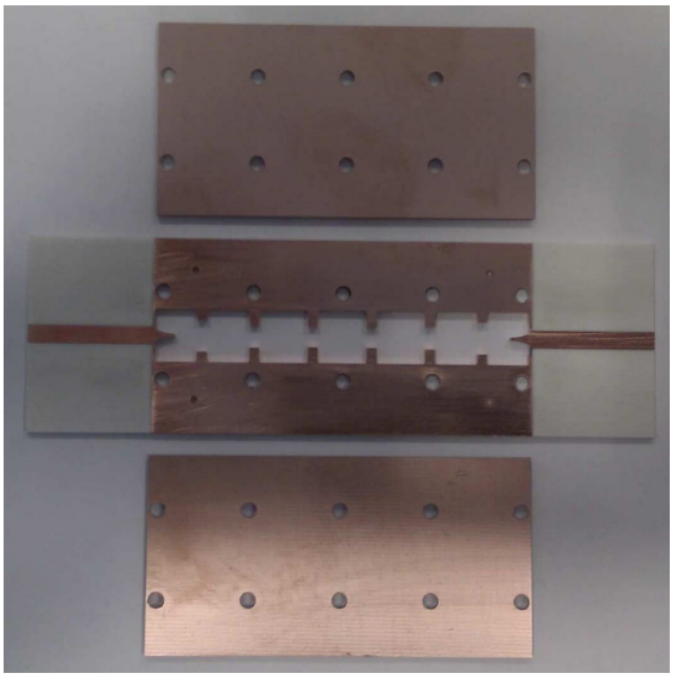

Figure 1.9: Empty SIW fabricated parts before assembly, as in [29]

given. The Ka-band HSIW parts are fabricated with the help of a low-temperature co-fired progressive multilayer ceramic technique. The author then presents the steps required to assemble an HSIW. It consists of many steps including;pre-lamination, laser-machining, screen-printing, lamination and co-firing. The observed measurement results and theoretical simulations are in a good agreement. In the Ka band, an average loss of 9 dB/m—comparable to an air-filled RWG—is obtained. This suggests that there is a lot of potential for this technique to produce highly integrated mmWave modules. It is therefore an excellent option for millimetre wave devices in 5G and 6G communication networks and a new approach to building a hollow SIW device. The 3D design of the Hollow SIW can be seen in Fig.1.10 and a cross-sectional view can be seen in Fig.1.11.

According to the theoretical-analysis approach of an HSIW [30] is a mixture of those of RWG and SIW; consequently, two processes are required to analyze and design the HSIW (to determine the width of the HSIW). HSIW is considered initially as a two-dielectric loaded RWG. After resolving this boundary value problem, the two-dielectric loaded RWG is converted to a uniformly filled RWG by injecting the effective dielectric constant (EDC), ϵ_e. This can be seen in Fig.1.12.

As proved in [30], the width of the HSIW can be calculated by using equation 1.14 : where c_0 is the velocity of light in free space and f_c is the cutoff frequency (Hz). It also includes a loading ratio (q), that is shows how much space the dielectric filling (α_1) occupies, shown in equation 1.15. Therefore the effective dielectric constant

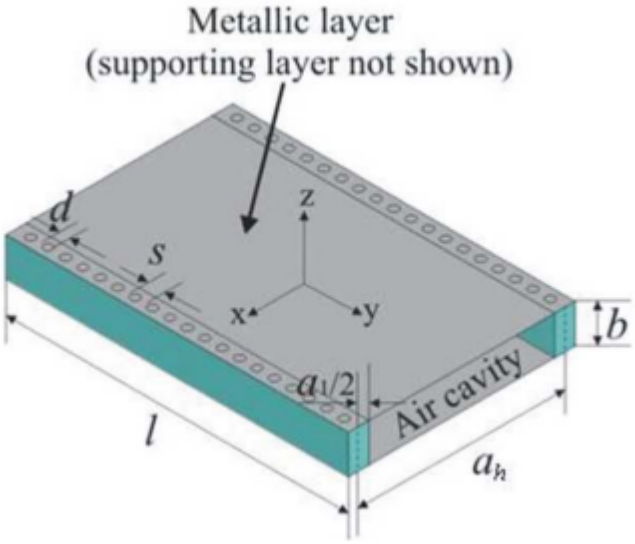

Figure 1.10: 3D Hollow SIW as in [30]

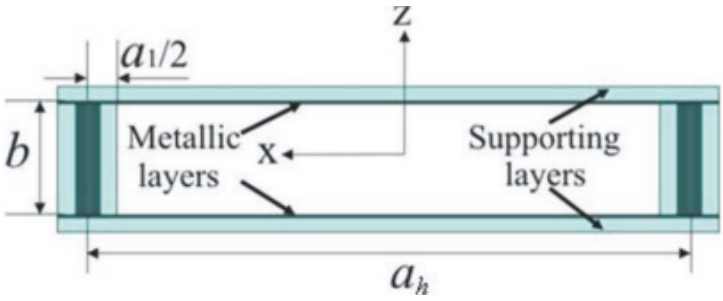

Figure 1.11: Cross-sectional view of Hollow SIW as in [30]

($\epsilon_{r,eff}$) shown in 1.16, formed is a combination of the air and dielectric material, where β is the propagation constant and k_0 is the wavenumber.

The fabricated HSIWs of [30], are shown in Fig.1.13 and their measurement fixture is shown in Fig.1.14.

$$W_{HSIW} = \frac{c_0}{2f_c\left[0.999 + 4.946 \times 10^{-4} \times e^{(9.406q)}\right]} \tag{1.14}$$

$$q = \frac{2a_1\sqrt{\varepsilon_r}}{W_{HSIW}} \tag{1.15}$$

$$\varepsilon_{r,\,\text{eff}} = \frac{\beta^2 + \left(\frac{\pi}{W_{HSIW}}\right)^2}{k_0^2} \tag{1.16}$$

An empty substrate-integrated coaxial line (ESICL) is presented in [31], that is a new structure that can be totally constructed utilizing PCB standard production techniques and common dielectric substrate layers. This structure exhibits several

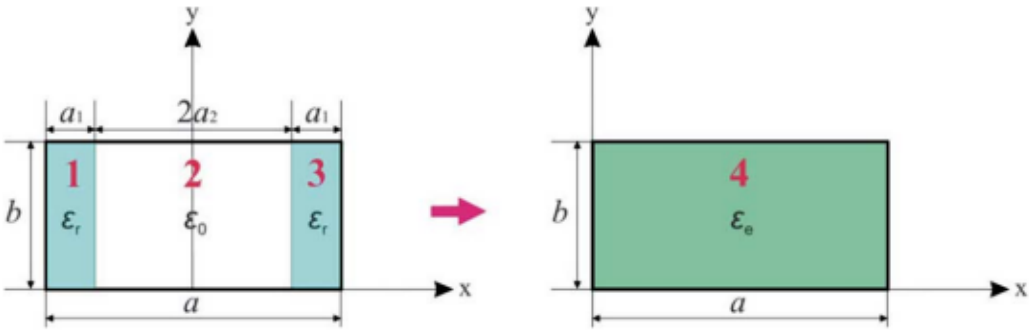

Figure 1.12: Transformation from a two-dielectric loaded RWG into a uniformly filled one of EDC, ϵ_e, as in [30]

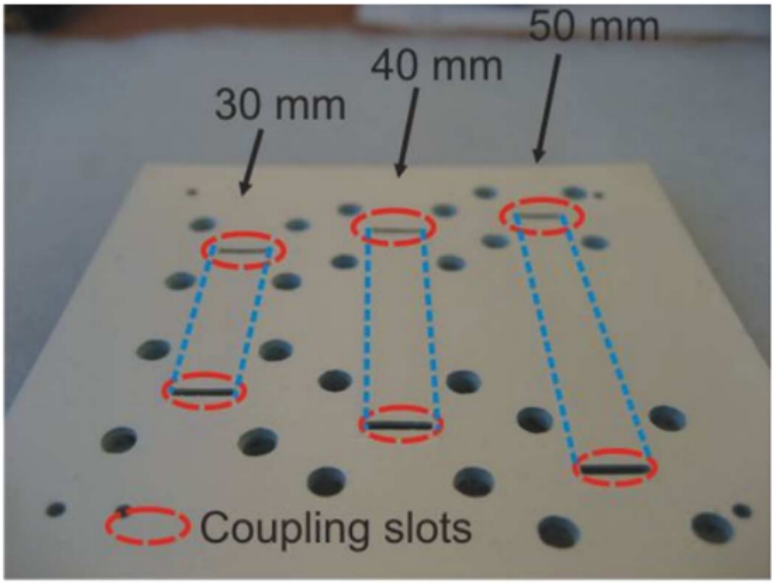

Figure 1.13: Prototype of the WR28-like HSIW as in [30]

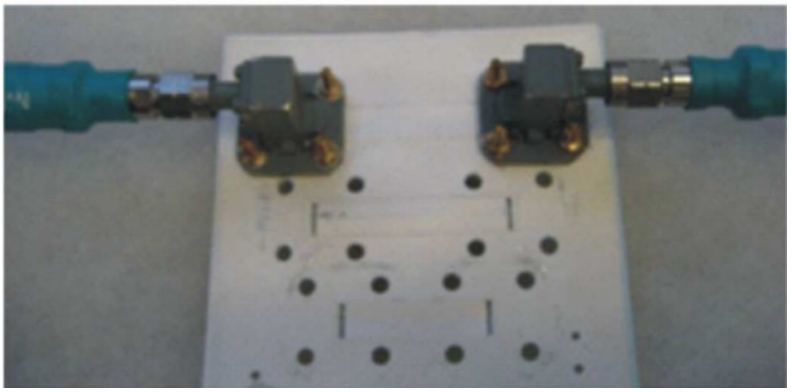

Figure 1.14: Measurement fixture of the WR28-like HSIW as in [30]

extremely intriguing characteristics, such as low loss, non-dispersion, immunity to interference or cross-talk, etc., which makes it highly desirable for the creation of high-quality passive or active devices. The high-performance transition from a conventional planar transmission line, a GCPW, to the innovative ESICL has been designed for the first time in that study. As a consequence, the promising ESICL has been successfully and completely integrated in a planar substrate for the first time. A broad band (100% fractional bandwidth) band-pass eight cavity filter in ESICL has been built and, utilizing this novel transition, incorporated in a planar system to demonstrate this point. When taking into account both feeding GCPW-to-ESICL transitions, the filter demonstrates extremely high quality response over the whole band of interest, with observed insertion losses of 0.23 dB at 11.15 GHz. The findings in this research offer a wealth of opportunities for the development of high-quality PCB-integrated devices in ESICL that have extremely low losses, broad operating bandwidths, great stability, and immunity to interference, cross-talk, and dispersion.

In [32], an innovative approach based on conventional PCB methods has been developed for the manufacturing of buried RWG. This approach is referred to as dielectric-less SIW. This realization enables the attainment of propagation properties similar with RWGs since the interior surface is entirely metallized, except for the space covered by the prepreg. The EM field is entirely contained in an air-filled area, with no path to dielectric, in contrast to SIW and multilayered SIW. As a result, FR4 laminates with superior thermomechanical characteristics and a low price may be used. This method results in producing devices that are lightweight, small, low loss and able to handle high power.

Another air-filled SIW is presented in [33]. The low-cost multilayer Printed Circuit Board (PCB) technique was used to create this low-loss transmission line. The measured insertion loss of the air-filled SIW of interest at U-band is 0.122 $\pm$0.122 dB/cm compared to 0.4 $\pm$0.13 dB/cm for its dielectric-filled counterpart. Furthermore, an air-filled SIW phase shifter is reported for the first time. The author has achieved a measured 0.15 $\pm$0.14 dB transmission loss at U-band.

The paper in [34] outlines the design and implementation of a half-mode slab air-filled substrate integrated waveguide (HM-SAFSIW). The study includes theoretical analysis and simulated outcomes to prove the operating principles. For experimental confirmation, a transition to SIW is incorporated and tested in a back-to-back configuration. The author employs a FR-4 cover and the experimental results demonstrate an insertion loss of 1.1 $\pm$ 0.17 dB and a reflection coefficient exceeding -21.5 dB across the entire Ka-band. Additionally, utilizing two transmission lines of varying lengths

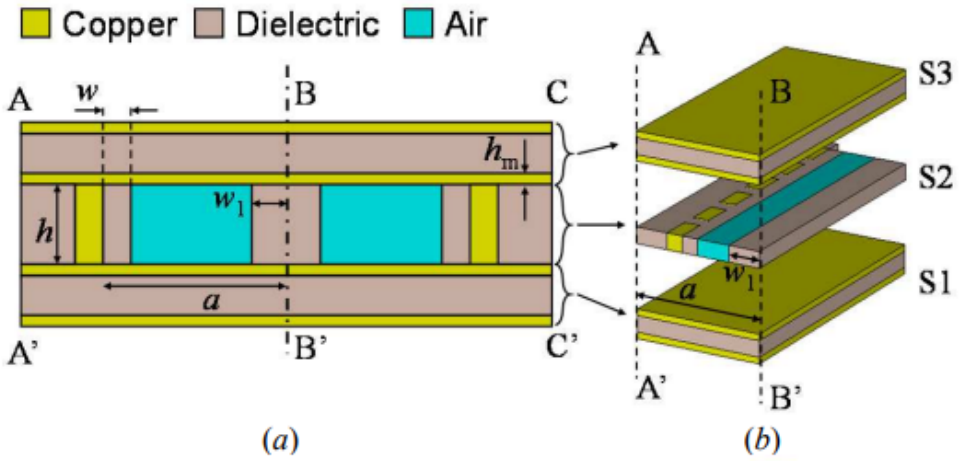

Figure 1.15: Designed HM-SAFSIW as in [34]

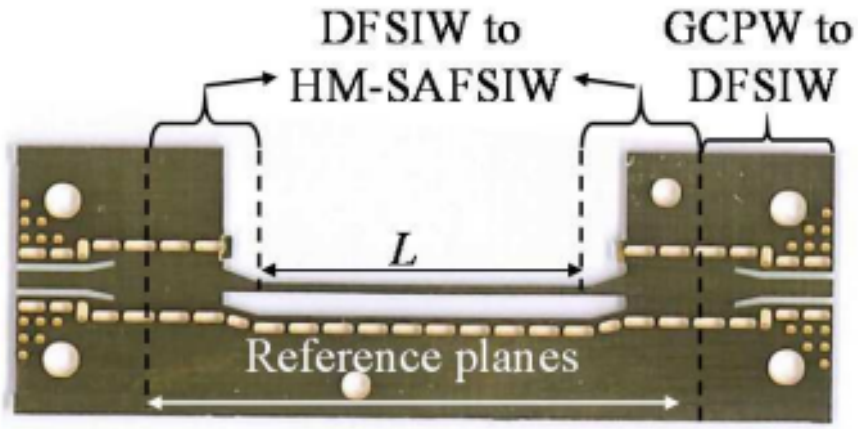

Figure 1.16: Fabricated HM-SAFSIW as in [34]

achieves an attenuation of 29.8 dB/m at 33 GHz. This innovative half-mode slab air-filled SIW offers extensive flexibility in controlling attenuation and phase constants, making it valuable for designing passive and active microwave millimetre-wave components. The designed HM-SAFSIW can be seen in Fig. 1.15 and the fabricated structure shown in Fig. 1.16.

From the above hollow/empty/air-filled SIWs, the ones which are manufactured and assembled, are summarized in Table 1.1, and it can be seen that there is a range of empty SIW options, some of them requiring more fabrication and assembly steps than others, but on the other hand, these may provide lower attenuation losses. Therefore, there is a trade-off between good performance and manufacturing steps. Also, most of the reported designs provide an interconnection transition to either microstrip, CGCPW or WG.

Name	Attenuation	Height	Manufacturing	Transition
ESIW [29]	0.8 dB/m @ 19.5 GHz (total loss, measured)	1 substrate + two covers	Mechanical CNC, micro-milling+electroplating, Reflow soldering	microstrip to ESIW
AFSIW [27]	4.41 dB/m @ 33 GHz (total loss, measured)	1 substrate + two covers	Laser micromachining, Lapping and polishing, Sputtering, electro-deposition	SIW to AFSIW
HSIW [30]	9 dB/m @ 30 GHz (total loss, measured)	1 substrate + two covers	Low temperature cofired ceramic (LTCC) Partially filled with dielectric	WR to HSIW
HM-SAFSIW [34]	22.4 dB/m @ 33 GHz (total loss, measured)	Multi-layered PCB	Laser micromachining, Lapping and polishing, Sputtering, electro-deposition	DFSIW to HM-SAFSIW GCPW to DFSIW

Table 1.1: Comparison of empty or hollow SIW publications that demonstrated device fabrication and measurement

1.6.3 Additive Manufacturing (3D printing) technologies

The PhD project is aiming to utilize 3D printing technologies to design and fabricate RF devices. For this reason, this section presents an overview of the 3D printing technologies used in industry.

Digital fabrication technology, known as 3D printing or additive manufacturing, constructs physical objects based on a digital model by adding materials layer by layer. This rapidly advancing technology finds widespread use globally. It's applied extensively for mass customization and the production of open-source designs in agriculture, healthcare, automotive, and aviation sectors. 3D printing operates by depositing material layer by layer directly from a computer-aided design (CAD) model. This section will discuss various 3D printing technologies, their applications, and the materials utilized in the manufacturing industry [35].

1.6.3.1 3D print technologies

Binder jetting involves selectively depositing a liquid binding agent onto powder particles, enabling the production of casting patterns and large-volume items from materials like metals, sands, polymers, hybrids, and ceramics. The process is cost-effective and can create large objects.[35]

Directed Energy Deposition, used for repairing or enhancing existing components, offers precise control over grain structure. It utilizes techniques like laser deposition and laser engineered net shaping (LENS) and is typically applied to metals and metal-based hybrids. The process allows movement in multiple directions, providing flexibility.[35]

Material extrusion, seen in technologies like Fused Deposition Modelling (FDM), creates parts by extruding heated thermoplastic filament layer by layer. It can print multi-material and multi-color objects, making it versatile and cost-effective for creating functional parts.[35]

Material jetting like Poly-jet involves selectively depositing build material drop by drop under ultraviolet light. It is capable of producing parts with high dimensional accuracy and smooth surface finish, using a wide range of materials including polymers, ceramics, composites, and hybrids.[35]

Powder bed fusion techniques like Selective Laser Sintering (SLS) and Electron Beam Melting (EBM) use lasers or electron beams to melt and fuse powdered materials. SLS, developed in 1987, can create metal, plastic, and ceramic objects with high accuracy and speed.[35]

Sheet lamination involves bonding sheets of materials together to create objects. Technologies like Laminated Object Manufacturing (LOM) and Ultrasound Additive Manufacturing (UAM) are examples. It allows full-color prints, is cost-effective, and offers ease of material handling and recycling opportunities.[35]

Vat photopolymerization uses lasers, light, or ultraviolet (UV) to cure photo-reactive polymers. Techniques like Stereolithography (SLA) and Digital Light Processing (DLP) create high-quality, detailed products. DLP, with its faster speed, is advantageous due to its use of conventional light sources and liquid crystal display panels.[35]

1.6.3.2 Materials used for 3D print technologies

Plastics are the most widely used material in 3D printing. The PLA, ABS, PETG, and nylon are frequently used in FDM and SLA printers.[35]

Metals like aluminum, titanium,alloys and stainless steel are used in metal 3D printing technologies. These are applied to sectors like healthcare, aerospace and biomedical industries.[35]

For applications in the dental and medical fields, ceramics can be used in certain 3D printing methods. Materials like alumina, bioactive glasses, and zirconia are used, enabling the production of complex-shaped parts with high density and mechanical strength.[35]

Composites are materials used in 3D printing that combine different substances to achieve specific properties, such as carbon-fiber-reinforced polymers. They are widely used in aerospace sector.[35]

1.7 Research Questions

The PhD is aiming to address how can a Hollow Substrate Integrated Waveguide (HSIW) be efficiently fabricated using cost-effective and readily available materials. It is examining if a low-cost and high-performance HSIW can be designed to overcome the fabrication and assembly complexities of the existing HSIW designs. Furthermore, it explores whether 3D printed materials can be used to fabricate RF and mm-wave devices to be used in high frequency and high power applications. It is also examining what are the characteristics of the HSIW structure in terms of bandwidth, insertion loss, and return loss. In addition, the research is addressing how does the new HSIW structure compares to standard HSIWs in terms of performance metrics, including the propagation loss.

The PhD project is answering to the question what are the electromagnetic characteristics, propagation modes, and transmission properties of the proposed HSIW, and how can this knowledge be utilized in advanced HSIW-based devices and systems for high-frequency communication and other emerging applications.

The research work is exploring if there is a possibility of fabricating and assembling a curved HSIW, that can perform well in high frequency and high power application where curved surfaces are involved.

These research questions can guide further studies and investigations related to both straight and curved HSIWs and their applications in the field of microwave and millimetre-wave technologies.

1.8 Key Research Contributions from this PhD project

This thesis conducts a detailed comparison of different planar transmission lines, including microstrip, strip-line, and the Substrate Integrated Waveguide (SIW). It demonstrates that conventional planar transmission lines suffer from radiation and material losses at higher frequencies, while SIW maintains better power signal level at higher frequencies, making it suitable for high-frequency and high-power applications. The thesis explores Hollow Substrate Integrated Waveguide (HSIW) as an emerging technology and it identifies that HSIW offers improved performance and cost-effectiveness compared to existing SIW designs. The study proposes new methodologies for designing and fabricating 3D-printed HSIW devices.

The research optimizes the proposed HSIW geometry based on simulation results and achieves the desired impedance matching with the microstrip interconnection

and the SMA connectors. The newly introduced fabrication process of the HSIW utilizes precision cut of copper sheets and 3D-printed dielectric substrates. The study acknowledges minor tolerances in the fabrication process and suggests optimization possibilities for the future.

Lab measurements confirm the low attenuation loss and high signal integrity of the 3D-printed HSIW through mathematical extraction using S-parameter measurements. The designed HSIWs demonstrate wide bandwidth in the Ka-band range, making them suitable for high-frequency communication systems, to be used in space and defence applications. The research identifies practical applications for HSIW technology, including slot antenna arrays in Multiple Input Multiple Output (MIMO) configurations. It highlights HSIW's potential in various high-frequency communication scenarios. The thesis emphasizes the advantages of HSIW over conventional planar transmission lines, including higher power handling capacity, improved electromagnetic shielding, low cost, and ease of integration with other planar circuit boards. This thesis, for the first time, presents a novel curved HSIW, that can be used for high-frequency communication applications. It conducts an in-depth analysis of dielectric materials, chooses suitable materials for the curved HSIW substrate, and validates their performance through simulations and measurements. The study demonstrates that curved HSIWs can maintain low attenuation loss across a wide operational band.

In summary, the thesis significantly contributes to the advancement of high-frequency communication systems by introducing and optimizing 3D-printed Hollow Substrate Integrated Waveguides, showcasing their superior performance, and exploring their potential applications in modern wireless technologies.

1.9 Thesis Outline

The aim of this thesis, is to design a new HSIW alternative to the previous HSIW designs, that will be more cost-effective, it will have improved performance and less fabrication complexity.

The rest of the thesis is structured as follows. The Chapter 2, presents for the first time a novel fabrication methodology to build a Hollow Substrate Integrated Waveguide (HSIW), based on additive and subtractive manufacturing. The whole manufacturing process is analyzed step by step, starting up by fabricating the components using in-house facilities. Later on, it describes all the assembly process performed at the University of Leeds premises with the assistance of off-the-shelf components. The Chapter 3, presents a novel HSIW transmission line and exam-

ines its characteristics. It involves analysis of its electromagnetic behaviour along with software simulations and mathematical analysis. The chapter also presents the simulated and measured propagation losses of this device. It finally compares its performance with other state of the art hollow SIWs and concludes that this device would be a great candidate to be used in high frequency systems. Chapter 4, presents for the first time, a curved HSIW, a novel type of transmission line, that can be applied on curved or rounded surfaces. It can be used in cases where there is a need for transferring RF power on a mechanical body like the arm of a robot. The chapter analyzes the electromagnetic behaviour and how the curvature affects the propagation loss of the devices. It shows the RF power leakage due to the curvature and also shows the mathematical analysis of the electromagnetic wave propagation.

Finally, Chapter 5, summarizes all the results shown in previous chapters and gives guidelines for future work.

Chapter 2

Harmonized Rapid Prototyping of Millimeter-Wave Components Using Additive and Subtractive Manufacturing

Published in IEEE TRANSACTIONS ON COMPONENTS, PACKAGING AND MANUFACTURING TECHNOLOGY

https://ieeexplore.ieee.org/document/9792420

Nonchanutt Chudpooti , Member, IEEE, Giorgos Savvides, Nattapong Duangrit , Member, IEEE, Prayoot Akkaraekthalin , Member, IEEE, Ian D. Robertson , Fellow, IEEE, and Nutapong Somjit , Senior Member, IEEE

2.1 Abstract

In this paper, a harmonized fabrication and assembly process combining additive and subtractive manufacturing is introduced for the rapid manufacture of millimeter-wave components, especially those using hollow substrate integrated waveguide (HSIW). HSIW has been shown to have some significant advantages for millimeter-wave communications, radar and sensing systems, but its fabrication can be challenging. To pattern the metallic layers that form the top and bottom HSIW walls, as well as other structures such as microstrip lines and landing pads for integrated circuits and passive components, a subtractive fabrication process using a water-jet laser cutter was employed. To fabricate the dielectric substrate using low-cost Acrylonitrile Butadiene Styrene (ABS), with cavities for the waveguides, a Stratasys

PolyJet 3D printer (Objet1000) was used. The HSIW components were then assembled using commercially-available through-substrate copper transitions, completely eliminating the process of throughsubstrate via-hole formation and metallization. The manufacturing techniques conventionally used for these vias are generally expensive and intricate at millimeter-wave frequencies. Therefore, the proposed fabrication and assembly process in this paper decreases the overall fabrication cost and complexity, and it is shown that this is achieved without compromising the performance of the millimeter-wave HSIW components. The measurement results show that a propagation loss of 13.55 dB/m (0.01355 dB/mm) is achieved for the first HSIW prototype, which is believed to be among the lowest propagation losses ever reported at these frequencies. The proposed harmonized fabrication and assembly technique has also a strong potential, by combining the advantages of additive and subtractive manufacturing techniques, to realize a new class of millimeter-wave components with the possibility of manufacturing conformal and flexible component shapes, based on the materials used.

2.2 Introduction

The 3-D printing technology, also known as additive manufacturing (AM), is defined as the development of an arbitrary 3-D shape, by building layer upon layer [1]. Specifically, material jetting [2], [3] offers the best printing accuracy and resolutions when compared with fused deposition modeling (FDM). This technique uses a nozzle head to drop the liquid photopolymer onto a plate. The photopolymer materials are cured by UV light to create 3-D parts from CAD models with a fully automated process. Advancements in 3-D printing technology have offered the benefit to develop fast and low-cost prototypes. It has replaced the time-consuming and costly methods of production and manufacturing, such as the computer numerical control (CNC), molding, or casting. In the case of rapid prototyping and medium volume production, the 3-D printing technology is an excellent alternative [4]. According to [5], it is a printing process widely used to produce mechanical and electronic devices, even for high-frequency electronics ranging from a few megahertz to the optical regimes [6]–[10]. More specifically, it is being used in many sectors, such as medical, personal healthcare, dentistry, consumer goods, and wireless communications [11], [13]–[16]. AM processes have been extensively used recently in the development of microwave, millimetre-wave, and even terahertz (THz) devices. Some examples include the design and prototyping of antennas, waveguides, filters, and many other functional RF devices [6]–[8], [11], [17]–[22]. Chan et al. [17] have designed and fabricated a microwave rectangular waveguide (RWG), operating in the Ku-band, by

using a FDM 3-D printing process with polylactic acid (PLA) filament. The internal walls of the waveguide are created with a metal liquid filling. The authors achieved an attenuation constant better than 1.29 dB/m and demonstrated a low-cost and high-performance RWG. Lacombe et al. [16] fabricated a 3-D printed dielectric lens for a slot antenna that enhances the total radiated power. In [23], a 3-D printed flexible antenna is demonstrated that combines acrylonitrile butadiene styrene (ABS) and PLA filaments and is compact in size and lightweight. The 3-D printing process gave the added benefit of building flexible devices since many different materials can be mixed and used by 3-D printing machines. In contrast to AM, subtractive manufacturing (SM) is the process of cutting material away, using the methods of grinding, cutting, or drilling, to form a 3-D shape. The process could be performed manually or by CNC. In an automated CNC process, the machine can perform fabrication based on data from CAD, with minimal human assistance, or in many cases without user interaction. The user may need to consider the feeding rate and the cutting speed of the material to set the fabrication settings on the machine before starting the process. In general, SM process is used typically in prototyping where traditional manufacturing methods like molding and casting are not able to provide the required precision and fabrication tolerance. Newer methods of laser and water laser cutting methods are more efficient and able to process harder materials. The SM processes have also been widely used in manufacturing many high-frequency components from RF to even some millimetre-wave devices [12], [24]–[29]. Obuh et al. [26] and Najib et al. [29] have built microwave sensors by using SM with an LPKF ProtoLaser machine. The designed microwave sensors achieved high accuracy and can be integrated to industrial and biomedical systems. In [29], instead of building an SIW by using traditional PCB methods, the authors used milling and drilling to cut smooth and precise copper sheets to form an empty SIW, eliminating all dielectric losses. In general, the SM methods used in these devices have provided a precise and accurate cutting that enhance the performance of millimetre-wave and THz devices. These previous research works are generally based on only either additive or SM. In this article, a harmonized fabrication technique combining both AM and SM to fabricate high-performance microwave and millimetre-wave components is introduced. To demonstrate the coordinated fabrication process, an HSIW transmission line operating from 21 to 31 GHz was fabricated and characterized, with a primary interest in signal transmission losses. The proposed harmonized fabrication technique combines the advantages from both additive and SM, i.e., rapid device prototyping and ease of fabrication with fully automated processes. The harmonized fabrication also completely removes the need for the chemical processes generally required for conventional material etching and metallization, such as photolithography and electroplating, which require toxic chemicals and experienced users to operate

the process. Moreover, the commercially available vertical through-substrate copper transitions were used during the assembly process as electrical connections of the patterned metallic layers on top and bottom of the 3D-printed substrate. This process completely eliminates the traditional through-substrate etching and via hole metallization processes, introducing superior cost effectiveness, ease of fabrication, and fabrication reliability.

2.3 Design and Geometry

The geometrical structure of the HSIW consists of four parts. These are a top and bottom copper sheet, a dielectric substrate, and prefabricated copper rivets, as shown in Fig. 2.1(a). The top and bottom copper sheets represent the waveguide horizontal walls. The copper sheets have a height of 0.15 mm and are supplied by Goodfellow [30]. Between the copper sheets, there is a dielectric ABS substrate, that is hollow in the middle; the hollow dielectric substrate minimizes the dielectric losses and so contributes to a lower propagation loss. Some commercially available copper rivets from Fortex [31] are used to attach the aforementioned layers together and these represent the vertical metallic walls of the waveguide. The prefabricated copper rivets are pressed with the PTH400 through hole plating (THP) machine also supplied by Fortex [31], in order to bind the three layers (copper sheets and dielectric) together, as shown in Fig. 2.1(b). It should be noted that this assembly step can be performed using a lamination technique, such as those used for large area multilayer PCBs in the mass production of consumer products. Frequencies in the 26–40 GHz range are already widely used in 5G systems, employing quite conventional transmission-line components fabricated on these traditional laminate materials. For 6G systems, it is likely that the so-called THz frequencies will be used (over 100 GHz), and then, the dielectric losses become much more of a problem and the HSIW can offer significant advantages. The designed HSIW has been simulated in the commercially available Electromagnetic (EM) solver CST Studio [32]. For measurement purposes, the HSIW is matched to 50- microstrip feed lines, as shown by the geometry in Fig. 2.1.

2.4 Fabrication and Assembly

All the HSIW parts were fabricated in-house at the University of Leeds National Facility for Innovative Robotics, using a Synova MCS 300 Laser MicroJet1 Cutter [33] and a Stratasys Objet 1000 PolyJet 3-D printer. The processing of the copper sheets and dielectric substrate fabrication are now described.

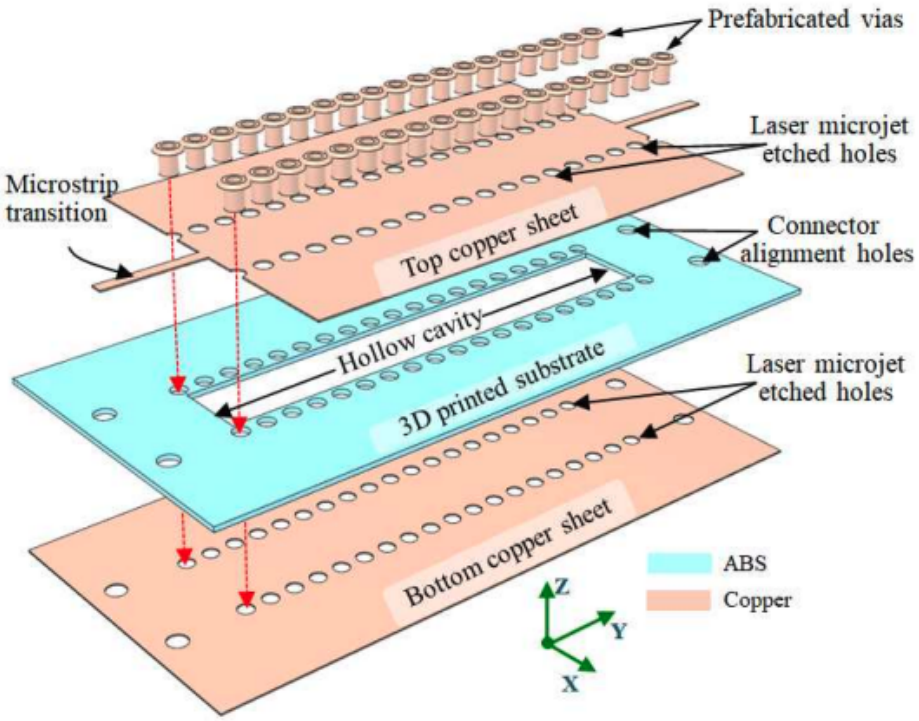

(a)

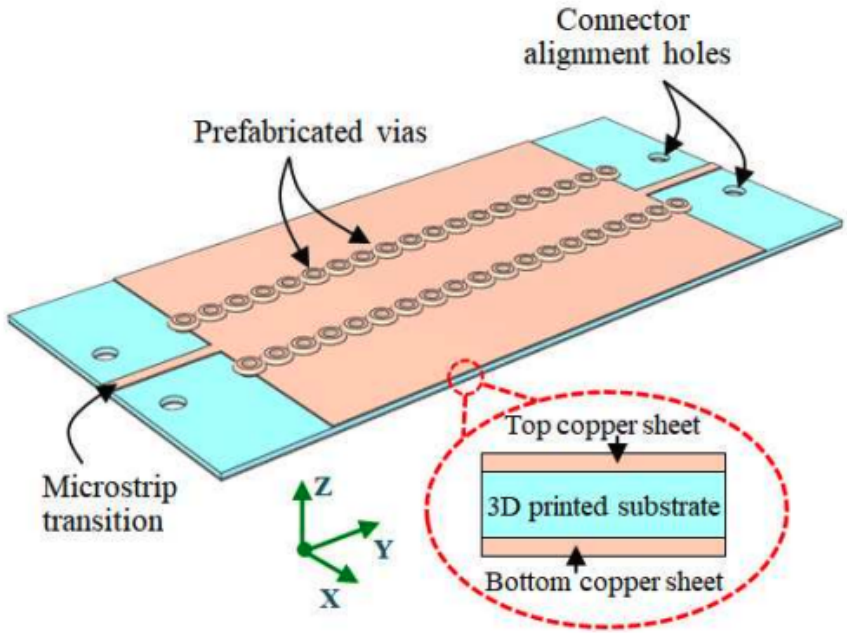

(b)

Figure 2.1: 3D geometry of HSIW : (a) before assembly and (b) after assembly

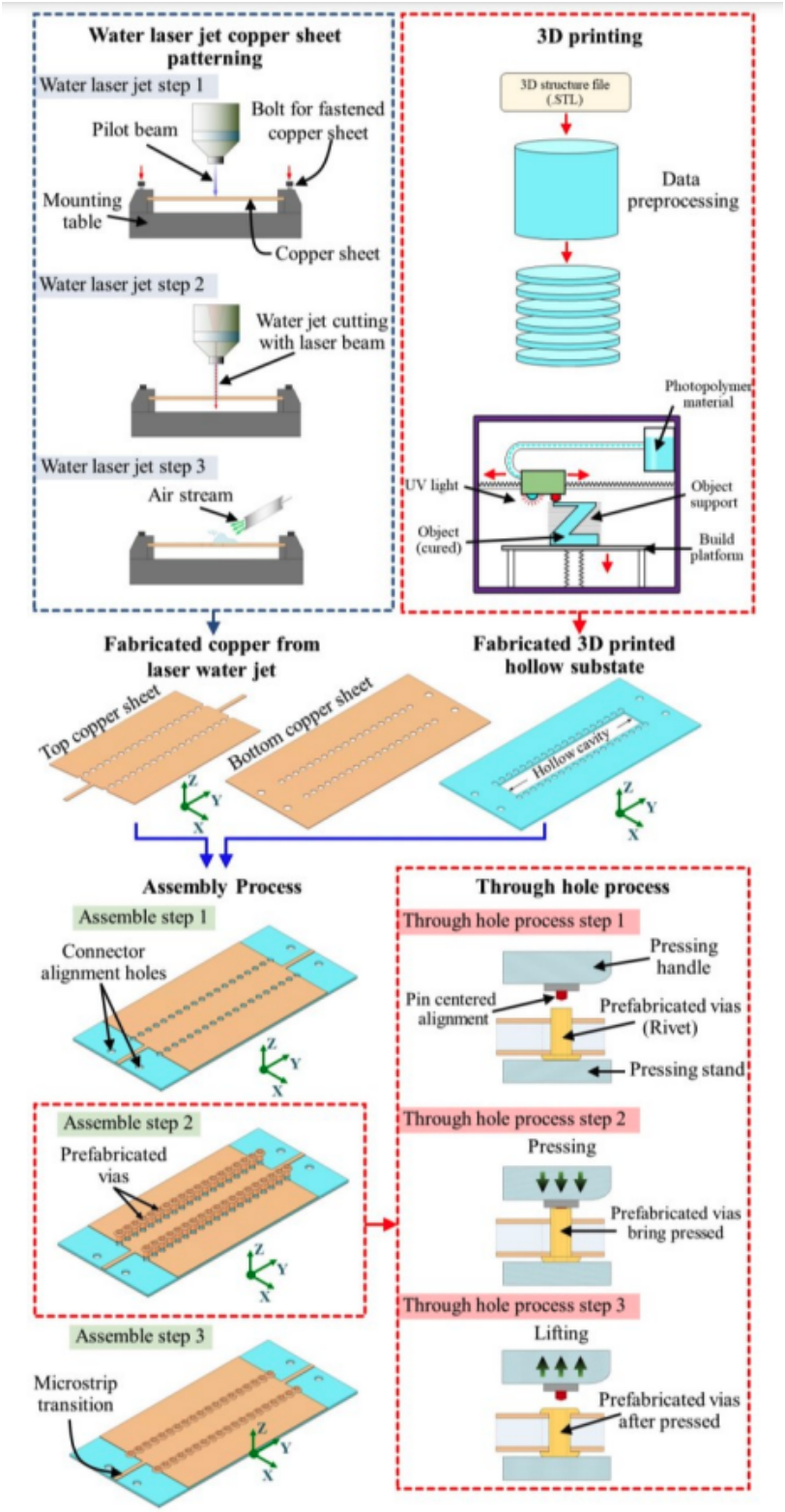

Figure 2.2: Process flow for 3D printed substrate, top and bottom copper sheet patterning and HSIW integration process

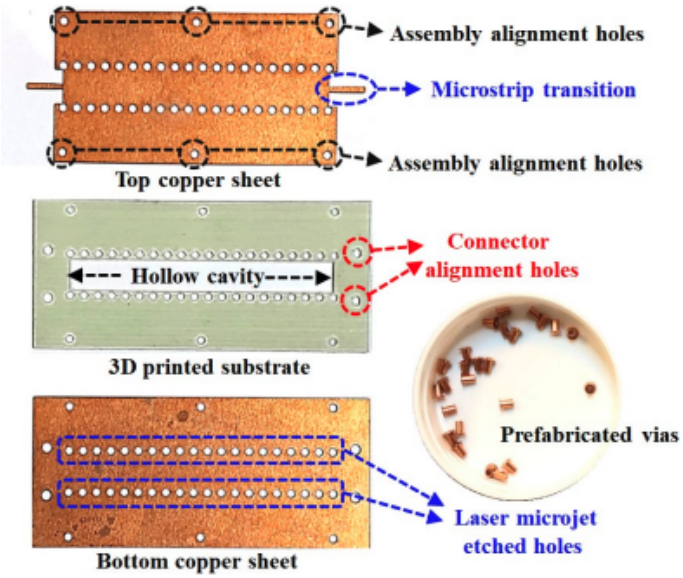

Figure 2.3: Fabricated HSIW prototype before assembly, which consists of the top copper sheet, 3D printed substrate, the bottom copper sheet and prefabricated vias

2.4.1 Copper Sheet Fabrication

The copper sheets, supplied by Goodfellow [30], were patterned using the laser cutter. The Synova MCS 300 has an emitted power up to 100 W and water pressure up to 500 bar and is powerful enough to process metals, such as super alloys, aluminum, copper, stainless steel, nickel, titanium, and so on. It also provides high-precision cutting, with a beam diameter up to 30 μm. The accuracy of the machine is ± 1 μm with repeatability ± 1 μm. The laser cutter operates by using a jet of deionized and filtered water to guide the laser beam via total internal reflection, helping to cool the sample and remove debris. With the laser beam having minimum losses, it is possible to keep the material sample further from the emitted laser beam. According to Synova [33],the beam can be placed at up to 10 cm range, as opposed to a conventional laser beam cutter that has a limited working distance. The copper fabrication process starts by placing and fastening the copper sheet sample on the mounting table, as shown in Fig. 2.2, step I. A pilot beam is emitted by the laser cutter to analyze the material and its dimensions. In step II, the water-jet laser cutter starts emitting the water laser beam that is cutting the copper sheet to the required shape, and finally, in step III, the air steam is activated to remove the remaining water on the surface of the copper sheet. The water-jet laser cutter has offered a very precise cut to the thin copper sheets. The fabricated copper sheets can be seen in Fig. 2.3, and these forms the enclosing top and bottom walls of the HSIW structure.

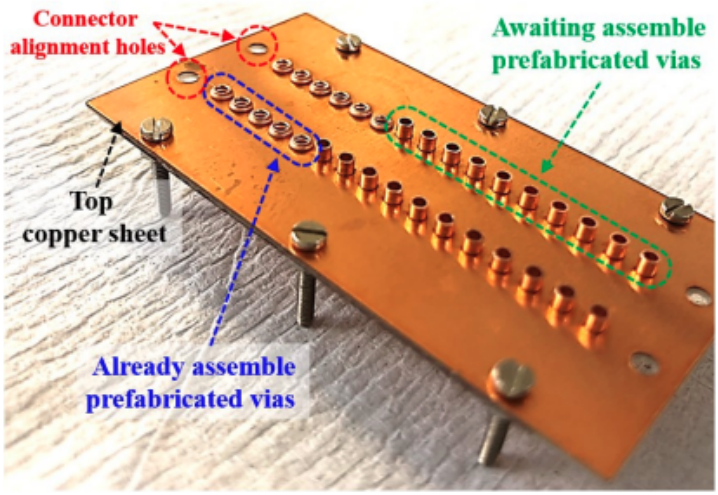

Figure 2.4: Fabricated HSIW with prefabricated vias inserted through the via holes

2.4.2 Dielectric Substrate Fabrication

Stratasys's Digital ABS Plus material [34] was chosen for the design and fabrication of the 3-D printed substrate, which forms the core of the HSIW. This ABS material provides high flexural strength of 65–75 MPa and tensile strength of 55–60 MPa that these offer a new degree of design freedom for applications benefiting from the use of conformal and flexible structures in the future. The ABS material has a dielectric constant of $\epsilon r = 2.75$ and a loss tangent of $\tan\delta = 0.025$ [1], [35]–[37]. The dielectric component was fabricated using the Objet 1000 3-D printer [38], which uses poly-jet printing technology. The lateral dimensional accuracy of the machine is up to 600 μm and the smallest thickness in each deposited layer is 16 μm. The geometry of the HSIW, after being designed and analyzed in the EM solver CST Studio [32], is exported in stereolithographic (STL) format for the Objet Studio software, which comes with the Objet 1000 Plus 3-D printer. In this software, the user assigns materials to the assembly's components and the build file are sent to the printer. The model material container of the 3-D printer is filled with the photopolymer resin, that is ABS material for this work, and the support material container is filled with water soluble polymer. The print heads can then start jetting the model and the support materials onto the build tray. The machine carries on jetting droplets until it builds the complete 3-D layer, and the UV light on top of the platform is emitted to cure the layer into a solid and strong material. The process is repeated until all the layers overlap to form the final 3-D structure. At the end, the water-soluble material is washed away, leaving behind the 3-D printed part. The fabricated dielectric substrate of the HSIW is shown in Fig. 2.3.

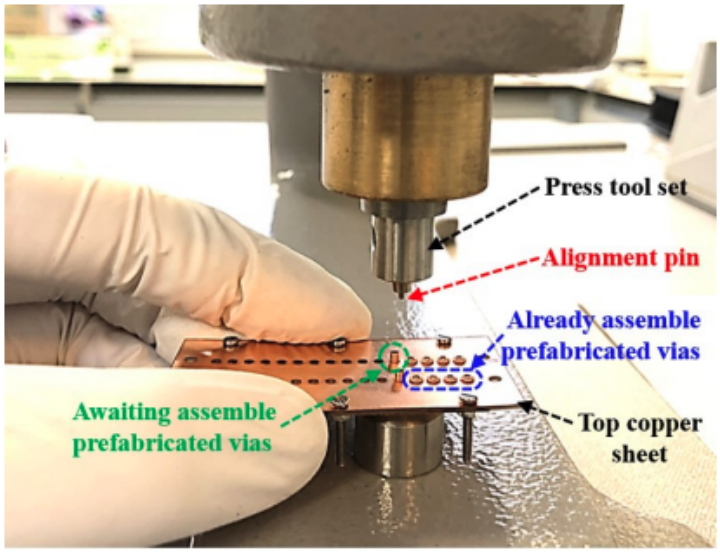

Figure 2.5: Assembly process of the proposed HSIW, by using the Mechanical Through Hole Plating method

2.4.3 Assembly

To construct the HSIW, the fabricated structures of the dielectric ABS and copper sheets are integrated. The three layers with sequence of top copper sheet, 3-D printed substrate, and bottom copper sheet are attached using the Fortex Mechanical PCB THP machine and copper rivets [31]. First, the copper rivets, which are the outer diameter of 1.6 mm, are inserted through the via holes of the three layers, as shown in Fig. 2.2. This is done for all via holes, as shown in Fig. 2.4. After that, the THP is pressing the copper rivets until they shrink to permanently fix the three surfaces together as shown in steps at Fig. 2.2. The assembly process as performed in the University of Leeds laboratory can be seen in Fig. 2.5. After all the copper rivets are pressed and fixed, at each end of the structure, a SOUTHWEST 2.4-mm connector is attached for connection to the measurement system.

2.5 Results

An Agilent (now Keysight) Technologies E8361A PNA 67-GHz vector network analyzer was used to measure the samples, as shown in the setup in Fig. 2.6. By following the multiline calibration method as described in [39], it is possible to extract the propagation constant by manipulating the scattering parameters of two HSIW devices of different lengths. A twoport coaxial short-open-load-through (SOLT) calibration was used to set the reference planes at the ends of the cables and remove as many errors as possible. The frequency range of 15–40 GHz was chosen, with 3200 points, for the S-parameter measurements. The measured propagation losses were

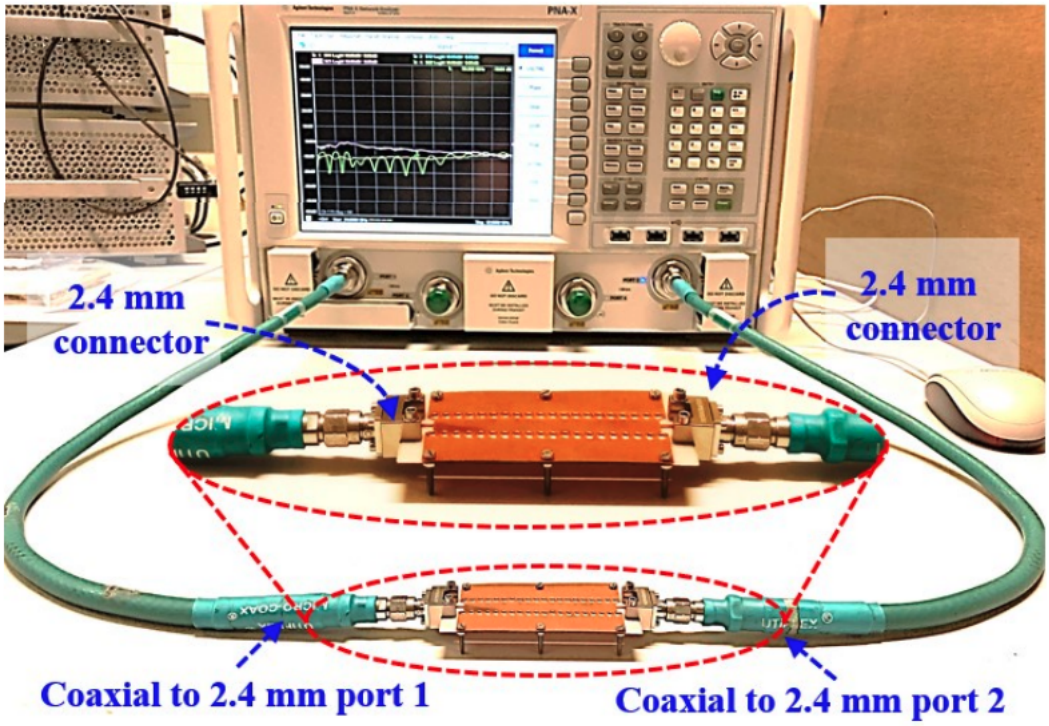

Figure 2.6: Measurement of Scattering parameters on Agilent E8361A PNA

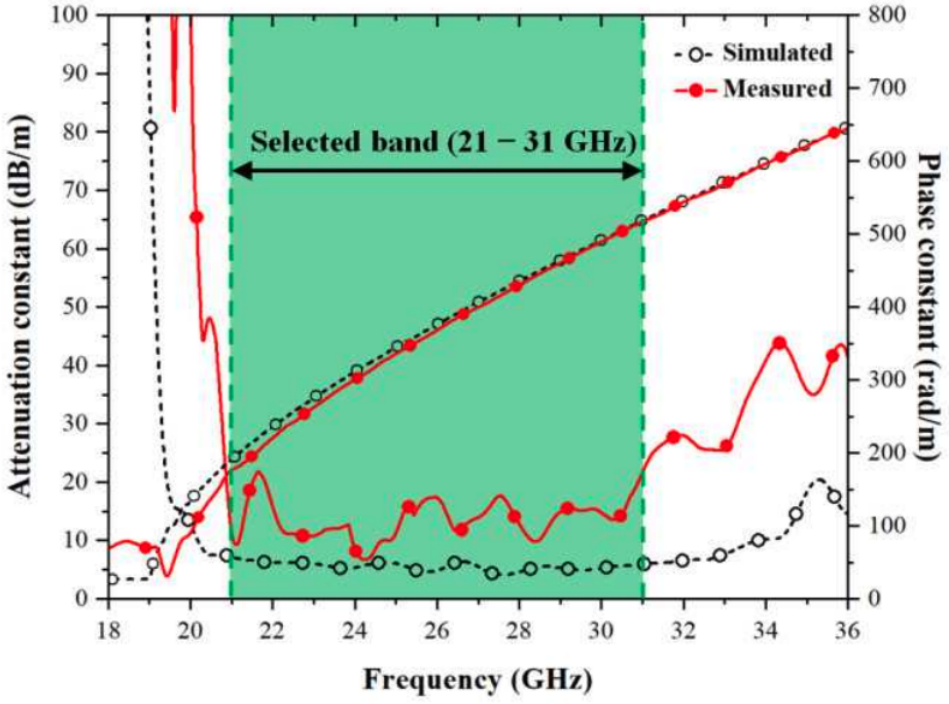

Figure 2.7: Simulated and measured propagation loss

calculated from the two S-parameter files and are plotted in Fig. 2.7, along with the results from the CST Studio simulation. There is some deviation of the measurement against the simulated attenuation constant. This difference is caused by the fabrication tolerances like surface roughness of the dielectric. Also, the assembly process caused some variations since the process was implemented manually; the use of PCB mechanical through-hole-press method has meant that the manual force was variable and the three layers were not attached precisely. The deviation can be up to 9 dB/m for some frequencies. Beyond 31 GHz, there is a significant increase in the attenuation constant, and so the HSIW is presented as have an operating range of 21–31 GHz. Overall, the designed HSIW achieves for the selected band of operation with an exceptionally low propagation loss of 13.55 dB/m (0.01355 dB/mm), which is one of the lowest values reported among other state-of-the-art designs, as summarized in reference [11].

2.6 Discussion

Fig. 2.8(a) shows the cross-sectional drawing in the xz plane before assembly. After pressing the prefabricated vias to fix the three surfaces, Fig. 2.8(b) shows the cross-sectional drawing in the xz plane after assembly, including the bending effect from the over pressing force of the THP machine. Fig. 2.9 shows the attenuation constant versus frequency when varying the diameter of the vias, D, from 1.6 to 2.0 mm in step of 0.2 mm and height of the hollow substrate, h, from 0.50 to 0.45 mm in step of 0.025 mm. The results show that the diameter of via does affect the cutoff frequency. The bigger diameter gives a higher cutoff frequency, which is to be expected. On the other hand, the variation in hollow substrate height has only a small effect on propagation loss. For SIW design, the frequency limit is dictated by design limitations and fabrication limitations. The main design limitation relates to the diameter of the vias and the distance between them [40]. In the practical case, the selected diameter of prefabricated vias depends on available diameter sizes that are available in the market [41]. In this article, the HSIW is designed and fabricated for operating at 21–31 GHz. We choose the via diameter of 1.6 mm, which is satisfactory for use in this band. However, at higher frequencies, the required diameter of vias is very small. We can change the technique for creating the via as reported in [42].

2.7 Future Work

The method of rapid prototyping HSIW-based millimetre-wave components using a combination of additive and SM processes has proved effective. The proposed

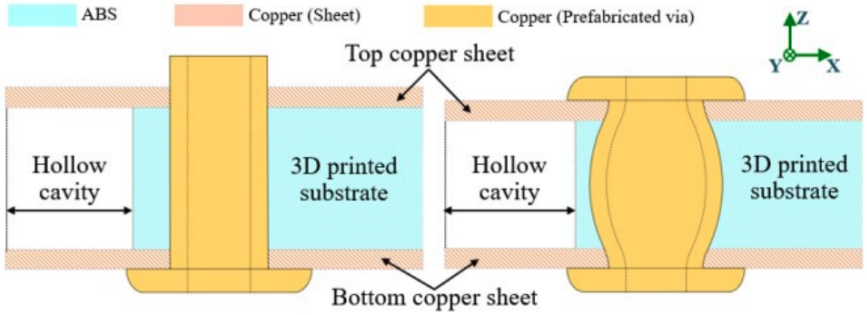

Figure 2.8: Cross section drawing XZ plane (a) before assembly and (b) after assembly

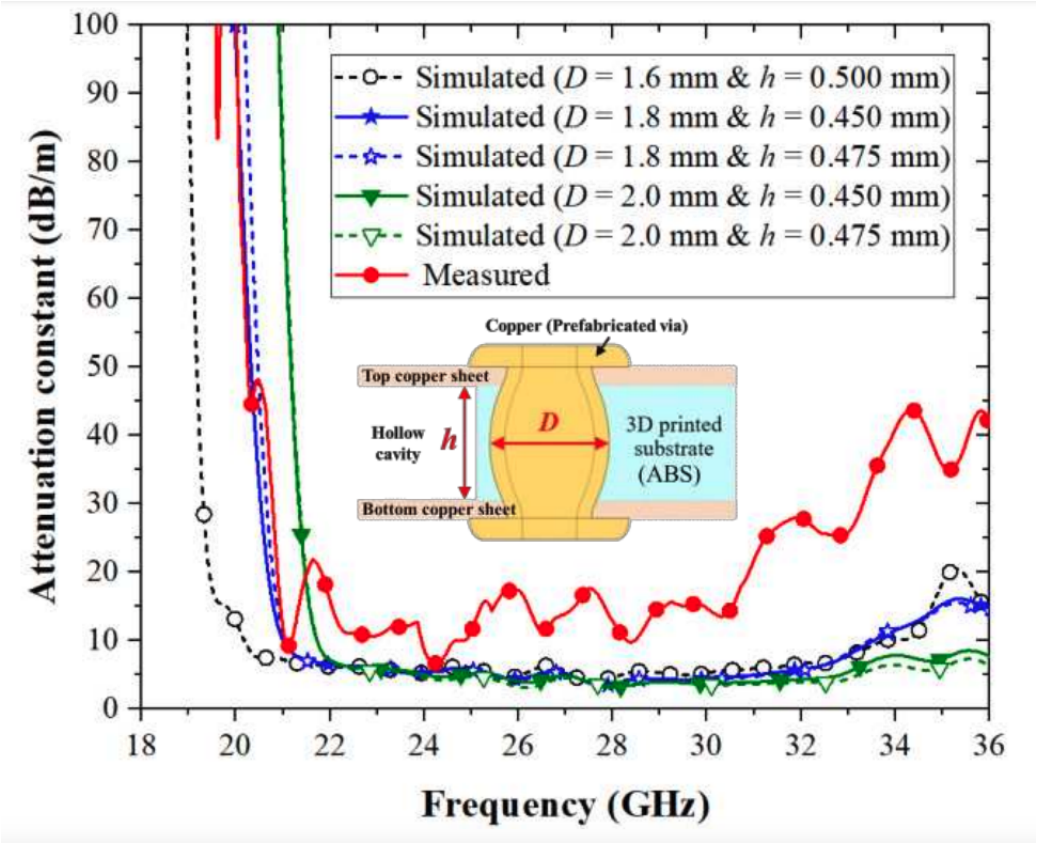

Figure 2.9: Simulated results of the bending effect by varying the diameter of the vias, D, and height of the hollow substrate, h

technique has advantages in the ease of design, low fabrication, and material cost, requires no chemical processing, and can be used to realize a new class of microwave- and millimetre-wave components with the possibility of conformal and flexible structures [43]. However, this method was necessary for fabricating the prototype components for testing the performance before considering mass production. This work has proved the concept, but further work is required to further automate the process to reduce the tolerance of the assembly processes. For example, controlling the pressed force of the mechanical head during assembly and using automatic stepping motors to align the center of the prefabricated vias before pressing. When comparing with a PCB process, the fabrication of through substrate vias in the PCB process is very problematic since the via diameter is very small, and thus, the metallization process of filling or covering sidewall of the via with copper is very difficult, unreliable, and very costly and requires very sophisticated machines to achieve the task.

2.8 Summary

In this paper, a new method for fabricating an HSIW waveguide at millimetre-wave frequencies has been demonstrated, using a combination of additive and SM techniques. These methods provide fast development and assembly and low-cost fabrication, compared to other methods, which can be extremely costly and require specialist facilities. The methods obviate the need to use any chemical processing, which is particularly advantageous as health, safety, and environmental legislation rightly impose ever greater requirements on laboratory management. The additive manufacturing process provides enhanced flexibility in choosing the dielectric material to be used as the hollow substrate. It has advantages of stability, ease of design, low-cost, lightweight, and the possibility for mechanical flexibility. It offers a new degree of design freedom for applications benefiting from the use of conformal and flexible structures. Specifically, the material jetting 3-D printing technology provides the opportunity to choose from hundreds of materials and they can be mixed to produce composite 3-D materials for a number of important new millimetre-wave components. Finally, the propagation constant results show an average 12.5% difference between simulations and measurements over the operating frequency range. A very low attenuation constant of 13.55 dB/m (0.01355 dB/mm) is achieved for the whole operating frequency range of 21–31 GHz.

2.9 References

[1] N. Duangrit, B. Hong, A. D. Burnett, P. Akkaraekthalin, I. D. Robertson, and N. Somjit, "Terahertz dielectric property characterization of photopolymers for additive manufacturing," IEEE Access, vol. 7, pp. 12339–12347, 2019.

[2] J. D. Kechagias and S. Maropoulos, "An investigation of sloped surface roughness of direct poly-jet 3D printing," in Proc. Int. Conf. Ind. Eng., 2015, pp. 150–153.

[3] A. Kampker, K. Kreisköther, and C. Reinders, "Material and parameter analysis of the PolyJet process for mold making using design of experiments," Int. J. Chem., Mol., Nucl., Mater. Metall. Eng., vol. 11, no. 3, pp. 242–249, 2017.

[4] V. W. Sahana and G. T. Thampi, "3D printing technology in industry," in Proc. 2nd Int. Conf. Inventive Syst. Control (ICISC), Jan. 2018, pp. 528–533.

[5] J. Li, Y. Wang, J. He, H. Liu, and G. Xiang, "Rapid production of customised electronic systems via multifunctional additive manufacturing technology," in Proc. IEEE 3rd Int. Conf. Integr. Circuits Microsyst. (ICICM), Nov. 2018, pp. 298–301.

[6] N. Chudpooti, N. Duangrit, P. Akkaraekthalin, I. D. Robertson, and N. Somjit, "220–320 GHz hemispherical lens antennas using digital light processed photopolymers," IEEE Access, vol. 7, pp. 12283–12290, 2019.

[7] B. Hong et al., "Low-loss asymptotically single-mode THz Bragg fiber fabricated by digital light processing rapid prototyping," IEEE Trans. THz Sci. Technol., vol. 8, no. 1, pp. 90–99, Jan. 2018.

[8] B. Hong, M. Swithenbank, N. Somjit, J. Cunningham, and I. Robertson, "Asymptotically single-mode small-core terahertz Bragg fibre with low loss and low dispersion," J. Phys. D, Appl. Phys., vol. 50, no. 4, 2017, Art. no. 45104.

[9] Z. Wu, M. Liang, W.-R. Ng, M. Gehm, and H. Xin, "Terahertz horn antenna based on hollow-core electromagnetic crystal (EMXT) structure," IEEE Trans. Antennas Propag., vol. 60, no. 12, pp. 5557–5563, Dec. 2012.

[10] X. Yu et al., "Exploring THz band for high speed wireless communications," in Proc. 41st Int. Conf. Infr., Millim., THz Waves (IRMMW-THz), Sep. 2016, pp. 1–2.

[11] G. Savvides et al., "3D rapid-prototyped 21–31-GHz hollow SIWs for low-cost 5G IoT and robotic applications," IEEE Access, vol. 9, pp. 11750–11760, 2021.

[12] N. Chudpooti et al., "In-situ self-aligned NaCl-solution fluidic-integrated microwave sensors for industrial and biomedical applications," IEEE Access, vol. 8, pp. 188897–188907, 2020.

[13] B. T. Malik, V. Doychinov, S. A. R. Zaidi, I. D. Robertson, and N. Somjit, "Antenna gain enhancement by using low-infill 3D-printed dielectric lens antennas," IEEE Access, vol. 7, pp. 102467–102476, 2019.

[14] N. Chudpooti, N. Duangrit, P. Akkaraekthalin, I. D. Robertson, and N. Somjit, "Electronics-based free-space terahertz measurement using hemispherical lens antennas," IEEE Access, vol. 7, pp. 95536–95546, 2019.

[15] B. Andres-Garcia et al., "Gain enhancement by dielectric horns in the terahertz band," IEEE Trans. Antennas Propag., vol. 59, no. 9, pp. 3164–3170, Sep. 2011.

[16] E. Lacombe et al., "Low-cost 3D-printed 240 GHz plastic lens fed by integrated antenna in organic substrate targeting sub-THz high data rate wireless links," in Proc. IEEE Int. Symp. Antennas Propag. USNC/URSI Nat. Radio Sci. Meeting, Jul. 2017, pp. 5–6.

[17] K. Y. Chan, R. Ramer, and R. Sorrentino, "Low-cost Ku-band waveguide devices using 3-D printing and liquid metal filling," IEEE Trans. Microw. Theory Techn., vol. 66, no. 9, pp. 3993–4001, Sep. 2018.

[18] G. Mitchell, T. Anthony, Z. Larimore, and P. Parsons, "Antenna comparison for additive manufacturing versus traditional manufacturing methods," in Proc. United States Nat. Committee URSI Nat. Radio Sci. Meeting (USNC-URSI NRSM), Jan. 2021, pp. 3–4, doi: 10.23919/USNC-URSINRSM51531.2021.9336492.

[19] G. Mitchell, Z. Larimore, and P. Parsons, "Additive manufacturing of a dual band, hybrid substrate, and dual polarization antenna," in Proc. Int. Appl. Comput. Electromagn. Soc. Symp. (ACES), Jul. 2020, pp. 1–2,
doi: 10.23919/ACES49320.2020.9196147.

[20] V. Gjokaj, J. Papapolymerou, J. Albrecht, and P. Chahal, "Design and fabrication of additively manufactured hybrid rigid-flex RF components," IEEE Trans. Compon., Packag., Manuf. Technol., vol. 9, no. 4, pp. 779–785, Apr. 2019, doi: 10.1109/TCPMT.2019.2900210.

[21] X. Yu et al., "3-D printed parts for a multilayer phased array antenna system," IEEE Antennas Wireless Propag. Lett., vol. 17, no. 11, pp. 2150–2154, Nov. 2018, doi: 10.1109/LAWP.2018.2873116.

[22] J. Bito, R. Bahr, J. G. Hester, S. A. Nauroze, A. Georgiadis, and M. M. Tentzeris, "A novel solar and electromagnetic energy harvesting system with a 3-D printed package for energy efficient Internet-ofThings wireless sensors," IEEE Trans. Microw. Theory Techn., vol. 65, no. 5, pp. 1831–1842, May 2017, doi: 10.1109/TMTT.2017.2660487.

[23] M. Mirzaee, S. Noghanian, L. Wiest, and I. Chang, "Developing flexible 3D printed antenna using conductive ABS materials," in Proc. IEEE Int. Symp. Antennas Propag. USNC/URSI Nat. Radio Sci. Meeting, Jul. 2015, pp. 1308–1309.

[24] N. Chudpooti, E. Silavwe, P. Akkaraekthalin, I. D. Robertson, and N. Somjit, "Nano-fluidic millimeter-wave lab-on-a-waveguide sensor for liquid-mixture characterization," IEEE Sensors J., vol. 18, no. 1, pp. 157–164, Jan. 2018.

[25] E. Silavwe, N. Somjit, and I. D. Robertson, "A microfluidic-integrated SIW lab-on-substrate sensor for microliter liquid characterization," IEEE Sensors J., vol. 16, no. 21, pp. 7628–7635, Nov. 2016.

[26] I. E. Obuh, V. Doychinov, D. P. Steenson, P. Akkaraekthalin, I. D. Robertson, and N. Somjit, "Low-cost microfabrication for MEMS switches and varactors," IEEE Trans. Compon., Packag., Manuf. Technol., vol. 8, no. 9, pp. 1702–1710, Sep. 2018.

[27] N. Chudpooti, V. Doychinov, P. Akkaraekthalin, I. D. Robertson, and N. Somjit, "Non-invasive millimeter-wave profiler for surface height measurement of photoresist films," IEEE Sensors J., vol. 18, no. 8, pp. 3174–3182, Apr. 2018, doi: 10.1109/JSEN.2018.2806185.

[28] B. Hong et al., "Substrate integrated Bragg waveguide: An octavebandwidth single-mode hybrid transmission line for millimeter-wave applications," Opt. Exp., vol. 28, no. 19, pp. 27903–27918, 2020.

[29] N. B. M. Najib, N. Somjit, and I. Hunter, "Design and characterisation of dual-mode suspended-substrate stripline filter," IET Microw., Antennas Propag., vol. 12, no. 9, pp. 1526–1531, Jul. 2018.

[30] GoodFellow. Accessed: Jan. 6, 2021. [Online]. Available: http://www. goodfellow.com/

[31] Fortex PTH400. Accessed: Jan. 6, 2021. [Online]. Available: http://www. fortex.co.uk/download/pth400-mechanical-through-hole-press/

[32] Dassault Systèmes. CST Studio Suite. Accessed: Jan. 6, 2021. [Online]. Available: https://www.3ds.com/products-services/simulia/products/cststudio-suite/

[33] Synova Laser Microjet: Water Jet Guided Laser Technology. Accessed: May 18, 2021. [Online]. Available: https://www.synova.ch/ technology/laser-microjet.html

[34] Digital ABS Plus. Accessed: Jan. 6, 2021. [Online]. Available: https://www.stratasys.com/materials/search/digital-abs-plus

[35] C.-K. Lee et al., "Evaluation of microwave characterization methods for additively manufactured materials," Designs, vol. 3, no. 4, p. 47, Sep. 2019.

[36] J. Pourahmadazar and T. A. Denidni, "Towards millimetre-wavelength: Transmission-mode Fresnel-zone plate lens antennas using plastic material porosity control in homogeneous medium," Sci. Rep., vol. 8, no. 1, Dec. 2018, Art. no. 5300.

[37] H. Xin and M. Liang, "3-D-printed microwave and THz devices using polymer jetting techniques," Proc. IEEE, vol. 105, no. 4, pp. 737–755, Apr. 2017.

[38] OBJET1000 PLUS. Accessed: Jan. 6, 2021. [Online]. Available: https://www.stratasys.com/3d-printers/objet1000-plus

[39] R. B. Marks, "A multiline method of network analyzer calibration," IEEE Trans. Microw. Theory Techn., vol. 39, no. 7, pp. 1205–1215, Jul. 1991.

[40] F. Xu and K. Wu, "Guided-wave and leakage characteristics of substrate integrated waveguide," IEEE Trans. Microw. Theory Techn., vol. 53, no. 1, pp. 66–73, Jan. 2005.

[41] Fortex PTH400. Accessed: Jul. 31, 2021. [Online]. Available: http://www.fortex.co.uk/product/favorit-through-hole-mechanical-plating/

[42] S. J. Bleiker et al., "High-aspect-ratio through silicon vias for highfrequency application fabricated by magnetic assembly of gold-coated nickel wires," IEEE Trans. Compon., Packag., Manuf. Technol., vol. 5, no. 1, pp. 21–27, Jan. 2015.

[43] A. C. Fischer et al., "High aspect ratio TSVs fabricated by magnetic self-assembly of gold-coated nickel wires," in Proc. IEEE 62nd Electron. Compon. Technol. Conf., May 2012, pp. 541–547, doi: 10.1109/ECTC.2012.6248882.

Chapter 3

3D Rapid-Prototyped 21-31-GHz Hollow SIWs for Low-Cost 5G IoT and Robotic Applications

Published in IEEE ACCESS

https://ieeexplore.ieee.org/document/9320482

GIORGOS SAVVIDES, NATTAPONG DUANGRIT, (Member, IEEE), NONCHANUTT CHUDPOOTI, (Member, IEEE), PRAYOOT AKKARAEKTHALIN, (Member, IEEE), ULRIK IMBERG, IAN D. ROBERTSON, (Fellow, IEEE), AND NUTAPONG SOMJIT, (Senior Member, IEEE)

3.1 Abstract

This article presents, for the first time, new design and fabrication techniques for Hollow Substrate Integrated Waveguides (HSIWs), demonstrated in the nominal frequency from 21 to 31 GHz, for use in wireless communication applications such as 5G, IoT and robotics. The design and fabrication techniques introduced in this paper feature: 1) the use of low-cost rapid prototyping additive manufacturing based on polymer jetting (PJ), and 2) the use of commercially available through-substrate copper via transitions. In contrast to the conventional SIW designs and fabrications, this new approach does not rely on through-substrate via fabrication, hence avoiding some difficult manufacturing steps, such as through-substrate etching, via formation and via metallization, which are considered complex and expensive to implement. The 3D printed HSIWs in this article can achieve a propagation loss of lower than 1.56 Np/m (13.55 dB/m), which is considered one of the results with the lowest

propagation loss achieved to date, when compared to the state-of-the-art.

3.2 Introduction

Transmission lines are crucially important in many high frequency applications and are used in RF, microwave, millimetre-wave (mmWave) and terahertz systems. There are many types of transmission line structures such as rectangular waveguide (RWG), coaxial cable, microstrip line, stripline, coplanar waveguide (CPW) and, more recently, substrate integrated waveguide (SIW) [1]–[8]. RWGs generally provide many advantages compared to the other conventional transmission line types, such as extremely low propagation loss, high power-handling capability and superior measurement repeatability for many precision test applications. However, they are relatively bulky and cannot easily be integrated with active devices and integrated circuits to realize wireless communications transceivers in mass production. Coaxial lines are widely used as interconnections between high frequency components/devices working up to a few hundreds of GHz but they are also not suitable for integration with high frequency integrated circuits and subsystems such as RFICs or MMICs [1], [3]. Microstrip and CPW are extensively used in integrated circuit technologies because they provide a low-cost and planar solution, are simple to fabricate, and convenient for integration with both passive and active circuit devices [4]–[8]. Recently, SIWs have attracted a great deal of research interest and industrial development because they combine these advantages with some of the performance capabilities of RWG: They have low physical profile, high Q-factor, good power-handling capability and are easy to integrate with other planar circuits, active devices and integrated circuits [9]– [11]. SIWs can outperform other planar transmission line technologies, such as microstrip or CPW, because of their lower propagation loss and higher power-handling capability. Moreover, microstrip and CPW structures have undesired electromagnetic (EM) radiation and usually suffer from signal dispersion at millimetre-wave and terahertz frequencies, which can significantly degrade the efficiency and performance of functional components [12]–[15]. In [16], SIW is shown to have similar propagation characteristics and performance when compared to the conventional RWG. The mode of electromagnetic (EM) wave propagation inside an SIW resembles that used in a conventional RWG. Its loss mechanisms are similar and loss is attributed to three factors: finite metal conductivity (α_c), dielectric loss (α_d) and radiation leakage (α_r). There are two main types of SIW that have been reported during the last decade [17]–[20]: 1) dielectric-filled, which is most common, and 2) hollow substrate integrated waveguide (HSIW). In [20], a slot antenna demonstrated based on a dielectric-filled SIW structure using

the electrode position fabrication was presented. It consists of very thin and closely spaced metallic wires to reduce the leakage loss but the propagation loss was compromised due to the lossy dielectric substrate. Generally, the main reason to select HSIWs over dielectric filled SIWs is due to the dielectric loss of the substrate used to fill the waveguide cavity. There are many research works that developed the HSIW-based functional devices by removing the dielectric material inside the waveguide structures [21]–[29], e.g. by using a multi-layered printed circuit board (PCB) structures. Moreover, the HSIWs can preserve many advantages inherited from SIWs and RWG, such as high level of system and circuit integration as well as high Q-factor and high power-handling capability [30], [31]. In [23], HSIW was used in a multilayer U-band phase shifter, fabricated using a standard PCB process, showing a significant improvement in the attenuation; from 40 dB/m to only 12.2 dB/m. Similarly, in [24], an air-filled SIW (AFSIW) fabricated using a standard multilayer PCB process, with a lossy FR-4 substrate, was demonstrated at 27-40 GHz and achieved a measured attenuation constant as low as 0.51 Np/m (4.43 dB/m). In general, air-filled SIWs have low transmission losses but require more complex manufacturing processes and are particularly dependent on through-substrate via-hole fabrication which implies higher fabrication cost. For example, the HSIWs in [25] and [26] used very costly low-temperature co-fired ceramic (LTCC) processes, which suffer from high fabrication and material costs as well as thermal shrinkage of substrates, drastically reducing the fabrication reliability and accuracy. In [26], an average attenuation constant of as low as 17.37 dB/m or 2 Np/m was reported. In [27], an "empty" SIW was demonstrated with an exceptional transmission loss of 0.8 Np/m at 19.5 GHz by completely removing all dielectric material in the structure using the standard PCB fabrication process. However, all reported HSIWs used PCB, LTCC or similar fabrication techniques that rely heavily on through-substrate transitions and vias, resulting in higher manufacturing cost and a complex fabrication process, especially at millimetre-wave frequencies and beyond. In [32], the metallic vertical walls of the traditional SIW were replaced by using a Bragg structure, reducing the overall propagation loss but the fabrication method is complex and the fabrication costs are comparatively large. This article presents a novel design and fabrication approach for realizing HSIW at low cost by using a simple fabrication process that combines two manufacturing techniques: 1) additive manufacturing based on polymer jetting (PJ), and 2) integration of commercially-available prefabricated through-substrate copper via transitions. The 3D-printed HSIWs demonstrated in this article cover the operational frequency range from 21 to 32 GHz, which covers many of the wireless communication frequency bands used for 5G, IoT and robotics. The novel design and fabrication approach has several advantages when compared to conventional fabrication techniques such as PCB, LTCC and cleanroom processes. Firstly, additive

manufacturing techniques have been proven to be very useful for the low-cost rapid-prototyping of high-frequency components from only a few MHz to THz [33]–[38]. Secondly, by using the commercially available prefabricated through-substrate via transitions, the manufacturing of through vias can be massively simplified, which is in contrast to the conventional fabrication processes that require many complicated fabrication steps such as through-substrate etching, via forming and electroplating to metallize the through-substrate via-holes. Thirdly, since the through-substrate vias are already prefabricated, the reliability of the through-substrate vias and the fabrication of the vias are highly reliable, resulting in high fabrication yields.

3.3 Analysis, Design and Fabrication

3.3.1 State-of-the-art 3D printing techniques

As comprehensively reported [39], 3D printing techniques are generally classified into five categories: fused deposition modeling (FDM), stereolithography apparatus (SLA), digital light processing (DLP), selective laser sintering (SLS), and polymer jetting (PJ). The FDM technique uses thermoplastic materials, which come in filament form. This technique constructs the model by depositing the melted filaments along pre-determined paths. This technique results in the lowest printing resolution and high surface roughness. The standard layer heights of a single printed path range from 50 to 500 µm, which is limited by the nozzle size and the viscosity of the filament materials. However, material-extrusion based 3D printing techniques such as FDM are known to suffer voids within the printed parts [40]. The SLA and DLP techniques use a light source to pattern a 3D structure by selectively curing resin-based photopolymer. The light sources of the SLA and DLP techniques are a laser beam and an ultraviolet light, respectively. The resolution of these techniques depends on the spot size used to pattern the 3D structure. The best printing resolutions of the structure height for the SLA and DLP techniques are typically 25 µm and 1 µm, respectively. A surface roughness of less than 10 µm can be achieved by these techniques. The SLS technique patterns a polymeric powder material layer-by-layer using a high-intensity laser beam for selective sintering. The best printing resolution for the SLS technique is typically 20 µm for the structure height. The printing resolution depends on the microparticle size of the powder material. However, this technique has a very limited choice of materials for the microparticle powders, limiting its use for microwave and mm-wave applications.

The PJ technique provides the best printing accuracy and resolutions compared with the other four techniques. This technique is like inkjet printing because it uses a

nozzle head to drop liquid photopolymer onto the printing area. The photopolymer materials are cured by UV light to create the 3D patterned structure step-by-step. The best printing resolution is approximately 14 µm for the structure height. The surface roughness is less than 10 µm. For this work, the PJ technique was selected for fabricating the HSIW because this technique provides the best printing accuracy and resolution and offers the smallest surface roughness, while still achieving low fabrication cost.

3.3.2 Theoretical Analysis and Design

The detailed geometry of the novel 3D printed HSIW is depicted in Fig. 3.1. Fig. 3.1(a) represents the 3D exploded view of the HSIW structure consisting of four different parts: (1) the commercially prefabricated through-substrate copper via transitions, (2) the top copper sheet being laser-patterned and containing the microstrip feeds and microstrip-to-SIW transitions as well as circular etch-hole array, (3) the 3D printed substrate using standard acrylonitrile butadiene styrene (ABS), and (4) the laser-patterned bottom copper sheet with circular etch-hole array and microstrip grounds. Fabricated into the top copper sheet, 50-ohm microstrip lines are used as EM-mode transitions between the 2.4-mm coaxial connectors and the HSIW structures which have a characteristic impedance of 48-ohm [41].

The bottom copper sheet was also laser-patterned and contains the ground planes of the microstrip transitions and the circular etch-hole array to form the HSIW metal fence posts. The standard ABS 3D-printing material, with a dielectric constant, ϵ_r , of 2.75 and a loss tangent, tanδ, of 0.025 [39], [42]–[44], was used to fabricate the hollow substrate structure sandwiched with two aforementioned laser-patterned copper sheets on the top and bottom of the substrate. The substrate thickness, Ts , was selected to be 0.5 mm for the 3D-printed HSIWs, which is matched to the thickness of the ready made copper via transitions and offers ease of impedance matching between the microstrip transition and the HSIWs.

Commercially prefabricated through-copper via transitions were used to assemble and firmly attach all three previously fabricated parts by using the Through Hole Mechanical Press [45]. Figures 3.1(b) and 3.1(c), represent the top view and the cross-sectional view of the 3D-printed HSIW, respectively. The values of the design parameters are shown in Table 3.1. The HSIW structure and all microstrip transitions are designed and optimized by using the 3D full-wave EM simulation package CST Studio Suite [46]. The 3D-printed HSIW in this article was optimized for the operating frequency range of 21-31 GHz, which is suitable for many applications in high-speed 5G, IoT and robotic communications.

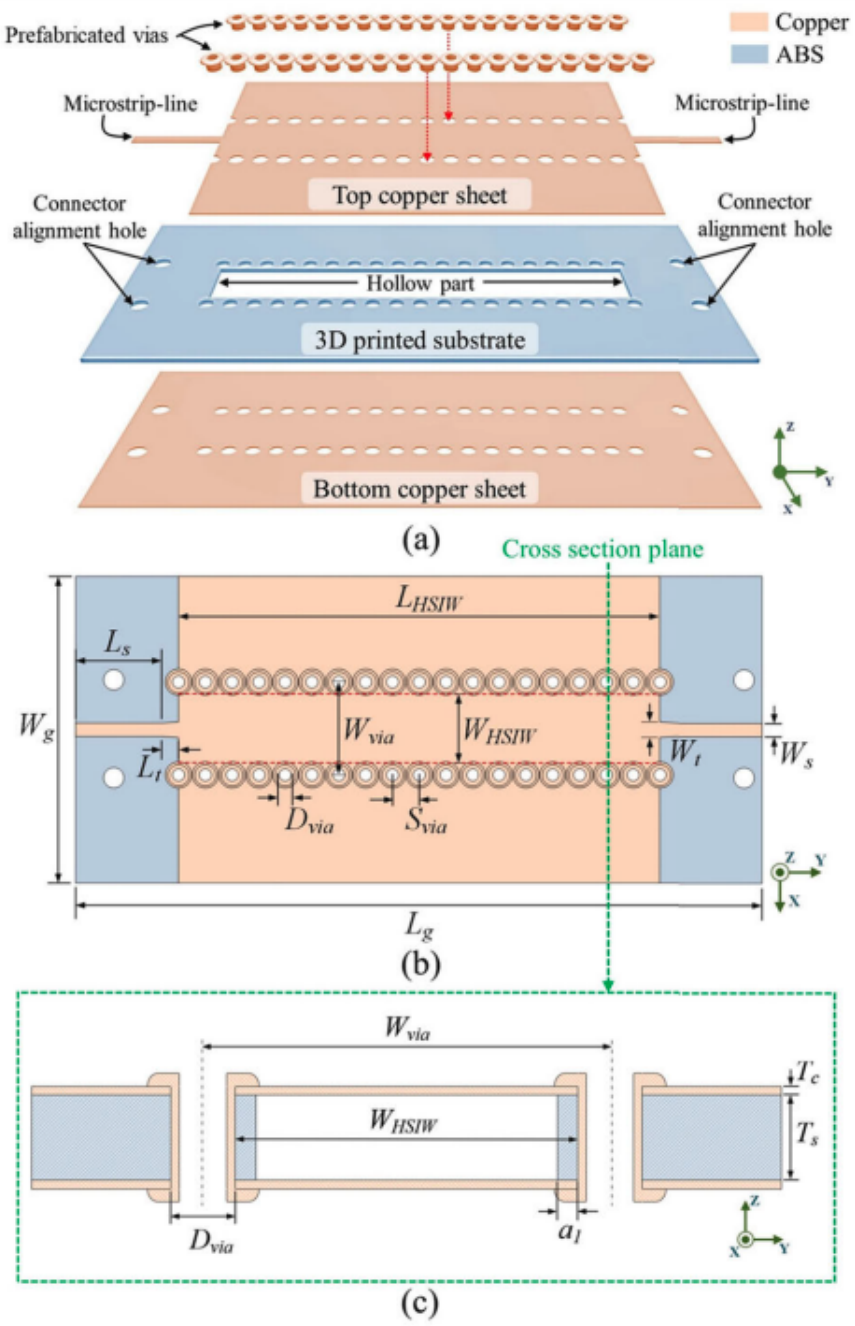

Figure 3.1: Schematic diagrams of the novel HSIW in this paper: (a) 3D exploded view, (b) top view with all design parameter, and (c) cross-sectional view of the HSIW

In [25], the theoretical analysis is investigated for the propagation mode inside a HSIW, which is an EM combination between the conventional RWG and SIW structures. The effect of the dielectric portion inside a hollow waveguide can be determined by defining a loading ratio, q, as shown in equation (3.1):

$$q = \frac{2a_1\sqrt{\varepsilon_r}}{W_{HSIW}} \tag{3.1}$$

Table 3.1: The Design Parameters of the HSIWs.

Parameter	Description	Value (mm)
W_s	Width of microstrip line	1.2
W_t	Width of a taper transition from microstrip line to HSIW	1.3
W_{via}	Distance between vias centers	9.0
W_{HSIW}	Width of HSIW	6.6
L_s	Length of microstrip line	8.0
L_t	Length of taper transition	2.0
L_{HSIW}	Length of HSIW	46.8, 52.0, 91.0
D_{via}	Diameter of via hole	1.2
S_{via}	Spacing between vias	2.6
T_c	Thickness of copper sheet	0.15
T_s	Substrate thickness	0.5
a_1	Width of the dielectric filling inside the HSIW	0.4

where a1 is the width of the dielectric filling inside the hollow SIW as shown in Fig. 3.1(c), ϵ_r is the dielectric constant of the substrate material, and WHSIW is the width of the HSIW structure. The lower the value of q, the more the structure behaves like the conventional RWG. According to [25], the maximum value of q used to design the HSIW should be lower than 0.35. The q of the 3D-printed HSIW was carefully determined by considering the fabrication resolution of the 3D printer used in this work, which can provide the minimum a1 of 0.4 mm and, therefore, the q value of 0.175 is calculated by using equation (3.1). The cutoff frequency of the 3D-printed HSIW is chosen to be 21 GHz to provide the operational frequency range of 21 to 31 GHz. Therefore, the WHSIW can be calculated by using equation (3.2): where c0 is the velocity of light in free space and fc is the cutoff frequency (Hz):

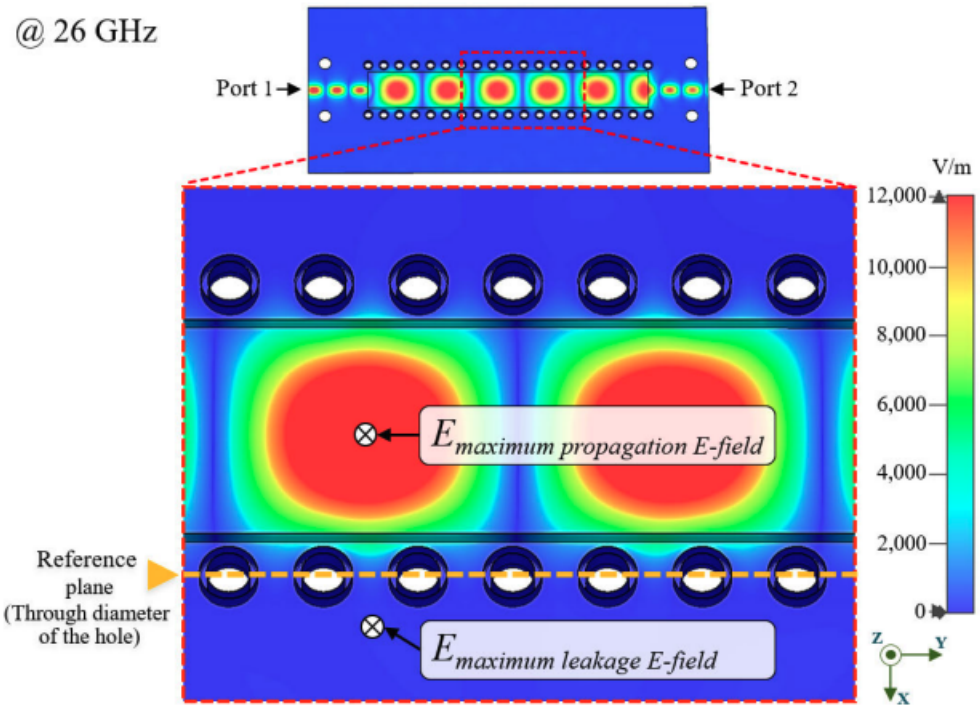

Figure 3.2: Electric field distribution at 26 GHz inside the proposed HSIW with the length of 46.8 mm.

$$W_{HSIW} = \frac{c_0}{2f_c\left[0.999 + 4.946 \times 10^{-4} \times e^{(9.406q)}\right]} \tag{3.2}$$

$$S_{via} \geq H_{via} \tag{3.3}$$

The readymade through-copper vias used in this work are offered by Fortex and have an outer diameter of 1.6 mm and an inner diameter, Dvia, of 1.2 mm [45]. The cap of the prefabricated copper vias have a diameter, Hvia, of 2.6 mm, therefore, the minimum spacing between two adjacent vias, Svia, can be calculated and chosen using equation (3.3), so the caps of the prefabricated vias will not collide with each other after fabrication. To minimize EM leakage losses through the substrate (α_r), the optimum space of 2.6 mm between two adjacent vias, Svia, was chosen.

Figure 3.2 illustrates the simulated electric field (E-filed) of the 3D-printed HSIW with a length of 46.8 mm at a frequency of 26 GHz, which is the center frequency of the selected frequency band. The ratio between the maximum guided E-field inside the hollow of the HSIW and maximum leaked E-field into the substrate of $7.275E-3$ is calculated, implying that the leaked E-field of the 3D-printed HSIW can be neglected.

An effective dielectric constant, ϵ_e, is a virtual dielectric parameter that combines the material properties of air and the dielectric substrate of the partially loaded RWG [25], [26]. The effective dielectric constant, ϵ_e, is calculated as follows:

$$\varepsilon_e = \varepsilon_0 \varepsilon_{r,eff} \left(1 - j \tan \delta_{eff}\right) \tag{3.4}$$

where, ϵ_0, which is permittivity of free space, is $8.85 \times 10^{-}12F \times m^{-}1$, $\epsilon_{r,eff}$ is effective relative permittivity and $tan\delta_eff$ is effective loss factor. As in [25] and [26], to calculate the effective dielectric constant, ϵ_e, it is necessary to first calculate the value of the effective permittivity, $\epsilon_{r,eff}$, and the normalized effective loss factor, $tan\delta_n$, as in equations (3.5) and (3.6):

$$\varepsilon_{r,\text{ eff}} = \frac{\beta^2 + \left(\frac{\pi}{W_{HSIW}}\right)^2}{k_0^2} \tag{3.5}$$

$$\tan \delta_n = \frac{\tan \delta_{eff}}{\tan \delta} = \frac{\varepsilon_r}{\varepsilon_{r,eff}} \left[1 + \frac{k_{x1}^2}{k_{x2}^2} \frac{a_2 + \sin\left(k_{x2} a_2\right)/k_{x2}}{a_1 - \sin\left(k_{x1} a_2\right)/k_{x1}} \frac{\cos^2\left(k_{x1} a_1/2\right)}{\sin^2\left(k_{x2} a_2/2\right)}\right]^{-1} \tag{3.6}$$

where, a_1 is the width of the dielectric filling inside the HSIW and a_2 is the width of the air filling inside the HSIW, which can be calculated from $a_2 = W_{HSIW}$–$2a_1$. The k_{x1} and k_{x2} are the x-direction wavenumber inside the HSIW in the dielectric and air, respectively.

The calculated effective relative permittivity, $\epsilon_{r,eff}$, and normalized effective loss factor, $tan\delta_n$, of the 3D-printed HSIW are plotted in Fig. 3.3, which shows that $\epsilon_{r,eff}$ varies from 1.00309 to 1.00337 and $tan\delta_n$ varies from $5.64 \times 10^{-3} to 6.80 \times 10^{-3}$ for the whole single-mode operating band. The trend is for $\epsilon_{r,eff}$ and $tan\delta_n$ to increase with frequency towards the end of the single propagation mode at f /fc = 2. The plots in Fig. 3.3 indicate that the values of $\epsilon_{r,eff}$ and the $tan\delta_n$ are close to an air-filled structure.

The effective dielectric constant, $\epsilon_{r,eff}$, is nearly equal to one and the normalized effective loss factor,$tan\delta_n$, gives a negligible angle value.

3.3.3 Design Comparison

As illustrated in Fig. 3.4(a)-(c), a comprehensive design study investigating the figure of merit of different planar transmission lines was conducted and supported by EM simulations comparing conventional structures, e.g. microstrip and CPW, with

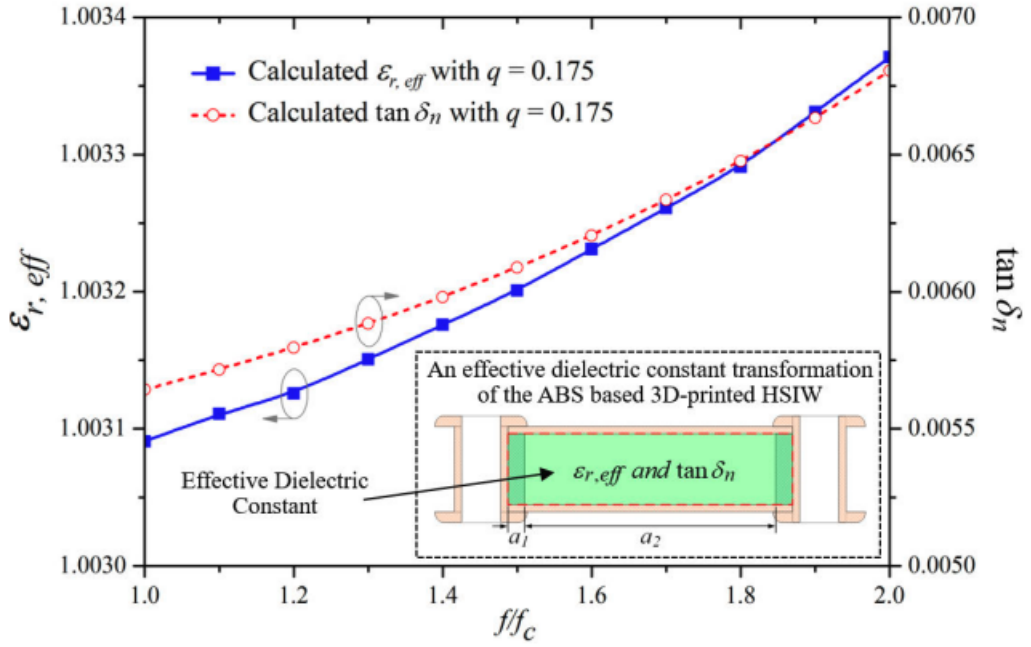

Figure 3.3: Calculated effective relative permittivity, $\epsilon_{r,eff}$, of the loaded RWG with two dielectric materials, which are air and ABS with the dielectric constant of 2.75, following Eqn. (5) and the normalized effective loss factor, $tan\delta_n$, following Eqn. (6)

the 3D printed HSIW. Commonly used substrate materials for microstrip lines and CPWs, such as Roger RT5880 and high resistivity silicon (with resistivity more than $4k\omega - cm$), were chosen and compared to ABS for their propagation characteristics. The material properties used in all transmission line simulations are presented in Table 3.2. The AWR TX-LINE is used to preliminary calculate the dimensions of microstrip and CPW structures before conducting the 3D full-wave simulations [47]. The multiline calculation technique is employed to extract the attenuation and phase constants through the simulated S-parameters. Therefore, at least two different lengths of each transmission line are required and simulated [48], [49]. Figure 3.4(d)

Table 3.2: List of Material Properties Used in Transmission Line Simulations

Material	Dielectric constant	Loss tangent (tan δ)
ABS	2.75	0.025
Roger RT5880	2.2	0.0009
High resistivity silicon	11.9	0.001

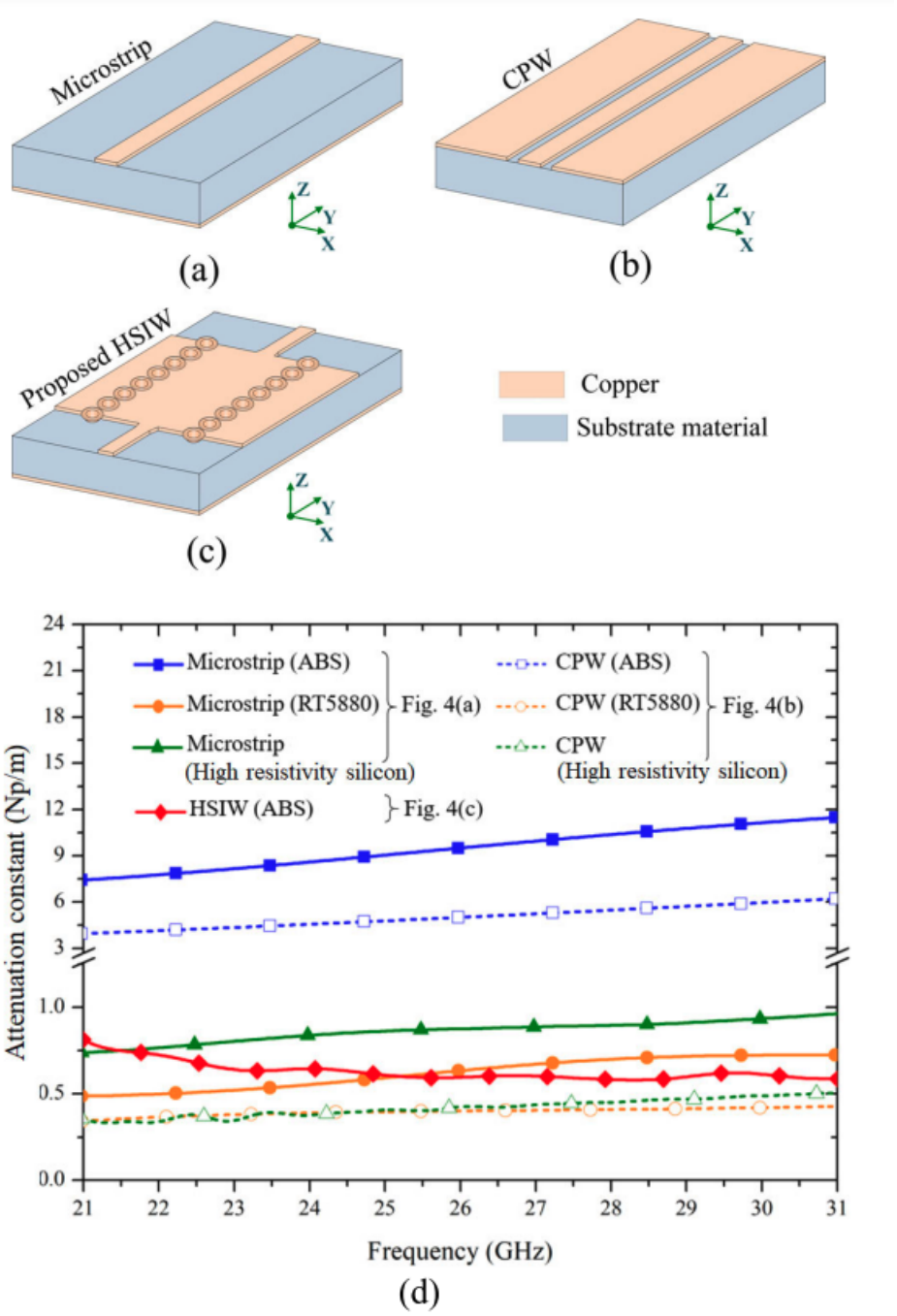

Figure 3.4: 3D views of the transmission line geometries used to compare their figure of merit in this work: (a) conventional microstrip line, (b) standard coplanar waveguide, (c) 3D-printed HSIW, and (d) the extracted attenuation constant of the all aforementioned transmission lines with different substrate materials (simulated).

shows the simulated attenuation constant of the 3D-printed HSIW compared with the conventional planar transmission lines, both microstrips and CPWs. Microstrip transmission lines, simulated with substrate materials of standard ABS, RT5880, and HRS achieve average attenuation constants of 9.480 Np/m (82.29 dB/m), 0.622 Np/m (5.39 dB/m), and 0.863 Np/m (7.49 dB/m), respectively, in the frequency range from 21 GHz to 31 GHz. The CPW designs with the same substrate materials have attenuation constants of 5.037 Np/m (43.72 dB/m), 0.397 Np/m (3.45 dB/m), and 0.418 Np/m (3.63 dB/m) using ABS, RT5880, and HRS, respectively. Although the microstrip and CPW transmission line designs using ABS substrates have higher signal attenuations as compared to the designs using RT5880 and HRS, the ABS substrate does not show any significant increase in attenuation constant for the HSIW case.

From Fig. 3.4(d), all microstrip transmission lines and CPWs clearly suffer from both radiation and material losses when the frequency increases, while this is not the case for the 3D-printed HSIWs. Moreover, even though some microstrip and CPW designs using RT5880 and HRS substrates exhibit slightly lower attenuation constant compared to the ABS-based HSIW, these substrate materials are normally at least 100x more expensive compared to ABS.

3.3.4 HSIW Fabrication and Assembly

Figure 3.5(a) shows the fabricated HSIW component parts for the length of 46.8-mm. There is a laser-patterned top and bottom copper sheet and the 3D printed waveguide substrate formed of ABS. Figure 3.5(b)-3.5(d) show the manufactured and assembled HSIW prototypes of three different HSIW designs with lengths of 46.8 mm, 52.0 mm, and 91.0 mm, respectively. First, the top and bottom copper sheets are made of a 99.90.15 mm [50]. The sheets were cut into the desired shapes by using the water laser cutting technology (Laser-MicroJet Cutter) to form the microstrip feeds and matching transitions as well as circular etched-hole arrays [51]. For the 3D printed substrate, Stratasys Object1000 3D printer is used to fabricate the substrate of the HSIW with ABS material [52]. The whole fabrication process is considered a very cost-effective precision manufacturing compared to other fabrication methods as summarized in [53]. The ABS-based HSIW structure was assembled by using commercial ready-to-use through-copper via transitions to firmly attach all fabricated copper and ABS layers together, avoiding the utilization of the complicated and costly conventional via and through-substrate fabrication process, e.g. through-substrate etching, electroplating for through via metallization and wet etching using various chemicals. The ABS-based HSIW structure is mechanically attached and fixed between the top and bottom copper sheets by using

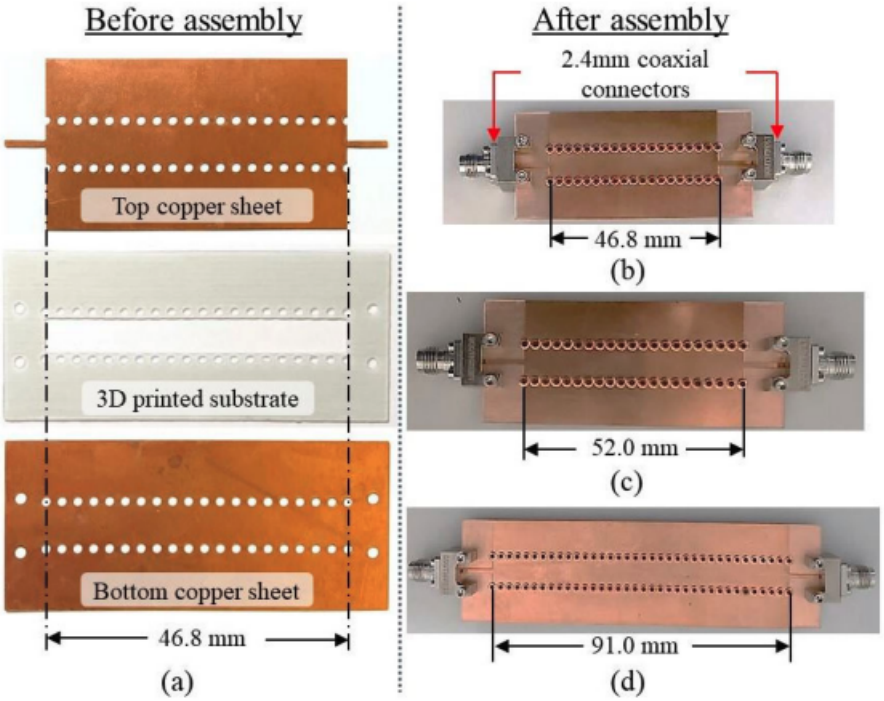

Figure 3.5: Fabricated HSIW prototype before and after assembly. (a) The 3D-printed HSIW is composed of the top and bottom laser-patterned copper sheets containing microstrip feed transitions and HSIW etch-hole array, and 3D printed ABS substrate with the total length of 46.8 mm. The right hand pictures show the fabricated HSIW after assembly with three different lengths of (b) 46.8 mm, (c) 52.0 mm, and (d) 91.0 mm, mounted with relaunchable 2.4-mm coaxial connectors at the end of microstrip feed lines

commercial ready-to-use through-copper via transitions. The commercial prefabricated through-copper via array is mechanically compressed by using the mechanical PCB through-hole-plating press tool [45], firmly fixing all the SIW parts together. Moreover, four screws are used to further fixing the SIW parts, shown in Fig. 3.5(b). These screw holes are also used as the connector alignment hole to accurately align each part of the SIW together. The final assembled 3D printed HSIW prototypes are shown in Fig. 3.5(b)-3.5(d) with the length of 46.8 mm, 52.0 mm, and 91.0 mm, respectively.

3.3.5 Measurement Results

All three HSIW prototypes were attached with relaunchable SOUTHWEST 2.4-mm coaxial connectors mounted on both sides of the microstrip feed lines. The S-parameters were measured using Agilent E8361A PNA Microwave Network Analyzer with two-port Short-Open-Load-Through (SOLT) calibration, bringing the S-parameter reference plane to the ends of the coaxial cables used for further coax-

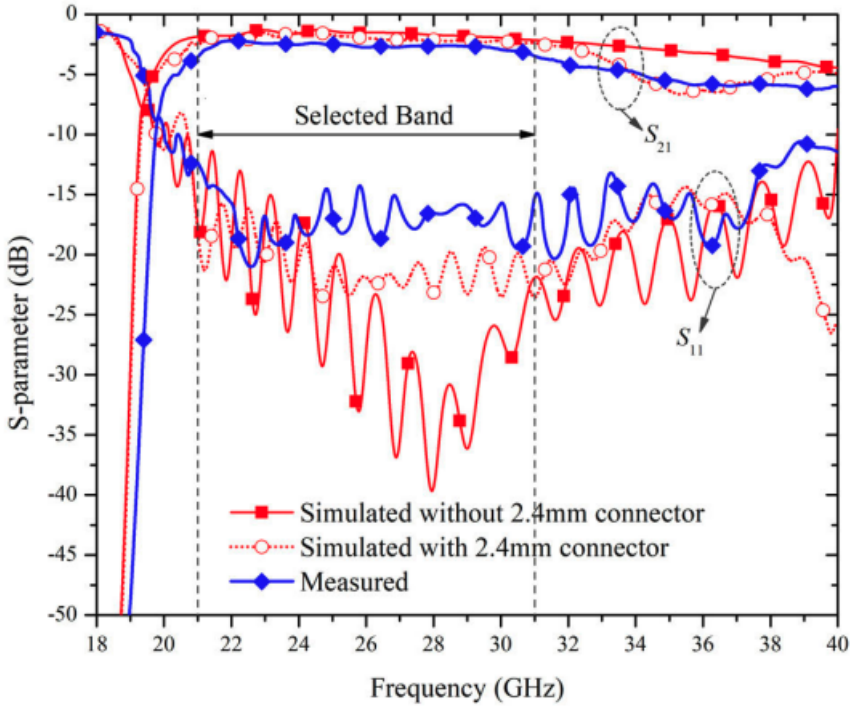

Figure 3.6: Simulated and measured S -parameters of the 91.0 mm-long 3D-printed HSIW over the operational band of 21-31 GHz. The plot also shows the effect of the 2.4mm coaxial connectors on the S-parameters(simulated).

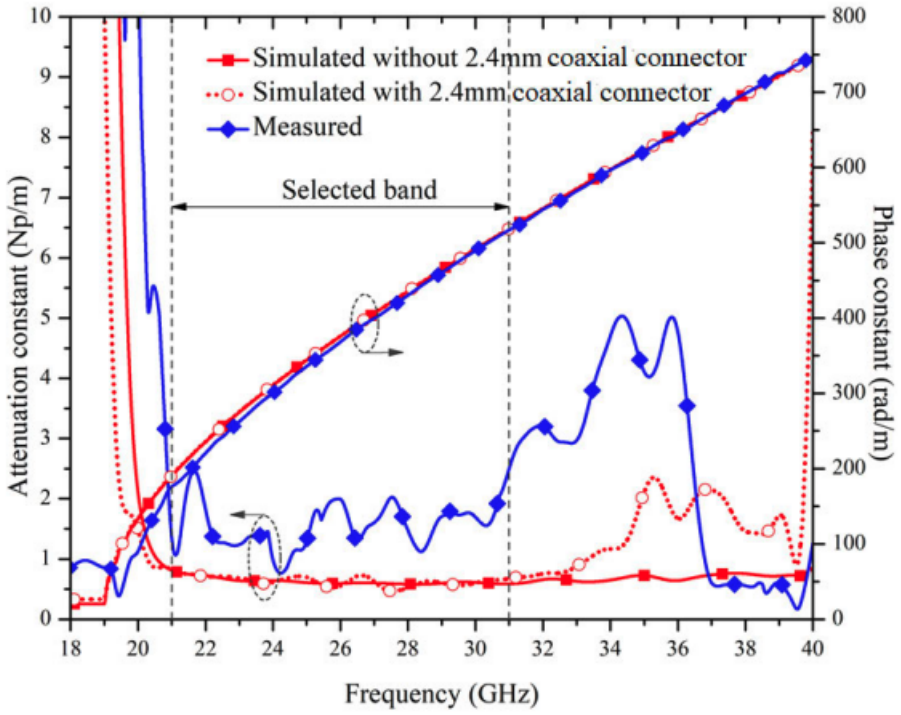

Figure 3.7: Extracted propagation characteristics of the 3D printed HSIW comparing phase and attenuation constants calculated from the measured and simulated S-parameters over the nominal frequency band from 21-31 GHz.

ial connector terminations. The frequency range was set to 15 GHz – 40 GHz on the PNA with 3201 frequency points. Figure 3.6 compares the measured and simulated reflection, S11, and transmission coefficients, S21, of the fabricated HSIW prototype with the length of 91.0 mm. The measured reflection coefficient, S11, of the 3D-printed HSIW was lower than -10 dB over the operational band of $21-31$ GHz while the S21 is better than -3.56 dB for the entire selected band. Fig. 3.6 also shows the effect of the 2.4mm coaxial connectors on the S-parameters of the 3D printed HSIW. However, since the multiline technique is used to calculate the transmission line loss, the effect of the coaxial connectors is removed after the mathematical calculations. By using the multiline calculation technique [48], [49], the phase and attenuation constants of the 3D-printed HSIWs can be extracted from the measured and simulated S-parameters as shown in Fig. 3.7. Over the whole operational band from 21 – 31 GHz, the average attenuation constant extracted from the simulated results without and with 2.4-mm coaxial connectors are 0.629 Np/m and 0.636 Np/m, respectively, while the measured attenuation constant has an average value of 1.56 Np/m. The main reasons for the propagation loss difference come from the fact that the dielectric and metal materials used in the designs are more lossy.

Also, the electrical connections between the patterned copper sheets and prefabricated through-substrate copper vias are not perfect. Specifically, during the assembly process, the ready-to-use through-copper vias were placed one-by-one into the etch-hole arrays of the copper sheets and, subsequently, attached to the HSIW structure. Then, commercial prefabricated copper vias were pressed with the mechanical PCB through-hole-plating press machine, which slightly affect the copper via shape due to the slightly high manually pressing force. Fortunately, this fabrication process can be further optimized and automated in the future. Even with some minor fabrication and assembly issues, the 3D-printed HSIWs can achieve the average signal propagation loss of 1.56 Np/m, which is among the lowest attenuation loss published to date. In Fig. 3.7, the extracted phase constant of the measured S-parameter results is also plotted and compared to the one calculated from the simulations with and without the 2.4-mm coaxial connectors.

Table 3.3 presents the key parameter comparisons between the 3D-printed HSIW with other state-of-the-art SIW designs with a similar frequency range recently reported [24], [26], [28], [29]. The substrate material used in this work is standard ABS, which is inexpensive when compared with the other commercially-available microwave substrate materials in [24], [26], [28], [29], e.g., Roger 5880, Roger 6002 and LTCC. In [24], [28], [29], the fabrication process uses a CNC/Laser micro-milling machine to manufacture the devices, which are comparatively expensive compared with 3D printing technology. Moreover, most of SIW fabrications rely critically on

Table 3.3: Key Parameters Comparison of Measurement Results of This Work With Other Published Work

Key parameters	[24]	[26]	[28]	[29]	***This work***
Structure	Air-filled SIW[1] (AFSIW)	Hollow SIW (HSIW)	Dielectric-filled SIW (DFSIW)	Half-mode SIW (HMSIW)	***Hollow SIW (HSIW)***
Operating frequency	26.5 – 40 GHz	26.5 – 40 GHz	20 – 40 GHz	26.5 – 40 GHz	***21 – 31 GHz***
Fractional bandwidth	40.60 %	40.60 %	66.67 %	40.60 %	***38.46 %***
Substrate material	Roger 6002	LTCC[2]	Roger 5880	Roger 6002	***ABS (3D printed)***
Fabrication process	PCB + Laser micromachining lapping and polishing sputtering	Progressive-lamination LTCC	PCB + Laser micromachining or mechanical CNC[3] micromilling	Mechanical CNC[3] micromilling	***3D printing technology + laser-microjet cutter***
Via hole fabrication	Electroplating	Conductive paste with Progressive-lamination	Electroplating	Electroplating	***Commercial prefabricated through copper vias***
Fabrication complexity	Moderate	Difficult	Simple	Moderate	***Simple***
Transition	CBCPW[4] to SIW and SIW to AFSIW	RWG to HSIW	ML[5] to DFSIW	ML to HMSIW	***ML to HSIW***
Propagation constant	0.51 Np/m	2 Np/m	2.5 Np/m	1.75 Np/m	***1.56 Np/m***
Fabrication cost	Medium	High	Medium	Medium	***Low***
Substrate and material costs	High	High	High	High	***Low***

[1]SIW: substrate integrated waveguide; [2]LTCC: low temperature co-fired ceramic; [3]CNC: computerized numerical control; [4]CBCPW: conductor-backed coplanar waveguide; [5]ML: microstrip line.

the fabrication of the through-substrate vias and via metallization, which are normally very complicated and costly, especially at high frequencies. The new idea in combining 3D printing technology and using commercial prefabricated through-substrate vias eliminates the aforementioned issues, e.g. fabrication complexity and overall development costs, and, thus, opens a new opportunity in developments of very low cost and less complex high frequency integrated components and devices for many applications such as 5G, IoT and high speed robotic communications.

3.4 Potential Applications

As presented in this article, the performance of the HSIW using 3D printing technology to fabricate the hollow substrate channels is excellent. It has advantages of stability, broadband design, low-cost, low-profile design, lightweight, and the possibility for mechanical flexibility. It offers a new degree of design freedom for applications benefitting from the use of conformal and flexible structures, which are now very easy to fabricate compared with the conventional rectangular waveguide structure.

Thus, the 3D-printed HSIW can be used in flexible conformal structures, such as in robotic communication systems where multiple transceiver RF chains are required

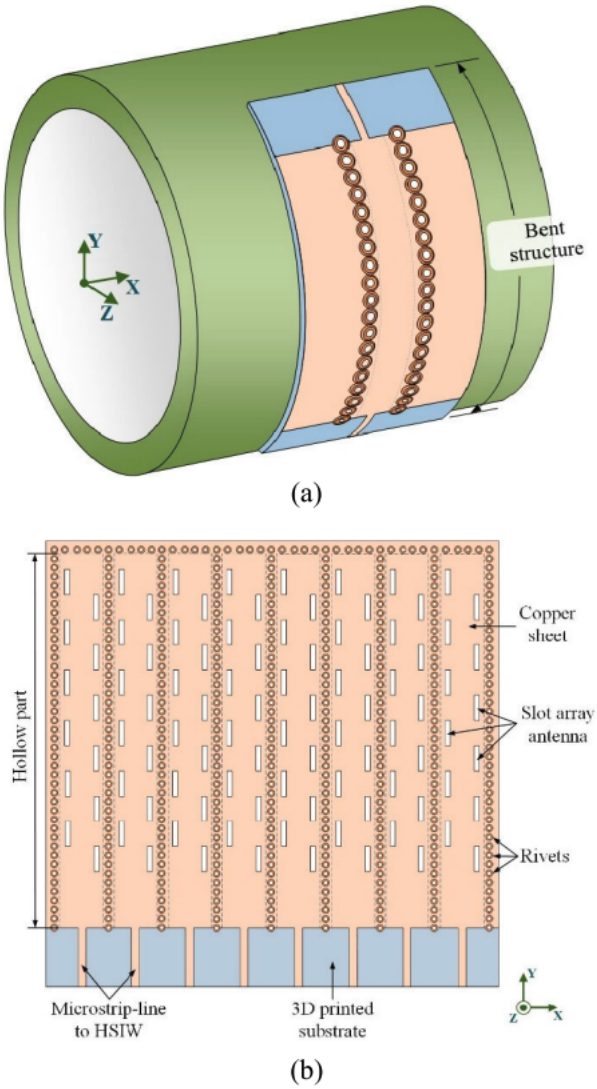

Figure 3.8: Conceptual design of HSIW potential applications: (a) HSIW conformal structure used as a communication medium on the arm of a robot and (b) MIMO HSIW slotted array antenna using in the 5G/6G communication systems

and the antennas are to be integrated into the mechanical body. Conceptual designs of potential applications have been produced in Figure 3.8. An example application is shown in Figure 3.8(a), illustrating a flexible HSIW structure that could be used as a communication device on the arm of a robot. This HSIW can be potentially designed with a flexible substrate, instead of the rigid ABS material used for this work and therefore it can be bent at an angle and wrapped around a conformal structure e.g. a cylindrical shape.

Moreover, since 5G communication networks utilize MIMO technology, this HSIW technology can be used to implement antenna arrays. As illustrated in Figure 3.8(b), the HSIW could be potentially used to realise a slot antenna array in a MIMO configuration. The MIMO slot antenna array provides enhanced gain and narrow

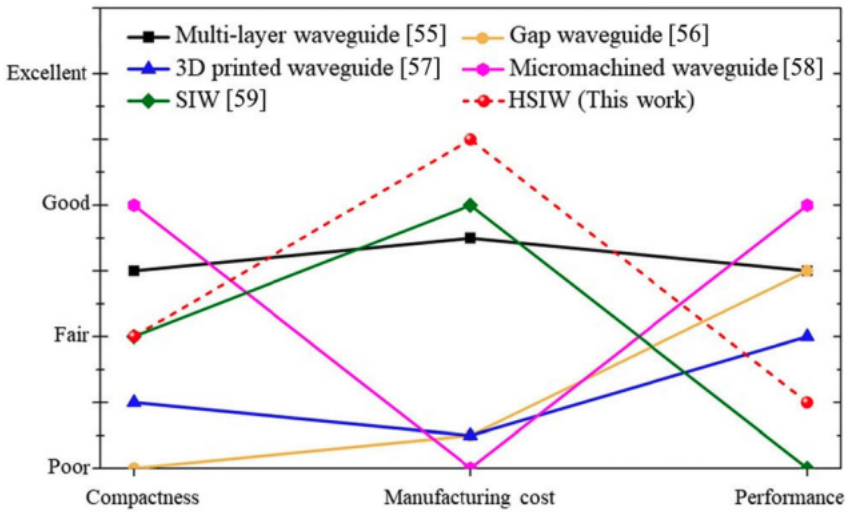

Figure 3.9: A comparison of emerging waveguide technologies in terms of compactness, manufacturing cost, and RF performance as presented in [54].

beam width, giving new design flexibility and compatibility with integrated circuits and other planar PCB circuits in millimetre wave applications.

3.5 Summary

This article has described a novel methodology for the fabrication of millimetre-wave HSIW structures based on 3D printing of the substrate, combined with laser cutting of the conductors and pre-formed via-hole plugs. The measured attenuation constant of the 3D-printed HSIW is less than 1.56 Np/m over the operating frequency range of 21-31 GHz, and a fractional bandwidth of 38.46% is achieved. The 3D-printed HSIW is compact, low cost, broadband, low loss, and easy to fabricate and integrate with other planar circuits. The measured results of the 3D-printed HSIW show that the device can be applied to be used for 5G communication with easy integration of other RF passive and active components such as filter, combiner/splitter, and antenna. Figure 3.9 presented a comparison of key novel waveguide technologies along with our proposed HSIW, in terms of three key factors; compactness, manufacturing cost, and performance [54]. There are five emerging waveguide (WG) technologies presented in the graph; the multi-layer waveguide [55], gap waveguide [56], 3D printed waveguide [57], micromachined waveguide [58], and SIW [59] compared with the 3D-printed HSIW. The 3D-printed HSIW in this work has a compactness similar to the SIW techniques and a better performance and lower manufacturing cost than the SIW. Although the 3D-printed HSIW has a slightly worse performance compared with the 3D printed waveguide technique, overall the 3D-printed HSIW has low manufacturing cost compared to the other technologies.

This work has proved the concept, but further work is required to further optimize the fabrication process. The authors will seek to optimize and develop the fabrication steps, such as reducing the thickness of copper sheet [60], using automatic via fabrication [61] and reducing the loss from the 3D-printed substrate [62], [63] in future work.

3.6 References

[1] D. M. Pozar, Microwave Engineering, 4th ed. Hoboken, NJ: Wiley, 2012.

[2] I. D. Robertson, N. Somjit, and M. Chongcheawchamnan, Microwave and Millimetre-Wave Design for Wireless Communication. Hoboken, NJ, USA: Wiley, 2016.

[3] T. Kai, "A coaxial line to post-wall waveguide transition for a cost-effective transformer between a RF-device and a planar slot-array antenna in 60- GHz band," IEICE Trans. Commun., vols. E89–B, no. 5, pp. 1646–1653, May 2006.

[4] J. Coonrod and B. Rautio, "Comparing microstrip and CPW performance," Microw. J., vol. 55, no. 7, pp. 74–86, Jul. 2012.

[5] E. C. Niehenke, R. A. Pucel, and I. J. Bahl, "Microwave and millimeterwave integrated circuits," IEEE Trans. Microw. Theory Techn., vol. 50, no. 3, pp. 846–857, Mar. 2002.

[6] W. Deal, "Coplanar waveguide basics for MMIC and PCB design," IEEE Microw. Mag., vol. 9, no. 4, pp. 120–133, Aug. 2008.

[7] M. Abulghasim, J. Tabatchnick, and M. Markovic, "Comparison of embedded coplanar waveguide and strip line for multi-layer boards," Semantic Scholar, Seattle, WA, USA, Tech. Rep., 2019. Accessed: Jan. 30, 2020. [Online]. Available: https://www.semanticscholar.org/paper/ Comparison-of-Embedded-Coplanar-Waveguide-and-for-AbulghasimTabatchnick/82e09d51ca4d0ca992f9f5cc 6a5c3854b7fc4ab9

[8] Y. CPW Yun, H. S. Kim, and N. Jang, "Study on characteristics of various RF transmission line structure on PES substrates for application to flexible MMIC," ETRI J., vol. 36, no. 1, pp. 1646–1653, Feb. 2014.

[9] D. Deslandes and K. Wu, "Integrated microstrip and rectangular waveguide in planar form," IEEE Microw. Wireless Compon. Lett., vol. 11, no. 2, pp. 68–70, Feb. 2001.

[10] M. Bozzi, A. Georgiadis, and K. Wu, "Review of substrateintegratedwaveguide

circuits and antennas," IET Microw., Antennas Propag., vol. 5, no. 8, pp. 909–920, 2011.

[11] H. Kumar, "A Review on Substrate Integrated Waveguide and its Microstrip Interconnect," IOSR J. Electron. Commun. Eng., vol. 3, no. 5, pp. 36–40, 2012.

[12] K. Wu, D. Desiandes, and Y. Cassivi, "The substrate integrated circuits-a new concept for high-frequency electronics and optoelectronics," in Proc. 6th Int. Conf. Telecommun. Modern Satell., Cable Broadcast. Service, Nis, Yugoslavia, 2003, p. 3.

[13] X.-P. Chen and K. Wu, "Low-loss ultra-wideband transition between conductor-backed coplanar waveguide and substrate integrated waveguide," in IEEE MTT-S Int. Microw. Symp. Dig., Boston, MA, USA, Jun. 2009, pp. 349–352.

[14] L. Jin, R. M. Lee, and I. D. Robertson, "Analysis and design of a slotted waveguide antenna array using hollow substrate integrated waveguide," in Proc. Eur. Microw. Conf. (EuMC), Paris, France, Sep. 2015, pp. 1423–1426.

[15] M. Bozzi, M. Pasian, and L. Perregrini, "Modeling of losses in substrate integrated waveguide components," in Proc. Int. Conf. Numer. Electromagn. Model. Optim. for RF, Microw., Terahertz Appl. (NEMO), Pavia, Italy, May 2014, pp. 1–4.

[16] M. Bozzi, C. Tomassoni, L. Perregrini, R. Bahr, and M. Tentzeris, "Additive manufacturing of substrate integrated waveguide components," in IEEE MTT-S Int. Microw. Symp. Dig., Chengdu, China, Jul. 2016, pp. 1–4.

[17] D. Deslandes and K. Wu, "Accurate modeling, wave mechanisms, and design considerations of a substrate integrated waveguide," IEEE Trans. Microw. Theory Techn., vol. 54, no. 6, pp. 2516–2526, Jun. 2006.

[18] E. Diaz-Caballero, A. Belenguer, H. Esteban, V. E. Boria, C. Bachiller, and J. V. Morro, "Analysis and design of passive microwave components in substrate integrated waveguide technology," in IEEE MTT-S Int. Microw. Symp. Dig., Ottawa, ON, Canada, Aug. 2015, pp. 1–3.

[19] Y. Li, L.-A. Yang, L. Du, K. Zhang, and Y. Hao, "Design of millimeterwave resonant cavity and filter using 3-D substrate-integrated circular waveguide," IEEE Microw. Wireless Compon. Lett., vol. 27, no. 8, pp. 706–708, Aug. 2017.

[20] H. Yousef, S. Cheng, and H. Kratz, "Substrate integrated waveguides (SIWs) in a flexible printed circuit board for millimeter-wave applications," J. Microelectromech. Syst., vol. 18, no. 1, pp. 154–162, Feb. 2009.

[21] N. Ranjkesh and M. Shahabadi, "Reduction of dielectric losses in substrate integrated waveguide," Electron. Lett., vol. 42, no. 21, pp. 1230–1231, Oct. 2006.

[22] F. Bigelli, D. Mencarelli, M. Farina, G. Venanzoni, P. Scalmati, and C. Renghini, "Design and fabrication of a dielectric substrate-integrated waveguide," IEEE Trans. Compon., Packag., Manuf. Technol., vol. 6, no. 2, pp. 256–261, Feb. 2016.

[23] F. Parment, A. Ghiotto, T.-P. Vuong, J.-M. Duchamp, and K. Wu, "Air-filled SIW transmission line and phase shifter for high-performance and low-cost U-Band integrated circuits and systems," in Proc. Global Symp. Millimeter-Waves (GSMM), Montreal, QC, Canada, May 2015, pp. 1–3.

[24] F. Parment, A. Ghiotto, T.-P. Vuong, J.-M. Duchamp, and K. Wu, "Airfilled substrate integrated waveguide for low-loss and high power-handling millimeter-wave substrate integrated circuits," IEEE Trans. Microw. Theory Techn., vol. 63, no. 4, pp. 1228–1238, Apr. 2015.

[25] L. Jin, R. M. A. Lee, and I. Robertson, "Analysis and design of a novel lowloss hollow substrate integrated waveguide," IEEE Trans. Microw. Theory Techn., vol. 62, no. 8, pp. 1616–1624, Aug. 2014.

[26] L. Jin, "Waveguide-based antenna arrays in multi-chip module technology," Ph.D. dissertation, School Electron. Elect. Eng., Univ. Leeds, Leeds, U.K., 2014.

[27] A. Belenguer, H. Esteban, and V. E. Boria, "Novel empty substrate integrated waveguide for high-performance microwave integrated circuits," IEEE Trans. Microw. Theory Techn., vol. 62, no. 4, pp. 832–839, Apr. 2014.

[28] X.-C. Zhu, W. Hong, K. Wu, K.-D. Wang, L.-S. Li, Z.-C. Hao, H.-J. Tang, and J.-X. Chen, "Accurate characterization of attenuation constants of substrate integrated waveguide using resonator method," IEEE Microw. Wireless Compon. Lett., vol. 23, no. 12, pp. 677–679, Dec. 2013.

[29] I. S. S. Lima, F. Parment, A. Ghiotto, T.-P. Vuong, and K. Wu, "Broadband Dielectric-to-Half-Mode air-filled substrate integrated waveguide transition," IEEE Microw. Wireless Compon. Lett., vol. 26, no. 6, pp. 383–385, Jun. 2016.

[30] Y. Dong, P. Liu, D. Yu, B. Yi, and G. Li, "Active substrate integrated terahertz waveguide using periodic graphene stack," AIP Adv., vol. 5, no. 11, Nov. 2015, Art. no. 117237.

[31] K. Wu, Y. Jian Cheng, T. Djerafi, and W. Hong, "Substrate-integrated millimeter-wave and terahertz antenna technology," Proc. IEEE, vol. 100, no. 7, pp. 2219–2232, Jul. 2012.

[32] B. Hong, N. Feng, J. Chen, G. Wang, V. Doychinov, R. Clarke, J. Cunningham, I. Robertson, and N. Somjit, "Substrate integrated Bragg waveguide: An octave-bandwidth single-mode hybrid transmission line for millimeterwave applications," Opt. Exp., vol. 28, pp. 27903–27918 (2020).

[33] C. Guo, X. Shang, J. Li, M. J. Lancaster, and J. Xu, "3-D printed lightweight microwave waveguide devices," in Proc. IEEE 5th Asia– Pacific Conf. Antennas Propag. (APCAP), Kaohsiung, Taiwan, Jul. 2016, pp. 47–48.

[34] B. T. Malik, V. Doychinov, S. A. R. Zaidi, I. D. Robertson, and N. Somjit, "Antenna gain enhancement by using low-infill 3D-printed dielectric lens antennas," IEEE Access, vol. 7, pp. 102467–102476, 2019.

[35] N. Chudpooti, S. Praesomboon, N. Duangrit, N. Somjit, and P. Akkaraekthalin, "An X-band portable 3D-printed lens antenna with integrated waveguide feed for microwave imaging," in Proc. Photon. Electromagn. Res. Symp. (PIERS-Spring), Rome, Italy, Jun. 2019, pp. 487–492.

[36] N. Chudpooti, N. Duangrit, P. Akkaraekthalin, I. D. Robertson, and N. Somjit, "220-320 GHz hemispherical lens antennas using digital light processed photopolymers," IEEE Access, vol. 7, pp. 12283–12290, 2019.

[37] N. Chudpooti, N. Duangrit, P. Akkaraekthalin, I. D. Robertson, and N. Somjit, "Electronics-based free-space terahertz measurement using hemispherical lens antennas," IEEE Access, vol. 7, pp. 95536–95546, 2019.

[38] B. T. Malik, V. Doychinov, S. A. R. Zaidi, I. D. Robertson, N. Somjit, R. Richardson, and N. Chudpooti, "Flexible rectennas for wireless power transfer to wearable sensors at 24 GHz," in Proc. Res., Invention, Innov. Congr. (RI2C), Bangkok, Thailand, Dec. 2019, pp. 1–5, doi: 10.1109/RI2C48728.2019.8999964.

[39] N. Duangrit, B. Hong, A. D. Burnett, P. Akkaraekthalin, I. D. Robertson, and N. Somjit, "Terahertz dielectric property characterization of photopolymers for additive manufacturing," IEEE Access, vol. 7, pp. 12339–12347, 2019.

[40] G. L. Goh, S. Agarwala, G. D. Goh, H. K. J. Tan, L. Zhao, T. K. Chuah, and W. Y. Yeong, "Additively manufactured multi-material free-form structure with printed electronics," Int. J. Adv. Manuf. Technol., vol. 94, nos. 1–4, pp. 1309–1316, Jan. 2018.

[41] D. Deslandes, "Design equations for tapered microstrip-to-Substrate integrated waveguide transitions," in IEEE MTT-S Int. Microw. Symp. Dig., Anaheim, CA, USA, May 2010, pp. 704–707.

[42] C.-K. Lee, J. McGhee, C. Tsipogiannis, S. Zhang, D. Cadman, A. Goulas, T.

Whittaker, R. Gheisari, D. Engstrom, J. Vardaxoglou, and W. Whittow, "Evaluation of microwave characterization methods for additively manufactured materials," Designs, vol. 3, no. 4, p. 47, Sep. 2019.

[43] J. Pourahmadazar and T. A. Denidni, "Author correction: Towards millimeter-wavelength: Transmission-mode fresnel-zone plate lens antennas using plastic material porosity control in homogeneous medium," Sci. Rep., vol. 8, no. 1, Dec. 2018, Art. no. 5300.

[44] H. Xin and M. Liang, "3-D-printed microwave and THz devices using polymer jetting techniques," Proc. IEEE, vol. 105, no. 4, pp. 737–755, Apr. 2017.

[45] FORTEX. PTH400 Mechanical Through Hole Press. Accessed: Mar. 30, 2020. [Online]. Available: http://www.fortex.co.uk/download/ pth400-mechanical-through-hole-press/

[46] CST-MW Studio, Comput. Simul. Technol., Framingham, MA, USA, 2017.

[47] Cadence Design Systems. Transmission-line calculator (TX-Line Software). Accessed: Feb. 10, 2020. [Online]. Available:
https://www.awr. com/awr-software/options/tx-line

[48] M. D. Janezic and J. A. Jargon, "Complex permittivity determination from propagation constant measurements," IEEE Microw. Guided Wave Lett., vol. 9, no. 2, pp. 76–78, Feb. 1999.

[49] F. Xu and K. Wu, "Guided-wave and leakage characteristics of substrate integrated waveguide," IEEE Trans. Microw. Theory Techn., vol. 53, no. 1, pp. 66–73, Jan. 2005.

[50] Goodfellow. Supplier for Materials. Accessed: Apr. 2, 2020. [Online]. Available: http://www.goodfellow.com/

[51] Synova. MCS 300 Laser-MicroJet Cutter. Accessed: Jul. 4, 2020. [Online]. Available: www.synova.ch/machines/mcs-series/

[52] Stratasys Company. 3D Printing & Additive Manufacturing. Accessed: Jul. 10, 2020. [Online]. Available: https://www.stratasys.com

[53] A. Belenguer, H. Esteban, A. L. Borja, and V. E. Boria, "Empty SIW technologies: A major step toward realizing low-cost and low-loss microwave circuits," IEEE Microw. Mag., vol. 20, no. 3, pp. 24–45, Mar. 2019.

[54] Ericson. (May 2020). Making Waves: A New Method for mmWave Antennas and Components. [Online]. Available:

https://www.ericsson. com/en/blog/2020/5/new-method-for-millimeter-wave-antennas

[55] A. Vosoogh, H. Zirath, and Z. S. He, "Novel air-filled waveguide transmission line based on multilayer thin metal plates," IEEE Trans. THz Sci. Technol., vol. 9, no. 3, pp. 282–290, May 2019.

[56] E. Rajo-Iglesias, M. Ferrando-Rocher, and A. U. Zaman, "Gap waveguide technology for millimeter-wave antenna systems," IEEE Commun. Mag., vol. 56, no. 7, pp. 14–20, Jul. 2018.

[57] A. Tamayo-Dominguez, J.-M. Fernandez-Gonzalez, and M. Sierra-Perez, "Metal-coated 3D-printed waveguide devices for mm-Wave applications [Application Notes]," IEEE Microw. Mag., vol. 20, no. 9, pp. 18–31, Sep. 2019.

[58] A. Gomez-Torrent and J. Oberhammer, "Micromachined waveguide interposer for the characterization of multi-port sub-THz devices," J. Infr., Millim., THz Waves, vol. 41, no. 3, pp. 245–257, Mar. 2020.

[59] L. Sun, H.-W. Deng, Y.-F. Xue, J.-M. Zhu, and S.-B. Xing, "Compactbalanced BPF and filtering crossover with intrinsic common-mode suppression using single-layered SIW cavity," IEEE Microw. Wireless Compon. Lett., vol. 30, no. 2, pp. 144–147, Feb. 2020.

[60] I. E. Obuh, V. Doychinov, D. P. Steenson, P. Akkaraekthalin, I. D. Robertson, and N. Somjit, "Low-cost microfabrication for MEMS switches and varactors," IEEE Trans. Compon., Packag., Manuf. Technol., vol. 8, no. 9, pp. 1702–1710, Sep. 2018.

[61] S. J. Bleiker, A. C. Fischer, U. Shah, N. Somjit, T. Haraldsson, N. Roxhed, J. Oberhammer, G. Stemme, and F. Niklaus, "High-aspectratio through silicon vias for high-frequency application fabricated by magnetic assembly of gold-coated nickel wires," IEEE Trans. Compon., Packag., Manuf. Technol., vol. 5, no. 1, pp. 21–27, Jan. 2015, doi: 10.1109/TCPMT.2014.2369236.

[62] N. Somjit, G. Stemme, and J. Oberhammer, "Binary-coded 4.25-bit W-band Monocrystalline–Silicon MEMS multistage dielectricblock phase shifters," IEEE Trans. Microw. Theory Techn., vol. 57, no. 11, pp. 2834–2840, Nov. 2009, doi: 10.1109/TMTT.2009.2032350.

[63] P. Kadam, A. Odhekar, and A. A. Deshmukh, "Air suspended multiband E-Shaped microstrip antenna," in Proc. 4th Int. Conf. Comput. Commun. Control Autom. (ICCUBEA), Pune, India, Aug. 2018, pp. 1–6.

Chapter 4

22-32-GHz Curved Hollow SIWs for Advanced Millimeter-Wave Applications

Under review in IEEE ACCESS

GIORGOS SAVVIDES, NONCHANUTT CHUDPOOTI, JOACHIM OBERHAMMER, IAN D. ROBERTSON, and NUTAPONG SOMJIT

4.1 Abstract

Millimetre-wave communication, sensing, imaging, radar, and wireless power transfer systems are becoming far more widespread, largely due to advances made in integrated circuits and system-in-package technology. There is, as a result, a growing need for hardware that can be integrated into physical structures that are curved for a specific reason, such as pipelines, medical imaging systems, rotating machines, and the curved surfaces of aircraft, spacecraft, robots, and drones. This paper presents a novel design of a curved hollow substrate integrated waveguide (CHSIW) for these millimetre-wave applications. It is fabricated by using an optimum combination of additive and subtractive manufacturing technologies. Specifically, it utilizes the MultiJet printing (MJP) method to print an M3 crystal dielectric substrate, and a water laser cutter system to produce smooth copper sheets to be used as the top and bottom conductors of the CHSIW. The layers are fixed together using commercially available prefabricated through-hole vias, eliminating the cost and complexity of performing via fabrication and metallization steps used in other SIW designs. The proposed waveguide covers the range from 21.7 GHz to 32 GHz. To demonstrate the technique and evaluate the performance, two CHSIW samples were fabricated with

a different radius: specifically, the curved surfaces have radii of 166.8 mm and 125.1 mm, and they give measured average attenuation constant of 1.89 Np/m (16.42 dB/m) and 1.95 Np/m (16.94 dB/m), respectively.

4.2 Introduction

In recent years, millimetre-wave communication, sensing, imaging, radar, and wireless power transfer systems have attracted great interest [1], [2]. In communications, for example, this has been driven by the demand for higher data rates and 6G systems are expected to use frequencies beyond 100 GHz. More and more systems are becoming smart, and there has been a growing demand for millimetre-wave imaging and radar systems because high gain antennas and electronically steered arrays can be physically small. These new applications have led to a need for millimetre-wave components that can be designed and manufactured with low- cost and high performance. To achieve this requirement of low-cost devices, new fabrication methods need to be utilized. Furthermore, as transceivers become ever more important in the IoT paradigm, the requirement for new conformal structures that can be embedded into everyday objects has increased. For example, curved structures are needed for pipeline applications and for rotating machines [3]–[6]. 3D printing, or Additive Manufacturing (AM), is an increasingly popular method for fabricating arbitrary shaped components [7]–[9]and has significant advantages compared with the traditional molding and casting methods [10]. AM can fulfill the aforementioned requirements and can be utilized for the fabrication of microwave and terahertz devices [11], with almost arbitrary shape. 3D printing can produce high precision components and is currently being used in many areas of research and manufacturing [9], [12]. It can produce low-cost rapid prototypes and can mix materials together to develop custom-made components which may have specific dielectric properties and conformal shapes according to the design requirements [9]. Subtractive Manufacturing (SM) has been extensively used in the fabrication and development of RF and millimetre wave devices. SM is the process of etching or cutting material away to produce a desired component. It can be used on many kinds of materials, including ceramic, metals and alloys [13].There are many publication works that are utilizing either or both AM and SM, to produce RF and millimeter wave devices. [11]-[14]

The author in [15], presented a 3D printed rectangular waveguide based on FDM (fused deposition modeling) printing method with PLA (poly-lactic acid) printing material. The results demonstrated excellent RF performance, with an attenuation constant of 1.29 dB/m, while having a low weight and low cost. Among many types of microwave and millimetre-wave transmission lines [1], [2], [16], [17], the

substrate integrated waveguide (SIW) technology has attracted the most interest in recent years, since it has the advantages of rectangular waveguides, but it can be manufactured in the same process as microstrip lines [18]. Therefore, it is a great candidate to be used for future high frequency applications [18]–[40]. There is a wide range of SIW designs, based on various fabrication methodologies. State of the art designs include SIWs which are low in cost, provide ease of fabrication and assembly and a high performance [25], [33], [34], [38]. The author in [38], has designed a hollow SIW, by using commercially available prefabricated vias, water laser cutting and polyjet 3D printing method. That work reduced the overall cost and the complexity of the fabrication process as compared to LTCC, PCB and clean room methods. It resulted in a high performance SIW transmission line, with a measured attenuation constant of 1.56 Np/m for the frequency range of interest. Overall, this work has proved the concept of using additive and subtractive manufacturing to produce low-cost mm-wave devices. In addition to the need to design low-cost RF devices, presently there is a huge interest in fabricating techniques and materials which will allow the design of high-performance electronic devices that can be used on circular components or curved surfaces. For that reason, RF and mm-wave components also need to be designed as flexible or curved devices [40]–[43]. In [40], the authors designed an inkjet-printed flexible broadband SIW multilayer coupler on a polyimide film (Kapton) substrate. The authors demonstrated the feasibility of flexible 3D SIW systems utilizing inkjet printing technology. To further improve the SIW loss, the author proposed to use lower loss flexible substrates and reduce the conductor loss by increasing the substrate thickness. The author in [43], designed a flexible inkjet-printed mm-wave rectenna. The device is proven to provide adequate performance at the 24 GHz frequency of interest, with a return loss of more than 20 dB. The author demonstrated the ability to deliver power through flexible wireless mm-wave channels, offering applications in miniaturized wearable and smart skins for next generation fully printed flexible components for IoT applications. Based on the demanding RF performance and the need for using curved-shaped SIW devices, this paper presents a novel design of a low cost curved hollow substrate integrated waveguide (HSIW) device, that is based on a combination of subtractive and additive manufacturing techniques and can be suitable for a variety of telecommunication, defense, and space applications. The fabrication is simple and includes: 1) producing copper sheets as top and bottom enclosures of the waveguide by using a water-jet laser cutting machine, 2) 3D printing of the substrate using a material called Visijet M3, and 3) use of prefabricated copper vias and a mechanical through hole plating machine to attach all the layers together. The rest of the paper is structured as follows: in section 4.2.1 the paper examines possible 3D printed dielectric materials to be used as substrates for the curved HSIW. Their dielectric properties are char-

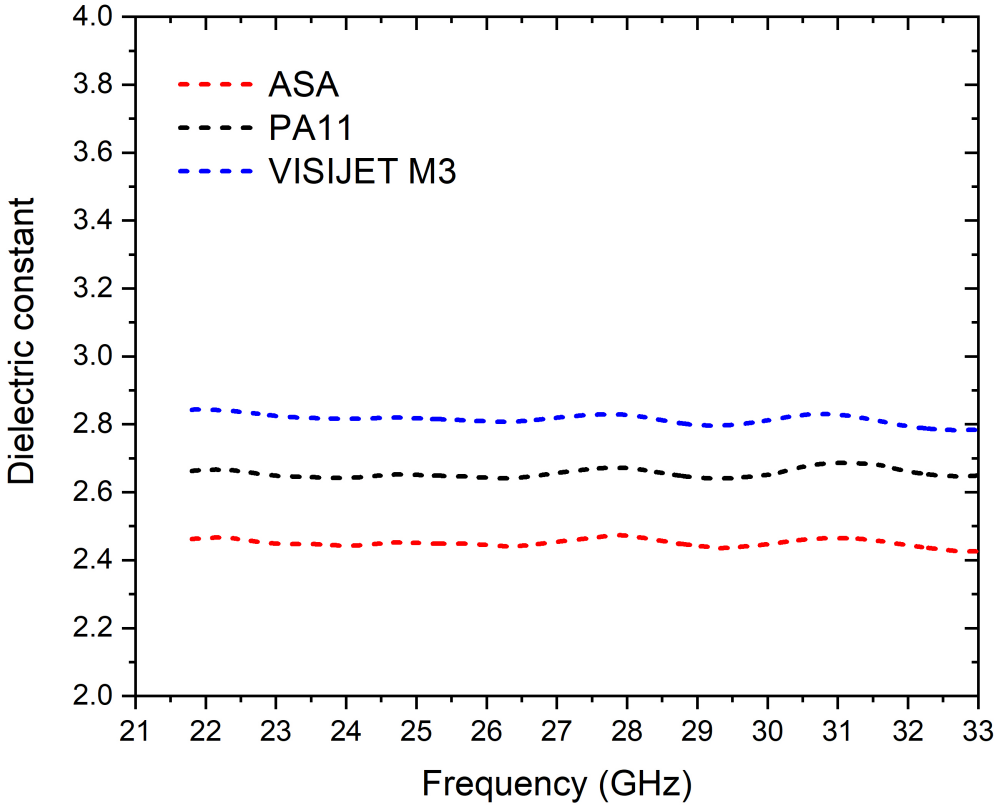

Figure 4.1: Dielectric constant versus frequency plot, using different additive manufacturing materials

acterized in the 21.7-33 GHz frequency range. In section 4.3, straight sections of HSIW that are based on candidate 3D printed materials are designed, fabricated and measured. Their performance indicates which material is more suitable to be used also as a substrate for the curved HSIW. The curved HSIW is presented in section 4.4, with simulations in CST Studio [44], fabrication and measurement results.

4.2.1 Dielectric Characterization

There is a wide variety of materials used for fabricating 3D printed millimetre-wave devices, as reported in the literature [43], [45]–[51].

We first characterized a promising selection of materials that could be used as the substrate for a curved section of a hollow SIW. The chosen three candidate 3D printing techniques were Selective Laser Sintering (SLS) [52], [53], Fused Deposition Modeling (FDM) [54] and Multijet Printing (MJP) [55]. The selection of 3D printing techniques was based on the criteria of availability, cost, and popularity. The materials that were chosen to be printed by these techniques were, respectively

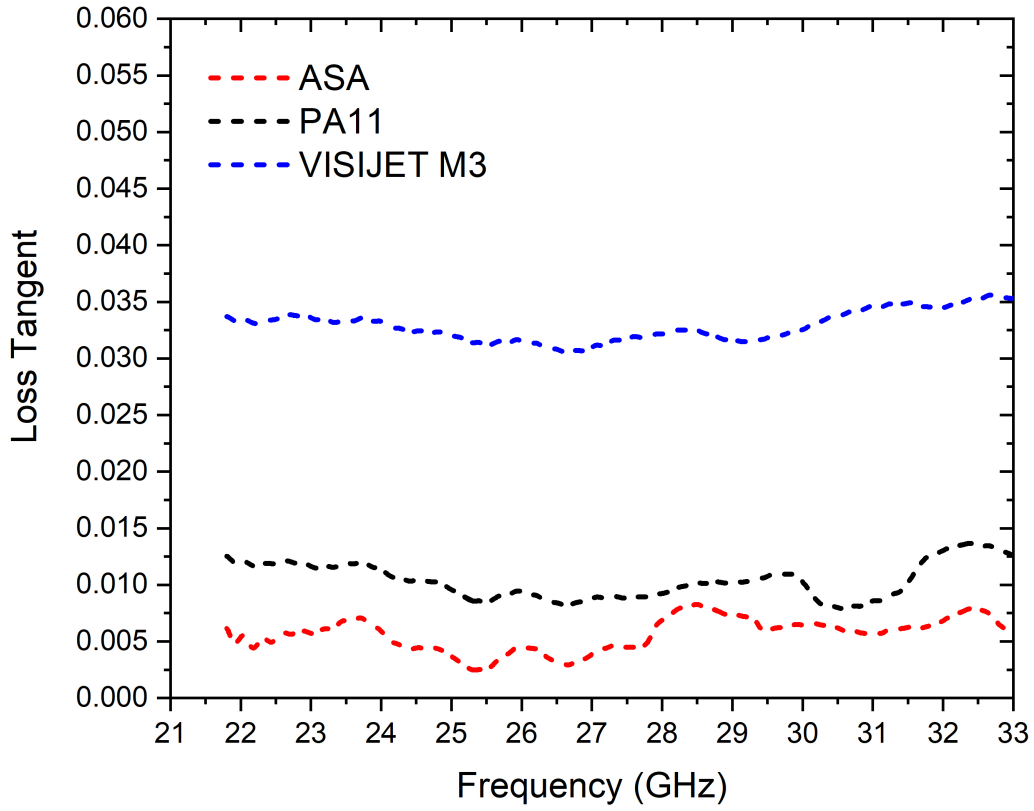

Figure 4.2: Loss tangent versus frequency plot, using different additive manufacturing materials

Polyamide Nylon black (PA11) [56], Acrylonitrile Styrene Acrylate Red (ASA) [57] and Visijet M3 crystal. The latter is a proprietary product of 3D SYSTEMS Inc. and is a durable and translucent material that can be used for many medical applications [58]. Since the frequency band of interest was selected to be from 21.7 GHz to 33 GHz, the materials' properties were characterized over this frequency range. The waveguide reflection resonance technique was used to measure these materials [59]–[65]. A pair of 2.4 mm cables connect the Agilent network analyzer model E8362B (PNA) to WR34 adaptors [66]. Between the adaptors there is a sample holder, which is a WR34 straight section [67], which holds the fabricated sample materials. Because low-cost manufacturing techniques were used to fabricate these samples, their manufacturing may have fabrication tolerances up to 2 percent. Therefore, the samples are lightly trimmed using high grit sandpaper to ensure a snug fit into the sample holder. The cuboid samples are then inserted to completely fill the cross section of the waveguide through line (sample holder). The samples have internal cross-section dimensions of width (8.636 mm) and height (4.318 mm). The sample length for each material is equal to the guided wavelength size that is calculated from the guided frequency, which is approximately the geometric mean between the recommended waveguide band-edge frequencies. Before performing the measurement, the PNA was calibrated using the TRL calibration method, with the reference plane brought at the edge of the waveguide adapters. The 85071E software [64], that comes pre-installed with the PNA E8362B, measures the s-parameters from the PNA and extracts the dielectric properties by using certain conversion algorithms. For this measurement, the Nicholson-Ross-Weir (NRW) conversion method was used to extract the relative permittivity and relative permeability of the sample material. The measured real part (dielectric constant) and imaginary part (loss tangent) of the dielectric permittivity, are shown in Figs. 4.1 and 4.2. The dielectric properties of the three materials are also summarized in Table 4.1.

4.3 Straight Section HSIW design

4.3.1 Theoretical Analysis and Design

In [38], the authors showed that the reported HSIW geometry gives an excellent performance and could be a great candidate for 5G and IoT applications. It can be seen that the measurement results provide a very low attenuation constant of 1.56 Np/m. In this paper, we use the same assembly technique as in [68], to produce a novel curved HSIW. As shown in Fig. 3.1(a), four components are used to construct the HSIW structure: (1) through-substrate copper via transitions that have been

Table 4.1: 3D printed materials average dielectric constants and average loss tangents for the frequency range of interest from 21.7 GHz to 33 GHz

Material	Average dielectric constant	Average loss tangent
ASA Red	2.45	0.005
PA11 Black	2.66	0.010
Visijet M3	2.82	0.033

commercially prefabricated; (2) a top copper sheet that has been laser-patterned and includes microstrip feeds and microstrip-to-SIW transitions; (3) the 3D printed substrate; (4) a bottom copper sheet that has been laser- patterned and includes circular via-holes and the microstrip ground plane. A 50-ohm microstrip line is being used as the interface between the HSIW structure and a 2.4 mm coaxial connector on the top copper sheet side. The ground planes for the microstrip transition are located on the copper sheet on the bottom side, and the via-holes are located on both copper sheets, ready for the mounting of the prefabricated copper vias. The cutoff frequency for a HSIW structure has been derived in [39] and is given as follows:

$$\lambda_c = 2a\,[0.999 + 4.946 * 10\hat{}(-4)\exp(9.409q)] \tag{4.1}$$

where q is the loading ratio given as:

$$q = \frac{2a_1\sqrt{\epsilon_r}}{a} \tag{4.2}$$

where a1 is the dielectric filling inside the hollow substrate. The propagation constant, γ, for a dielectric-filled SIW structure depends heavily on the dielectric substrate and specifically its loss tangent, $tan\delta$, as follows:

$$\gamma = \alpha_d + j\beta = \frac{k^2\tan\delta}{2\beta} + j\beta \tag{4.3}$$

Thus, the benefit of a hollow SIW, is that the removal of the dielectric substrate will minimize the attenuation due to dielectric attenuation factor α_d. Therefore, the hollow structure, is chosen as the basis for designing a curved SIW structure.

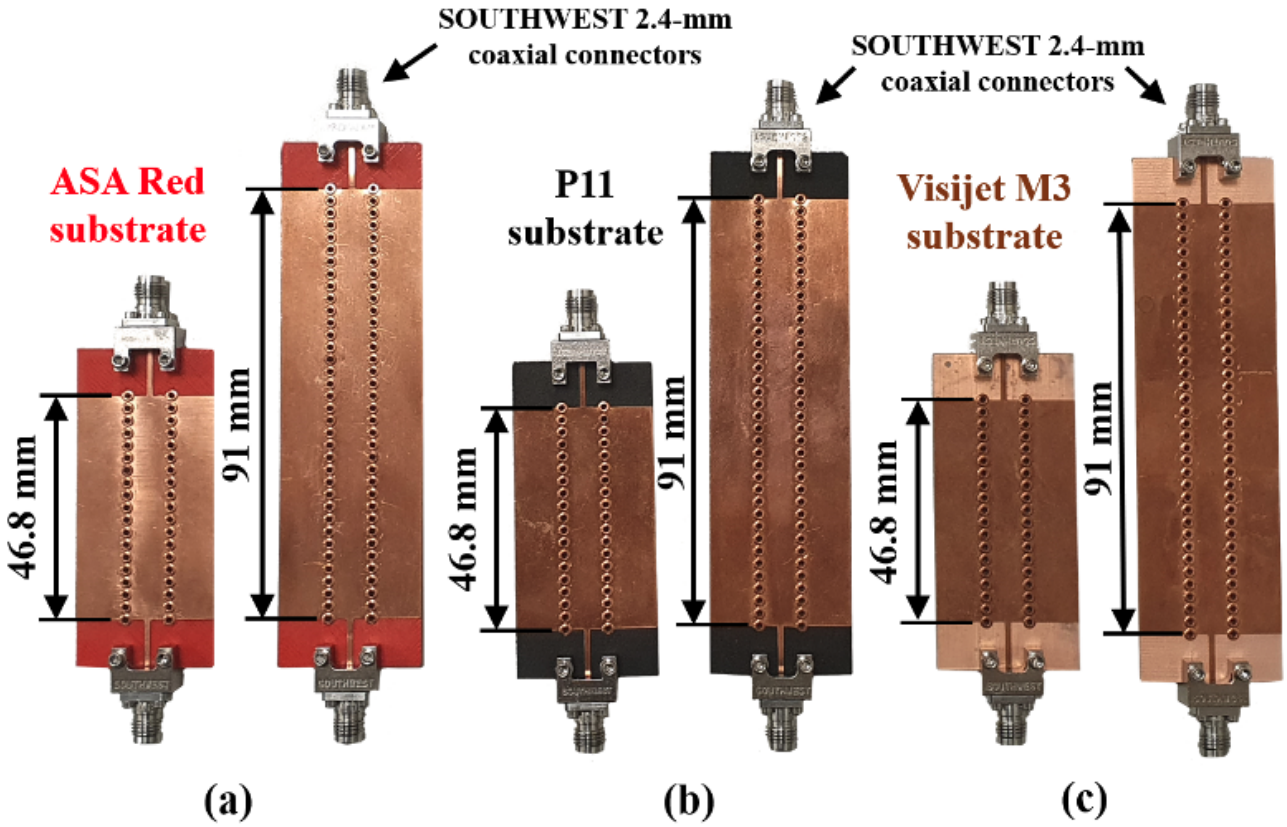

Figure 4.3: Fabricated structures of HSIW pairs with substrates of: (a) ASA Red, (b) PA11 and (c) Visijet M3 dielectric materials

4.3.2 Simulation and Fabrication of straight HSIWs

For this work, we first extract the propagation constant for each regular HSIW structure set. The propagation constant will provide a good indication of which material substrate performs better in a straight section of HSIW. A well-known method to extract the propagation constant is the multi-line calibration technique as described and analyzed in [69].

Since the substrate materials' dielectric properties have been measured in section II, their dielectric values have been used in the commercially available simulation software CST Studio. The waveguide s-parameters are calculated in the simulation software and by using the multi-line technique, their simulated propagation constants are extracted. After determining the simulated propagation constants, it is necessary to obtain the measured propagation constants. These can be obtained after the fabrication and assembly of HSIW structures, that is described in this section.

For this work, two distinct lengths of identical HSIWs were fabricated. This enables

the use of the multi-line calibration approach to analyze and extract the propagation constant of the HSIW as described in [69]. The first HSIW section had a length of 91 mm and the second had a length of 46.8 mm. The University of Leeds' Faculty of Engineering and Physical Sciences facilities were used to fabricate and assemble the HSIWs. By using the water laser cutting technology (Laser MicroJet Cutter) from Synova [70], the top and bottom copper sheets are precisely cut to form the microstrip feeds, matching transitions and the circular via-hole arrays. The copper sheets are supplied by Goodfellow [71] and they are made of 99.9% purity copper sheet with a thickness of 0.15 mm. The HSIW's dielectric substrate is manufactured by using the respective 3D printing processes described earlier. The fabricated copper and dielectric layers were joined together to form the HSIW structure using ready-made through-copper via transitions that were available commercially. These ready-to-use through-copper via transitions were used to mechanically attach and fix the HSIW dielectric between the top and bottom copper sheets. Using the mechanical PCB through-hole plating press tool, the copper vias were mechanically compressed, securely fastening all the SIW components together. For each 3D printed substrate material, a set of two HSIWs of different lengths, was fabricated and assembled, and the samples are shown in Fig. 4.3. In Fig. 4.3(a), the two lengths of HSIW use ASA dielectric substrate with red color, which was printed using the FDM process. The HSIWs in Fig. 4.3(b) use the PA11 dielectric substrate with black color, printed by using the SLS printing process. Finally, Fig. 4.3(c) shows the two HSIWs with the Visijet M3 dielectric substrate, which is clear and was manufactured with the multi-jet printing method. For all the HSIW structures, a SOUTHWEST coaxial connector was mounted on the edge of the substrate, connected to the microstrip at the end of the microstrip-to-HSIW transition. Having completed the fabrication and assembly, the HSIWs were measured and characterized.

4.3.3 Measurement Results

The assembled HSIW structures were measured using the same Agilent E8361A PNA network analyzer. Their S-parameters were measured and exported into an .s2p file. After MATLAB processing and using the multi-line algorithm, their respective measured propagation constants are calculated.

Their simulated and measured propagation constants are plotted in Figs. 4.4,4.5 and 4.6. It can be seen that while the ASA and PA11 materials have demonstrated better simulated performance compared to Visijet M3, their fabrication tolerances and printing inaccuracies have given rise to higher measured attenuation constants. On the other hand, for the Visijet M3 material, the attenuation constant measurement

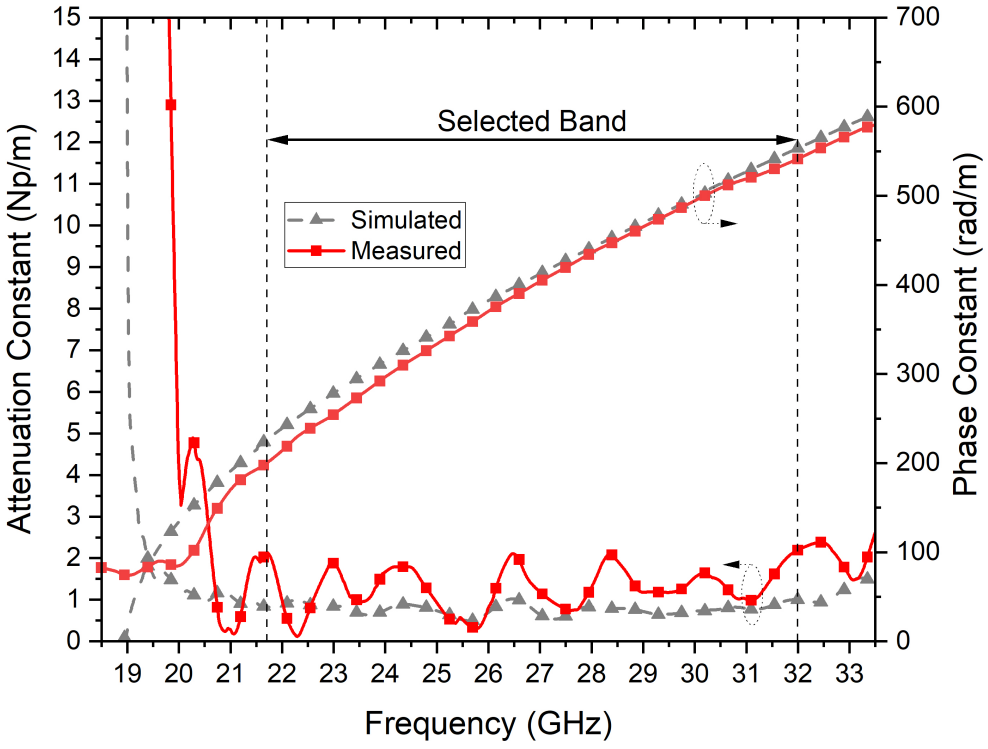

Figure 4.4: Simulated and Measured Propagation constant plot for ASA Red material

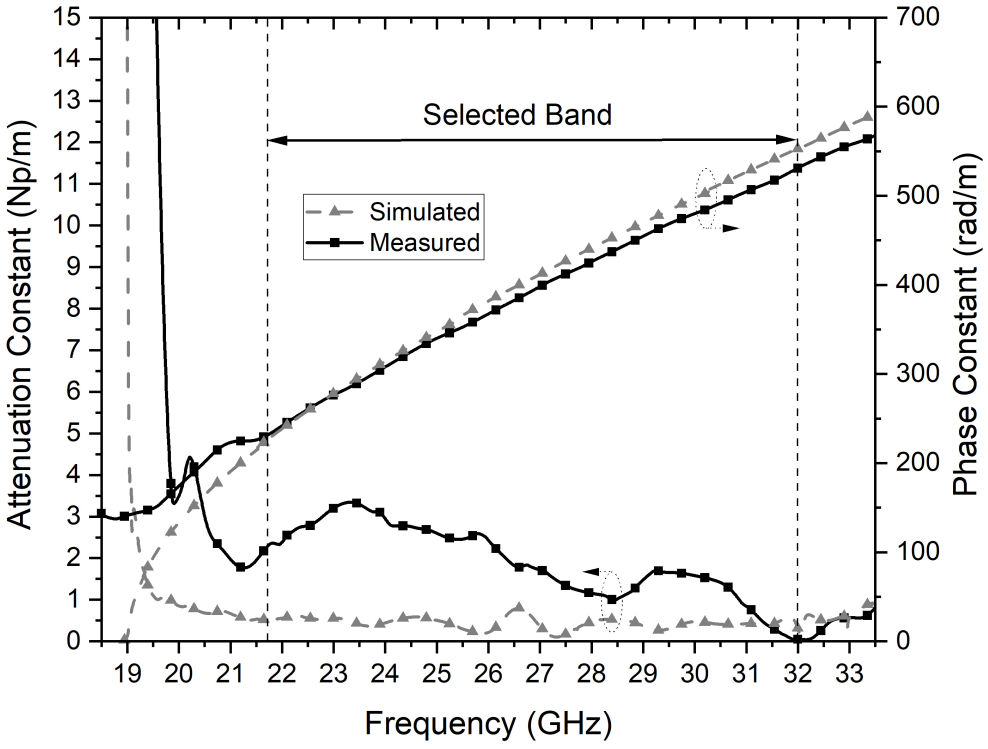

Figure 4.5: Simulated and Measured Propagation constant plot for PA11 black material

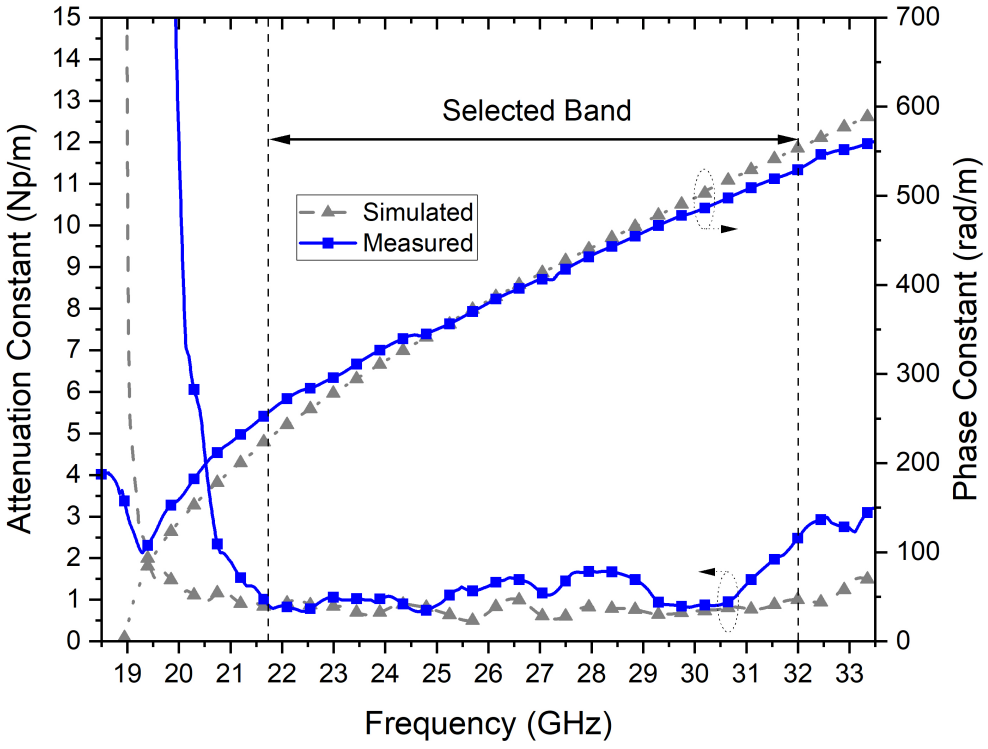

Figure 4.6: Simulated and Measured Propagation constant plot for Visijet M3 crystal material

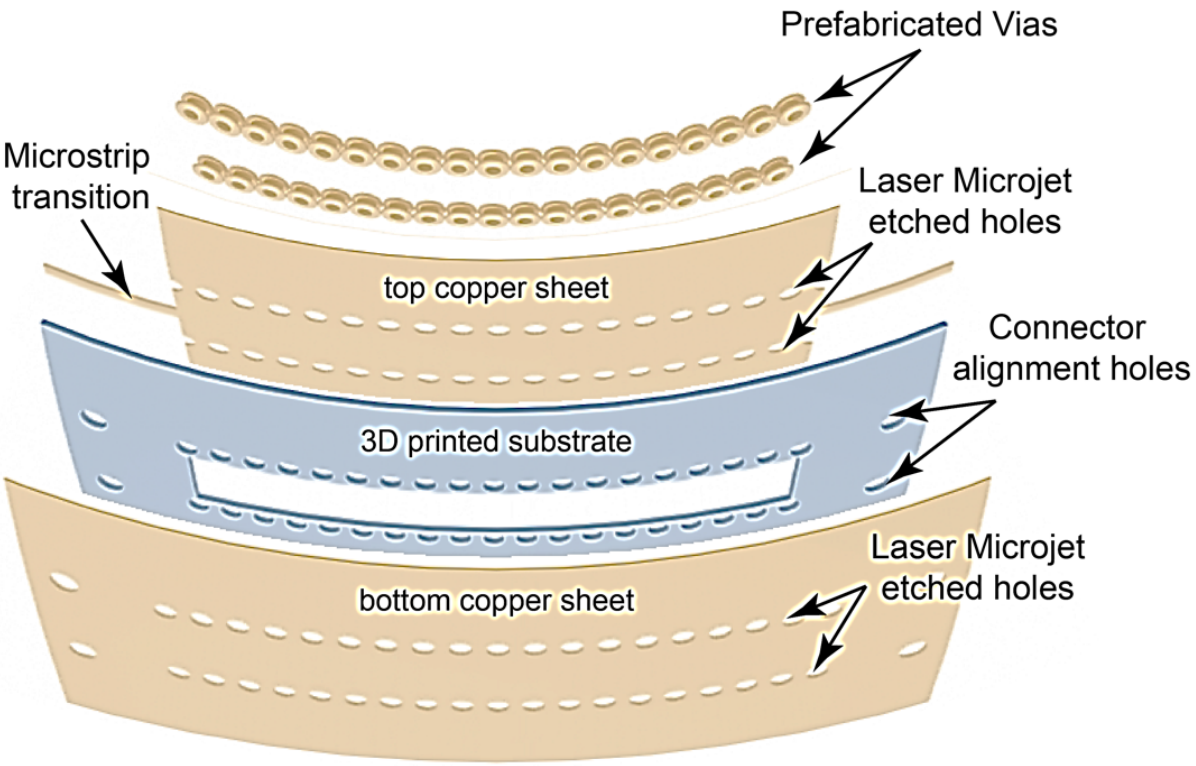

Figure 4.7: Curved HSIW geometrical structure: (a) prefabricated vias, (b) top copper sheet, (c) hollow Visijet M3 substrate, (d) bottom copper sheet

result is in close agreement with the simulated value.

The simulated and measured attenuation constant values for each HSIW with different dielectric substrate material are summarized in Table 4.2.

Among the three dielectric substrate materials, the Visijet M3 crystal has shown the best measured attenuation constant performance and a better agreement between simulation and measurement results. It is also the most precisely printed plastic material with smooth surface finish and the fastest printing speed. Therefore, for the curved section of HSIW, it is decided that a Visijet M3 crystal would be used as the structure's supporting dielectric substrate. The curved hollow SIW section design process is now described.

4.4 Curved HSIW design

4.4.1 Theoretical Analysis and Design

The proposed structured of the 3D printed curved HSIW is illustrated in Fig. 4.7 and consists of four different parts. In this curved structure design, a curved dielectric based on M3 dielectric material, needed to be fabricated, also shown in Fig. 4.7,

Table 4.2: Average Simulated and Measured Attenuation Constant for each of the three materials for the frequency range 21.7-32 GHz

Material	Average simulated attenuation constant (Np/m)	Average measured attenuation constant (Np/m)
ASA Red	0.39	1.27
PA11 Black	0.45	1.92
Visijet M3	0.77	1.20

with light blue color. The curved HSIW structure and all microstrip transitions were designed and optimized by using the 3D full-wave EM simulation package CST Studio. The curved HSIW in this work was optimized for the operating frequency range of 21.7 GHz - 32 GHz, which is suitable for many applications in aerospace, defense, and robotic communications.

Table 4.3: Intensity of maximum propagating and leakage electric field at different radius curvature

HSIW	Maximum propagating field (V/m)	Maximum leakage field (V/m)	Maximum Leakage to Propagating Field Percentage
Straight section	12,516	142	1.13%
125.1 mm	12,428	266	2.14%
41.7 mm	12,403	290	2.34%

The author in [72], has derived a mathematical equation of the wave equation, H, in terms of the propagation constant, γ, for curved rectangular waveguides, as shown in Eq. (4.5), where R is the curvature's radius that is related to the length, s, of the waveguide and its bending angle, θ, shown in Eq. (4.4). It can be seen from Eq. (4.5), that the propagation constant, γ, is inversely proportional to the bending angle, R. This relation is going to be validated with a simulation in CST studio.

$$s = R\theta \tag{4.4}$$

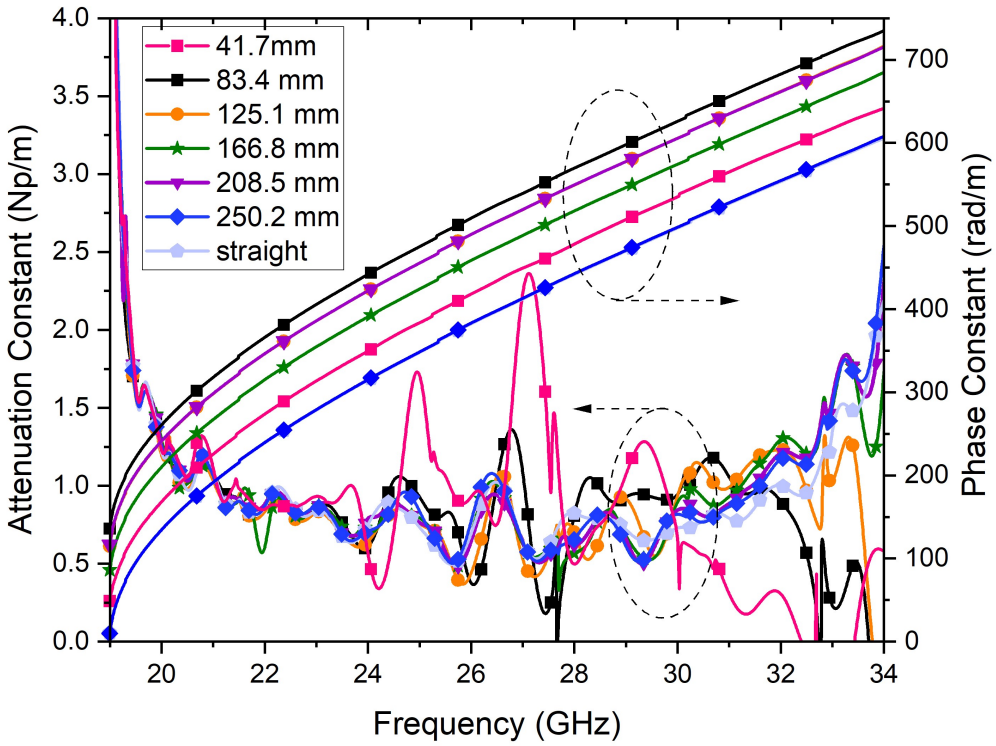

Figure 4.8: Propagation Constant simulation for varying curvature radius of HSIW

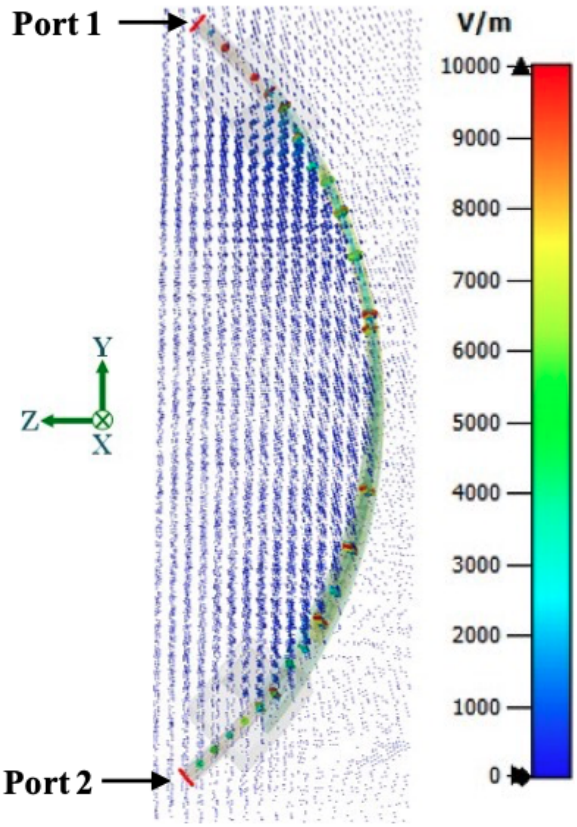

Figure 4.9: Electric field leakage at 26 GHz on sideview of the proposed conformed HSIW

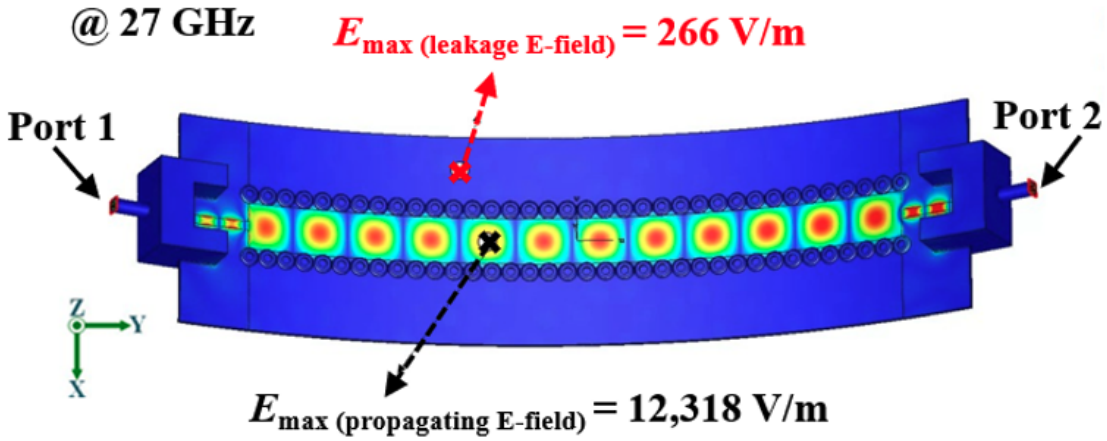

Figure 4.10: Electric Field distribution inside the hollow substrate of the proposed HSIW with length of 111 mm curved on radius R = 125.1mm

$$(1+y/R)^2\frac{d^2h}{dy^2}+(1+y/R)\frac{1}{R}\frac{dh}{dy}+ (1+y/R)^2k^2h=\gamma^2h \tag{4.5}$$

The curved SIW was simulated for use on various curved surfaces with different bending radius. For this work, the curved HSIW was simulated with a bending radius ranging from 41.7 mm to 250.2 mm, with the upper bound of 250.2 mm being closer to a straight section part.

It can be observed, from Fig. 4.8, that by reducing the bending radius and therefore having higher bending angle according to Eq. (4.5), there is an increase in the attenuation constant value. Specifically, the 41.7 mm case shows higher ripples and overall, a higher average value of attenuation constant. In contrast, the higher bending radius value cases like 208.5 mm and 250.2 mm have attenuation constant that is very close to a straight section of HSIW, as one would expect.

Simulation results of the electric field outside and inside the structure are shown in Figs. 4.9 and 4.10, respectively. Fig. 4.9 shows the EM wave leakage on both sides of the curved structure. The front side has much higher leakage compared to the back side. It is notable that the leaked electromagnetic energy in both sides is negligible compared to the magnitude of the EM wave propagating inside the HSIW structure.

Fig. 4.10 shows the EM field leakage that is simulated at 26 GHz, through the inner air-filled structure. The obtained values of maximum propagating field and

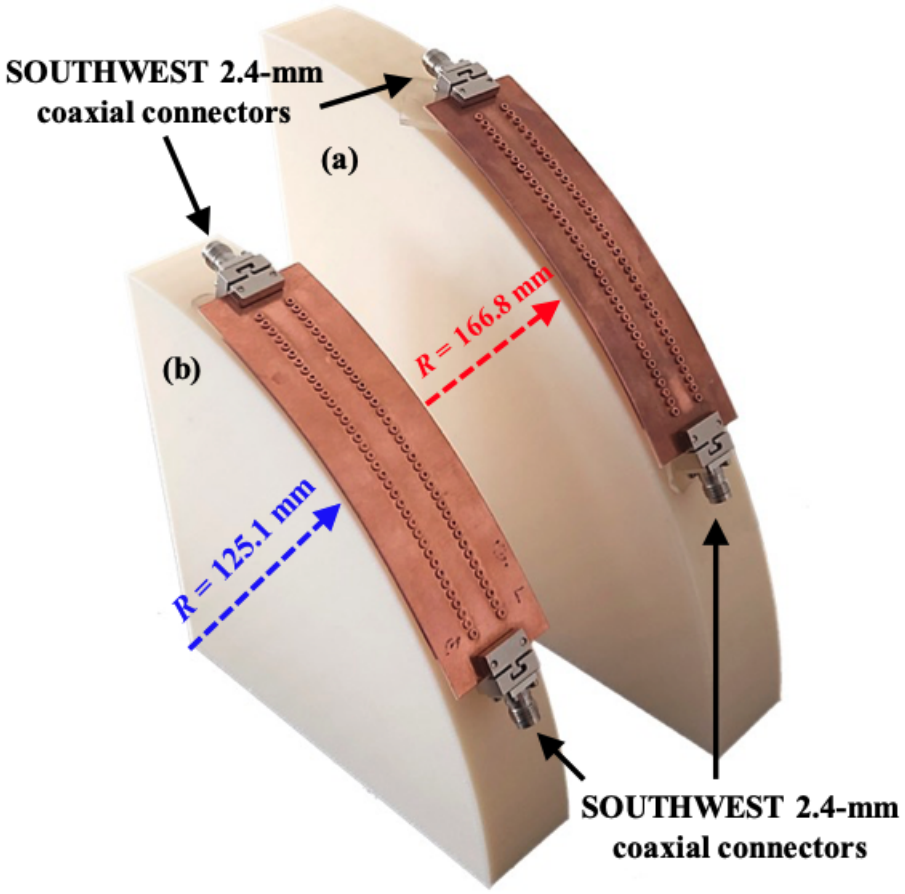

Figure 4.11: The assembled and aligned HSIW with length 91 mm on cylindrical structures with radius (a) 166.8 mm and (b) 125.1 mm

the maximum leakage field for each curved HSIW are shown in Table 4.3. The third column of the Table 4.3 shows the percentage of the maximum leakage field in respect to the total maximum propagating field inside the hollow curved HSIW. The total leakage field value has a negligible percentage value. Therefore, there is very small amount of electromagnetic energy escaping outside of the confined walls of the curved HSIW.

4.4.2 Fabrication and Assembly of Curved HSIWs

Like the straight sections, the curved HSIWs were assembled by using the mechanical through hole pressing machine supplied by Fortex [73], which firmly attaches the copper layers and the dielectric substrate together by compressing the copper rivets also supplied by Fortex.

The CHSIW's dielectric substrates were manufactured using a ProJet MJP 3600 3D printer [74], that can provide high precision and a good surface finish for the 3D printed parts. Overall, this manufacturing process is considered to be a very cost-effective and high-precision process compared to other 3D printing processes like

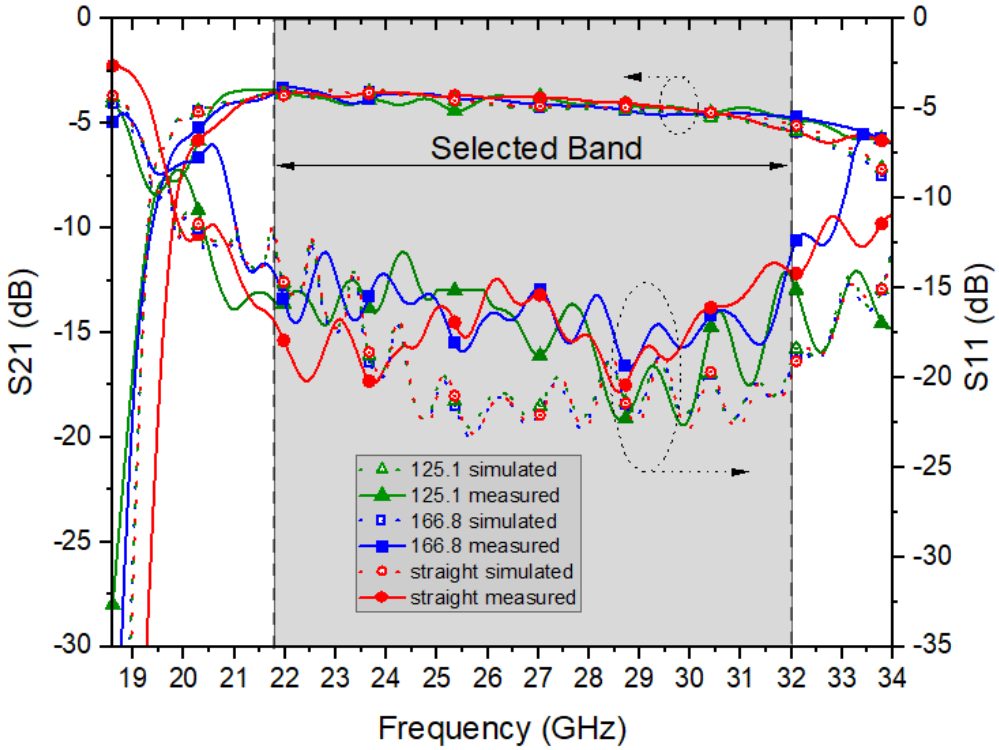

Figure 4.12: Simulated and measured S-parameters of the 91.0 mm-long 3D-printed HSIW at different bending angles

FDM and SLS methods. As in the straight section case, two sets of curved HSIW were fabricated. Each set has curved HSIWs of the same radii but of different lengths of 91 mm and 46.8 mm. The fabricated and assembled curved HSIWs of 91 mm length, but with different radii, are shown in Fig. 4.11.

The first curved HSIW, shown in Fig. 4.11(a), has a radius of curvature of 166.8 mm, while the second curved HSIW in Fig. 4.11(b), has a radius of curvature of 125.1 mm. Both were aligned and attached on a plastic quadrant sample holder as shown in Fig. 4.11. The curved HSIW prototypes had SOUTHWEST 2.4-mm coaxial connectors mounted on both ends of the microstrip feed lines.

4.5 Measurement Results

The S-parameters of the assembled CHSIW are then measured using Agilent E8361A PNA Microwave Network Analyzer with two-port Short-Open-Load-Through (SOLT) calibration, bringing the S-parameter reference plane to the ends of the coaxial cables. The frequency range was set to 15 GHz – 40 GHz on the PNA with 3201 frequency points. Fig. 4.12 shows the measured and simulated reflection, S11, and transmission coefficients, S21, of the fabricated straight section HSIW and curved HSIW prototypes, with a length of 91.0 mm. The measured reflection coefficient,

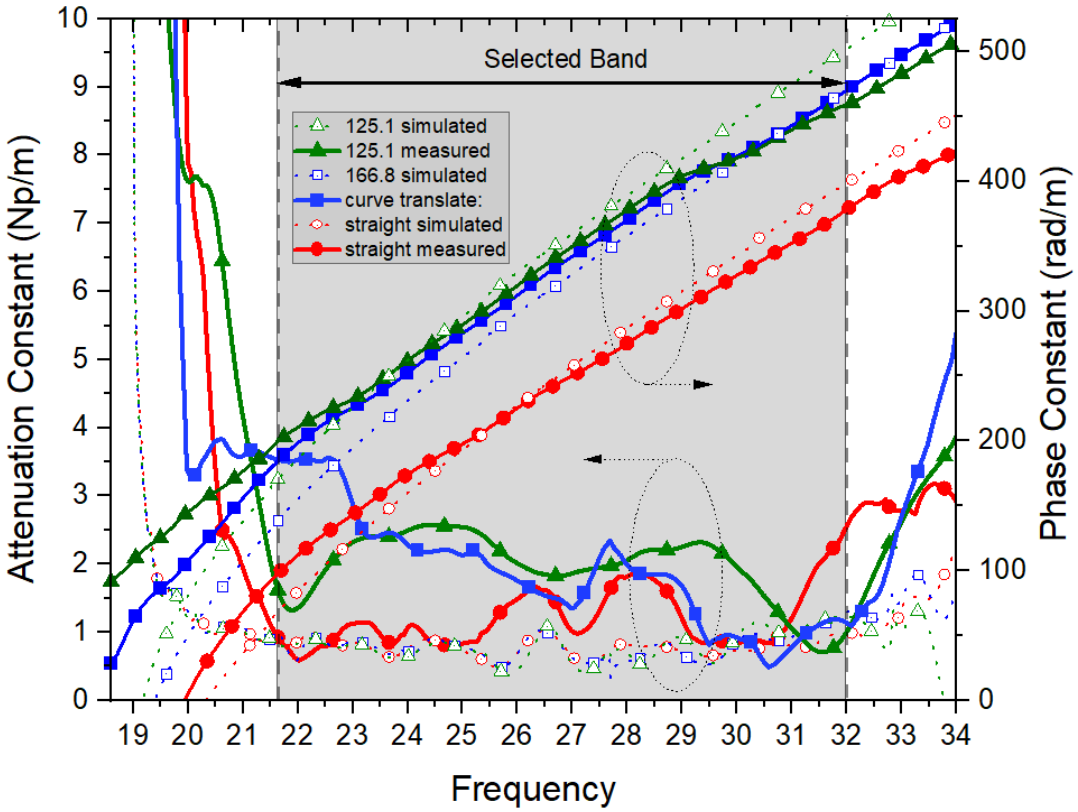

Figure 4.13: Extracted propagation characteristics of the 3D-printed HSIW comparing phase and attenuation constants calculated from the measured and simulated S-parameters at different bending angles

Table 4.4: Average Simulated and Measured Attenuation Constant for each of the two angled and straight section HSIW for the frequency range 21.7-32 GHz

HSIW	Average simulated attenuation constant (Np/m)	Average measured attenuation constant (Np/m)
Straight section	0.77	1.20
166.8 mm	0.78	1.89
125.1 mm	0.79	1.95

S11, of all the 3D-printed HSIW is lower than -10 dB over the operational band of 21.7 GHz – 32 GHz while the S21 is better than -3.56 dB for the entire selected band. By having straight and curved HSIWs of different lengths and using the multi-line calculation technique [69], the attenuation and phase constants of the 3D-printed HSIWs can be extracted from the measured and simulated S-parameters as shown in Fig. 4.13. Over the whole operational band from 21.7 GHz – 33 GHz, the average simulated and measured attenuation constant increases with bending radius decrease as shown in Table 4.4 and this agrees with the simulation results and mathematical derivations. For the lowest curvature radius case, that is an CHSIW bent at a curvature of radius of 125.1 mm, the measured attenuation constant averages at 1.95 Np/m, also shown in Table 4.4. This value of attenuation constant shows that a fabricated curved HSIW, can provide a high-performance solution for curved surface applications.

4.6 Summary

This paper has described a novel design of millimetre-wave curved HSIW structure based on 3D printing of the curved supporting substrate layer, combined with laser cutting of copper layers which are attached with pre-formed vias- holes. The electromagnetic simulations and experimental results have demonstrated that the attenuation constant for a curved HSIW increases with decreasing radius of curvature. At the same time, the fabricated CHSIW is compact, it is broadband, low loss and low cost, and easy to fabricate and integrate with other planar circuit boards. The authors anticipate that the proposed low-cost CHSIW will be used in communication and sensing applications where millimetre-wave low-loss, low-cost and lightweight devices are required. Specifically, the curved HSIW can be attached around a curved surface for a wide range of novel applications such as pipeline inspection, rotary joints and motors, and conformal structures for robotics and aerospace.

4.7 References

[1] D. M. Pozar, Microwave Engineering, 4th ed. Hoboken, NJ: Wiley, 2012.

[2] I. Robertson, N. Somjit and M. Chongcheawchamnan, Microwave and millimetre-wave design for wireless communications. Wiley, 2016.

[3] J. Prisutova, A. Krynkin, S. Tait, and K. Horoshenkov, "Use of fibre- optic sensors for pipe condition and Hydraulics Measurements: A Review," CivilEng, vol. 3, no. 1, pp. 85–113, 2022.

[4] C. H. See, K. V. Horoshenkov, M. T. Ali, and S. J. Tait, "An acoustic sensor for combined sewer overflow (CSO) screen condition monitoring in a drainage infrastructure," Sensors, vol. 21, no. 2, p. 404, 2021.

[5] V. Doychinov et al., "A Study of Wireless Communications Systems for Robotic Communications in Underground Pipes and Ducts," 2021 18th In- ternational Conference on Electrical Engineering/Electronics, Computer, Telecommunications and Information Technology (ECTI-CON), 2021, pp. 209-213, doi: 10.1109/ECTI-CON51831.2021.9454819.

[6] M. Niu, X. Sun, H. Ma, Z. Zhu, T. Huang, and K. Song, "Analysis and design of wireless power transfer system for rotational inertial navigation application," Applied Sciences, vol. 12, no. 13, p. 6392, 2022.

[7] F. T. Talom and S. Turpault, "Additive manufacturing for RF microwave devices: Design, performances and treatments improvement evaluations," 2017 International Conference on Electromagnetics in Advanced Applica- tions (ICEAA), 2017, pp. 1473-1476, doi: 10.1109/ICEAA.2017.8065560.

[8] A. Périgaud, S. Bila, O. Tantot, N. Delhote and S. Verdeyme, "3D printing of microwave passive components by different additive manufacturing technologies," 2016 IEEE MTT-S International Microwave Workshop Series on Advanced Materials and Processes for RF and THz Applications (IMWS-AMP), 2016, pp. 1-4, doi: 10.1109/IMWS-AMP.2016.7588328.

[9] K. Y. Park, M. I. M. Ghazali, N. Wiwatcharagoses and P. Chahal, "Thick 3D Printed RF Components: Transmission Lines and Band- pass Filters," 2018 IEEE 68th Electronic Components and Technology Conference (ECTC), San Diego, CA, USA, 2018, pp. 2186-2191, doi: 10.1109/ECTC.2018.00328.

[10] G. Mitchell, T. Anthony, Z. Larimore and P. Parsons, "Antenna Compar- ison for Additive Manufacturing versus Traditional Manufacturing Meth- ods," 2021 United States National Committee of URSI National Radio Sci- ence Meeting (USNC-

URSI NRSM), 2021, pp. 3-4,
doi: 10.23919/USNC- URSINRSM51531.2021.9336492.

[11] H. Xin and M. Liang, "3-D-printed microwave and THz devices using polymer jetting techniques," Proc. IEEE, vol. 105, no. 4, pp. 737–755, Apr. 2017.

[12] V. W. Sahana and G. T. Thampi, "3D printing technology in industry," in 2018 2nd International Conference on Inventive Systems and Control (ICISC), 2018.

[13] "Additive vs. Subtractive Manufacturing", Formlabs, 2022. [On- line]. Available:
https://formlabs.com/eu/blog/
additive-manufacturing-vs- subtractive-manufacturing/. [Accessed: 09- Oct- 2022].

[14] Z. Wu, M. Liang, W.-R. Ng, M. Gehm and H. Xin, "Terahertz Horn Antenna Based on Hollow-Core Electromagnetic Crystal (EMXT) Structure," IEEE Transactions on Antennas and Propagation, vol. 60, no. 12, pp. 5557-5563,2012.

[15] K. Y. Chan, R. Ramer and R. Sorrentino, "Low-Cost Ku-Band Waveguide Devices Using 3-D Printing and Liquid Metal Filling," IEEE Transactions on Microwave Theory and Techniques, vol. 66, no. 9, pp. 3993-4001, 2018.

[16] W. Deal, "Coplanar waveguide basics for MMIC and PCB design," IEEE Microw. Mag., vol. 9, no. 4, pp. 120–133, Aug. 2008.

[17] Y. CPW Yun, H. S. Kim, and N. Jang, "Study on characteristics of various RF transmission line structure on PES substrates for application to flexible MMIC," ETRI J., vol. 36, no. 1, pp. 1646–1653, Feb. 2014.

[18] D. Deslandes and K. Wu, "Integrated microstrip and rectangular waveg- uide in planar form," IEEE Microw. Wireless Compon. Lett., vol. 11, no. 2, pp. 68–70, Feb. 2001.

[19] Design equations for tapered microstrip-to-Substrate integrated waveguide transitions," in IEEE MTT-S Int. Microw. Symp. Dig., Anaheim, CA, USA, May 2010, pp. 704–707.

[20] M. Bozzi, A. Georgiadis, and K. Wu, "Review of substrate integrated waveguide circuits and antennas," IET Microw., Antennas Propag., vol. 5, no. 8, pp. 909–920, 2011.

[21] K. Wu, D. Deslandes, and Y. Cassivi, "The substrate integrated circuits-a new concept for high-frequency electronics and optoelectronics," in Proc. 6th Int. Conf. Telecommun. Modern Satell., Cable Broadcast. Service, Nis, Yugoslavia, 2003, p. 3

[22] M. Bozzi, M. Pasian, and L. Perregrini, "Modeling of losses in substrate in-

tegrated waveguide components," in Proc. Int. Conf. Numer. Electromagn. Model. Optim. for RF, Microw., Terahertz Appl. (NEMO), Pavia, Italy, May 2014, pp. 1–4.

[23] L. Jin, R. M. Lee, and I. D. Robertson, "Analysis and design of a slotted waveguide antenna array using hollow substrate integrated waveguide," in Proc. Eur. Microw. Conf. (EuMC), Paris, France, Sep. 2015, pp. 1423–1426.

[24] F. Xu and K. Wu, "Guided-wave and leakage characteristics of substrate integrated waveguide," IEEE Trans. Microw. Theory Techn., vol. 53, no. 1, pp. 66–73, Jan. 2005.

[25] A. Belenguer, H. Esteban, A. L. Borja, and V. E. Boria, "Empty SIW technologies: A major step toward realizing low-cost and low-loss microwave circuits," IEEE Microw. Mag., vol. 20, no. 3, pp. 24–45, Mar. 2019.

[26] L. Sun, H.-W. Deng, Y.-F. Xue, J.-M. Zhu, and S.-B. Xing, "Compact balanced BPF and filtering crossover with intrinsic common-mode suppres- sion using single-layered SIW cavity," IEEE Microw. Wireless Compon. Lett., vol. 30, no. 2, pp. 144–147, Feb. 2020.

[27] D. Deslandes and K. Wu, "Accurate modeling, wave mechanisms, and design considerations of a substrate integrated waveguide," IEEE Trans. Microw. Theory Techn., vol. 54, no. 6, pp. 2516–2526, Jun. 2006.

[28] E. Diaz-Caballero, A. Belenguer, H. Esteban, V. E. Boria, C. Bachiller, and J. V. Morro, "Analysis and design of passive microwave components in substrate integrated w aveguide technology," in IEEE MTT-S Int. Microw. Symp. Dig., Ottawa, ON, Canada, Aug. 2015, pp. 1–3.

[29] Y. Li, L.-A. Yang, L. Du, K. Zhang, and Y. Hao, "Design of millime- terwave resonant cavity and filter using 3-D substrate-integrated circular waveguide," IEEE Microw. Wireless Compon. Lett., vol. 27, no. 8, pp. 706–708, Aug. 2017

[30] H. Yousef, S. Cheng, and H. Kratz, "Substrate integrated waveguides (SIWs) in a flexible printed circuit board for millimeter-wave applications," J. Microelectromech. Syst., vol. 18, no. 1, pp. 154–162, Feb. 2009.

[31] N. Ranjkesh and M. Shahabadi, "Reduction of dielectric losses in substrate integrated waveguide," Electron. Lett., vol. 42, no. 21, pp. 1230–1231, Oct. 2006.

[32] F. Bigelli, D. Mencarelli, M. Farina, G. Venanzoni, P. Scalmati, and C. Renghini, "Design and fabrication of a dielectricless substrate-integrated waveguide," IEEE Trans. Compon., Packag., Manuf. Technol., vol. 6, no. 2, pp. 256–261, Feb. 2016

[33] F. Parment, A. Ghiotto, T.-P. Vuong, J.-M. Duchamp, and K. Wu, "Airfilled

SIW transmission line and phase shifter for high-performance and low- cost U-Band integrated circuits and systems," in Proc. Global Symp. Millimeter-Waves (GSMM), Montreal, QC, Canada, May 2015, pp. 1–3.

[34] F. Parment, A. Ghiotto, T.-P. Vuong, J.-M. Duchamp, and K. Wu, "Airfilled substrate integrated waveguide for low-loss and high power-handling millimeter-wave substrate integrated circuits," IEEE Trans. Microw. The- ory Techn., vol. 63, no. 4, pp. 1228–1238, Apr. 2015.

[35] K. Wu, Y. Jian Cheng, T. Djerafi, and W. Hong, "Substrate-integrated millimeter-wave and terahertz antenna technology," Proc. IEEE, vol. 100, no. 7, pp. 2219–2232, Jul. 2012.

[36] E. Silavwe, N. Somjit and I. D. Robertson, "A Microfluidic-Integrated SIW Lab-on-Substrate Sensor for Microliter Liquid Characterization," in IEEE Sensors Journal, vol. 16, no. 21, pp. 7628-7635, Nov.1, 2016, doi: 10.1109/JSEN.2016.2599099.

[37] B. Hong, N. Feng, J. Chen, G. Wang, V. Doychinov, R. Clarke, J. Cunningham, I. Robertson, and N. Somjit, "Substrate integrated Bragg waveguide: An octave-bandwidth single-mode hybrid transmission line for millimeterwave applications," Opt. Exp., vol. 28, pp. 27903–27918 (2020).

[38] G. Savvides et al., "3D Rapid-Prototyped 21-31-GHz Hollow SIWs for Low-Cost 5G IoT and Robotic Applications," in IEEE Access, vol. 9, pp. 11750-11760, 2021, doi: 10.1109/ACCESS.2021.3051180.

[39] L. Jin, R. M. A. Lee and I. Robertson, "Analysis and Design of a Novel Low-Loss Hollow Substrate Integrated Waveguide," in IEEE Transactions on Microwave Theory and Techniques, vol. 62, no. 8, pp. 1616-1624, Aug. 2014, doi: 10.1109/TMTT.2014.2328555.

[40] S. Kim, H. Aubert and M. M. Tentzeris, "An inkjet-printed flexible broadband coupler in substrate integrated waveguide (SIW) technology for sensing, RFID and communication applications," 2014 IEEE MTT-S International Microwave Symposium (IMS2014), Tampa, FL, USA, 2014, pp. 1-4,
doi: 10.1109/MWSYM.2014.6848580.

[41] B. T. Malik, V. Doychinov, S. A. R. Zaidi, I. D. Robertson, N. Somjit, R. Richardson, and N. Chudpooti, "Flexible rectennas for wireless power transfer to wearable sensors at 24 GHz," in Proc. Res., Invention, Innov. Congr. (RI2C), Bangkok, Thailand, Dec. 2019, pp. 1–5, doi: 10.1109/RI2C48728.2019.8999964.

[42] M. Mirzaee, S. Noghanian, L. Wiest and I. Chang, "Developing flexible 3D printed antenna using conductive ABS materials," in 2015 IEEE International Sym-

posium on Antennas and Propagation & USNC/URSI National Radio Science Meeting, 2015.

[43] J. Bito et al., "Millimeter-wave ink-jet printed RF energy harvester for next generation flexible electronics," 2017 IEEE Wireless Power Transfer Conference (WPTC), Taipei, Taiwan, 2017, pp. 1-4, doi: 10.1109/WPT.2017.7953871.

[44] CST-MW Studio, Comput. Simul. Technol., Framingham, MA, USA, 2017.

[45] M. Bozzi, C. Tomassoni, L. Perregrini, R. Bahr, and M. Tentzeris, "Ad- ditive manufacturing of substrate integrated waveguide components," in IEEE MTT-S Int. Microw. Symp. Dig., Chengdu, China, Jul. 2016, pp. 1–4.

[46] R. Bahr et al., "RF characterization of 3D printed flexible materials - NinjaFlex Filaments," 2015 European Microwave Conference (EuMC), Paris, France, 2015, pp. 742-745, doi: 10.1109/EuMC.2015.7345870.

[47] A. A. Abtan, R. C. Richardson and B. Thomas, "Analyzing the 3D printed material Tango plus FLX930 for using in self-folding structure," 2016 International Conference for Students on Applied Engineering (IC- SAE), Newcastle Upon Tyne, UK, 2016, pp. 114-118, doi: 10.1109/IC- SAE.2016.7810171.

[48] B. T. Malik, V. Doychinov, S. A. R. Zaidi, I. D. Robertson, and N. Somjit, "Antenna gain enhancement by using low-infill 3D-printed dielectric lens antennas," IEEE Access, vol. 7, pp. 102467–102476, 2019.

[49] N. Chudpooti, S. Praesomboon, N. Duangrit, N. Somjit, and P. Akkaraekthalin, "An X-band portable 3D-printed lens antenna with integrated waveguide feed for microwave imaging," in Proc. Photon. Electromagn. Res. Symp. (PIERS-Spring), Rome, Italy, Jun. 2019, pp. 487–492.

[50] N. Chudpooti, N. Duangrit, P. Akkaraekthalin, I. D. Robertson, and N. Somjit, "220-320 GHz hemispherical lens antennas using digital light processed photopolymers," IEEE Access, vol. 7, pp. 12283–12290, 2019

[51] N. Chudpooti, N. Duangrit, P. Akkaraekthalin, I. D. Robertson, and N. Somjit, "Electronics-based free-space terahertz measurement using hemi- spherical lens antennas," IEEE Access, vol. 7, pp. 95536–95546,2019.

[52] "Selective Laser Sintering (SLS) — 3D Printing — Protolabs", Protolabs.com, 2022. [Online]. Available: https://www.protolabs.com/services/3d- printing/selective-laser-sintering/. [Accessed: 08- Oct- 2022].

[53] "Guide to Selective Laser Sintering (SLS) 3D Printing", Formlabs, 2022. [On-

line]. Available: https://formlabs.com/eu/blog/what-is-selective-laser- sintering/. [Accessed: 08- Oct- 2022].

[54] "Fused deposition modeling - FDM 3D printers," Stratasys. [Online]. Available: https://www.stratasys.com/en/guide-to-3d- printing/technologies-and-materials/fdm-technology/. [Accessed: 29- Oct-2022].

[55] "Multijet printing," 3D Systems, 15-Feb-2022. [Online]. Available: https://www.3dsystems.com/multi-jet-printing. [Accessed: 29-Oct-2022].

[56] "PA11-Black", Protolabs.com, 2022. [Online]. Available: https://www.protolabs.com/media/uzylqy5i/sls-pa-11-black-120821.pdf. [Accessed: 15- Oct- 2022].

[57] "ASA: A UV Stable 3D Printing Material", Stratasys.com, 2022. [Online]. Available: https://www.stratasys.com/en/materials/materials-catalog/fdm- materials/asa/. [Accessed: 15- Oct- 2022].

[58] "VisiJet M3 Crystal (MJP) — 3D Systems", 3D Systems, 2022. [Online]. Available: https://www.3dsystems.com/materials/visijet-m3-crystal. [Ac- cessed: 15- Oct- 2022].

[59] N. Duangrit, B. Hong, A. D. Burnett, P. Akkaraekthalin, I. D. Robert- son, and N. Somjit, "Terahertz dielectric property characterization of photopolymers for additive manufacturing," IEEE Access, vol. 7,pp. 12339–12347, 2019

[60] C.-K. Lee, J. McGhee, C. Tsipogiannis, S. Zhang, D. Cadman, A. Goulas,T. Whittaker, R. Gheisari, D. Engstrom, J. Vardaxoglou, and W. Whittow, "Evaluation of microwave characterization methods for additively manu- factured materials," Designs, vol. 3, no. 4, p. 47, Sep. 2019.

[61] E. Márquez-Segura, S. -H. Shin, A. Dawood, N. M. Ridler and S. Lucyszyn, "Microwave Characterization of Conductive PLA and Its Ap- plication to a 12 to 18 GHz 3-D Printed Rotary Vane Attenuator," in/emphIEEE Access, vol. 9, pp. 84327-84343, 2021, doi: 10.1109/AC- CESS.2021.3087012.

[62] K. Y. You, "Materials characterization using microwave waveguide system," IntechOpen, 11-Jan-2017. [Online]. Available: https://www.intechopen.com/chapters/53062. [Accessed: 22-Oct-2022].

[63] Ward, A. (2016). Dielectric materials for advanced applications. 10.13140/RG.2.1.3481.5600.

[64] "85071E materials measurement software - keysight." [Online]. Available: https://www.keysight.com/us/en/assets/7018-01155/technical- overviews/

5988-9472.pdf. [Accessed: 12-Nov-2022].

[65] Lee, Chih-Kuo & McGhee, Jack & Tsipogiannis, Christos & Zhang, Shiyu & Cadman, Darren & Goulas, Athanasios & Whittaker, Tom & Gheisari, Reza & Engstrom, Daniel & Vardaxoglou, John & Whittow, Will. (2019). "Evaluation of Microwave Characterization Methods for Additively Manufactured Materials". Designs. 3. 47. 10.3390/designs3040047.

[66] "WR-34 waveguide to Coax Adapter," Eravant. [Online]. Available: https://www.eravant.com/wr-34-waveguide-to-2-4-mm-f-coax-adapter- end-launch. [Accessed: 22-Oct-2022].

[67] "WR-34 waveguide straight section," Eravant. [Online]. Available: https://www.eravant.com/wr-34-waveguide-1-25-waveguide-straight- section. [Accessed: 22-Oct-2022].

[68] N. Chudpooti, G. Savvides, N. Duangrit, P. Akkaraekthalin, I. D. Robert- son and N. Somjit, "Harmonized Rapid Prototyping of Millimeter-Wave Components using Additive and Subtractive Manufacturing," in IEEE Transactions on Components, Packaging and Manufacturing Technology, 2022, doi: 10.1109/TCPMT.2022.3181886

[69] M. D. Janezic and J. A. Jargon, "Complex permittivity determination from propagation constant measurements," IEEE Microw. Guided Wave Lett., vol. 9, no. 2, pp. 76–78, Feb. 1999.

[70] Synova. MCS 300 Laser-MicroJet Cutter. Accessed: Oct. 2, 2022. [On- line]. Available: www.synova.ch/machines/mcs-series/

[71] Goodfellow. Supplier for Materials. Accessed: Oct. 2, 2022. [Online].Available: http://www.goodfellow.com

[72] L. Lewin, "Propagation in curved and twisted waveguides of rectangular cross-section", Proceedings of the IEE - Part B: Radio and Electronic Engineering, vol. 102, no. 1, pp. 75-80, 1955. Available: 10.1049/pi-b-1.1955.0013 [Accessed 18 September 2022].

[73] FORTEX. PTH400 Mechanical Through Hole Press. Accessed: Sep. 30, 2022. [Online]. Available: http://www.fortex.co.uk/download/ pth400- mechanical-through-hole-press/.

[74] Projet MJP 3600 series (2021) 3D Systems. Available at: https://www.3dsystems.com/3d-printers/projet-mjp-3600-series (Accessed: October 23, 2022).

Chapter 5

Conclusion and Future Work

5.1 Summary

The design study conducted in this thesis, compared the figure of merit for different planar transmission lines like the microstrip or the strip-line with a 3D-printed SIW (Substrate Integrated Waveguide). The results showed that while conventional planar transmission lines suffer from radiation and material losses at higher frequencies, the SIWs maintain better their signal power level, even up to sub-GHz range. On the other hand, non-planar RF transmission lines like the Rectangular Waveguide (RWG) while it outperforms SIW's propagation loss, is considered bulky and incompatible with modern wireless PCB applications. Therefore the SIW technology offers good compatibility with planar PCB devices while still maintaining a high level of RF performance.

The thesis also investigated existing and various SIW designs and summarized their advantages and disadvantages. It took into consideration their performance level, fabrication complexity and cost. From this investigation, it was concluded that the existing SIW fabrication methods, fulfil only the performance requirement for high frequency applications. Therefore the thesis goes a step beyond, to explore potential HSIW (Hollow Substrate Integrated Waveguide) designs that outperform the SIW designs in terms of performance and cost. The analytical investigation of the design and fabrication of existing HSIW technologies led to the conclusion that this emerging technology holds great promise for future high-speed communication systems. Specifically, this thesis examines many design methodologies, through the literature, which utilize the dielectric substrate removal approach, which can be found under different names such as air-filled SIW, empty SIW or hollow SIW.

This study proposes a new design and fabrication methodology for HSIW devices

and the thesis proves that a 3D-printed HSIW can achieve low attenuation loss and high signal integrity, making it a viable alternative to traditional planar transmission lines, even a good alternative to SIW components.

The design and fabrication methodology presented in chapter 2, starts with the selection of the optimum HSIW geometry based on the simulation results that are obtained using electromagnetic (EM) simulation software. This is followed by optimizing the HSIW dimensions to achieve the desired HSIW impedance that will match with the microstrip interconnect and SMA connectors. The final step in the design process involves the fabrication and testing of the 3D-printed HSIW structure to validate the simulation results.

The fabrication process has utilized water-laser jet to produce precision cut copper sheets, which compose the top and bottom enclosures of the device. Furthermore, a 3D printed dielectric substrate was produced using a Stratasys 3D printer. The methodology of fabrication and assembly was explained in detail in the main part of the thesis.

It was observed that the fabrication process of the 3D-printed HSIWs, suffered from some minor tolerances. Specifically, the electrical connections between the patterned copper sheets and prefabricated through-substrate copper vias were not perfect, and the prefabricated copper vias were slightly affected by the manual pressing force during assembly. However, it was noted that this fabrication process can be further optimized and automated in the future.

After lab measurements performed on the manufactured HSIW, showed that, the signal integrity of the HSIW was confirmed by the low attenuation loss extracted mathematically using the S-parameter measurements. Additionally, the HSIWs demonstrated a wide bandwidth in the Ka-band range.

The measured results of the 3D-printed HSIW also showed that the device has the required performance needed to be used for high frequency communication systems and in addition it can easily be integrated with other RF passive and active components such as filter, combiner/splitter, and antenna.

In terms of cost-effectiveness, the designed 3D-printed HSIW proved to be a viable alternative to traditional planar transmission lines, since it has lower costs of material fabrication and material assembly. While some conventional transmission lines using more expensive substrate materials showed slightly lower attenuation constants compared to a dielectric-based HSIW, the cost factor outperforms the slight difference in attenuation loss. Therefore, 3D-printed HSIWs may offer a cost-effective solution for high-speed communication systems without greatly compromising performance.

Apart from the cost-effectiveness and improved performance, the proposed HSIW design also offers other significant advantages over conventional planar transmission lines, such as higher power handling capacity, and improved electromagnetic shielding. The aforementioned benefits exhibited by the proposed HSIW make it an attractive option for future research and development.

The chapter 3 of the thesis, demonstrates that a HSIW transmission line can give an excellent propagation loss of 1.56 Np/m for a wide bandwidth namely from the frequency range 21-31-GHz. Even with some minor fabrication and assembly issues, the 3D-printed HSIWs can achieve this low average value of signal propagation loss , which is among the lowest attenuation loss published to date. Moreover, it gives some potential applications where the HSIW can be used. Some of these include a slot antenna array in a MIMO configuration.

The chapter 4 of the thesis, demonstrates the feasibility to built curved HSIW devices for high frequency communication applications. Initially this part of the thesis, goes into a preliminary analysis of dielectric materials that can be used as dielectric substrates of a straight HSIW. The author has chosen three materials that were printed with different 3D printing technologies, therefore a comparison of the performance can be made between these materials. To examine these materials better and have a good indication of their dielectric behaviour, their dielectric properties are measured using the waveguide reflection resonance technique. The dielectric constant and loss tangent of these materials are calculated using the Nicholson-Ross-Weir (NRW) mathematical conversion method. After this material analysis, straight sections of HSIW are manufactured which their substrates are built with the materials examined previously. The straight sections of HSIW are measured using the Vector Network Analyzer and their s-parameters are measured and plotted. That gave a good indication on which material is most suitable to be used as the dielectric substrate of a curved HSIW. Finally, this dielectric material is used to build sets of curved HSIW with a specific bending radii and are measured on VNA, that produced their corresponding s-parameters. Following the same approach as with the straight sections, their propagation losses are extracted using the multi-line calibration technique. It is shown that, for the whole operational band from 22-32-GHz, the average simulated and measured attenuation constant increases with bending radius. For the lowest curvature radius case, that is an CHSIW bent at a curvature of radius of 125.1 mm, the measured attenuation constant averages at 1.95 Np/m.At the same time, the fabricated CHSIW is compact, it is broadband, low loss and low cost, and easy to fabricate and integrate with other planar circuit boards. In conclusion, this part of this thesis, has proved that many dielectric materials can be used as substrates for straight section of HSIW. It has also proved by simulation

and measurement that by increasing the curvature radius, it respectively increases the propagation loss.

Overall, the findings of this thesis contribute to the general knowledge on the potential of 3D printing technology applied in high-speed RF communication systems.

5.2 Potential Applications

The proven Hollow SIW device can be applied in a variety of industrial and research applications. The 3D-printed HSIW can be used in flexible conformal structures, such as in robotic communication systems where multiple transceiver RF chains are required and the antennas are to be integrated into the system.

Specifically, it could be used utilized as communication device on the arm of a robot. This HSIW can be potentially designed with a curved substrate, and wrapped around a conformal structure e.g. a cylindrical shape, that is part of a robotic arm. This gives the benefit of transferring RF power from one edge of the robot to the other.

Another application could be in the sector of wireless mobile networks. The huge expansion and development of wireless mobile networks has led to the need for higher speeds, more devices and higher power needed. Therefore the straight HSIW or curved HSIW could be used in a 5G or 6G base station. It can handle high amount of RF power and therefore can send the signal to be transmitted from directional and omni-directional antennas of a mobile network base station. This application can be a performance enhancement, since it will help propagate high RF power with minimum losses and can be manufactured from companies at a low cost.

The HSIW can also be applied in civilian and military applications like surveillance, detection, and tracking which are being deployed by radar systems. Specifically, it can be applied and used in the RF chain and RF front ends of a radar system that is being used to detect incoming threats in a military controlled area. Moreover it can be used as a transmission medium around a satellite payload. This could help remove bulky Rectangular waveguides that may be present and being used on the electronic system of a satellite and furthermore contribute to minimizing the losses associated with RF propagation around and near the satellite system. Thus the benefit of eliminating energy losses could contribute to more efficient and power consuming satellite with is supply battery lasting for longer periods of time.

5.3 Future Work

This thesis has demonstrated that RF devices can be designed and fabricated using both additive and subtractive manufacturing techniques. Specifically, the thesis has shown that the proposed hollow substrate integrated waveguide (HSIW) component performs exceptionally well at very high frequencies and can be used as a viable alternative to existing SIW devices.

Further research could investigate the feasibility of using different 3D printing materials and techniques to further improve the performance and cost-effectiveness of HSIW. Such materials may include higher-performing thermoplastics and composite materials such as carbon fiber-reinforced polymers (CFRP) and ceramic composites. These materials could potentially improve the mechanical stability and thermal management of the HSIWs, allowing for higher operating temperatures and longer lifespan. In addition, further research could investigate the use of additive manufacturing techniques to fabricate HSIWs with even higher precision and smoother surfaces, which could further reduce signal attenuation.

Based on the excellent performance of the HSIW, it can be concluded that this RF device has great potential to serve as the foundation for future designs of passive and active components. One way to design an HSIW filter is by utilizing the SIW cavity filter method, which can synthesize a band-pass filter as previously demonstrated in [36]. Another method that can be adopted to design an HSIW filter is the inductive post method for creating a dual inductive post integrated waveguide filter, as outlined in the same publication. The inductive posts can be easily replaced by using the copper rivets and mechanical through-hole plating method that was utilized in this thesis work.

Another design can be an SIW slot array antenna in the Ka band. The author in [37], proposed this design that consists of a microstrip to SIW transition feeding a SIW antenna, which was analyzed using the CST Microwave Studio full-wave electromagnetic simulator. To validate its Ku band operation, the design was evaluated based on its return loss and radiation pattern characteristics. Therefore this design pattern could be realized by utilizing the proposed HSIW structure. The use of a hollow SIW structure, would eliminate the propagation losses in the antenna further, enhance its emitted electromagnetic wave and consequently increase the antenna gain.

With both simulated and measured results, a substrate integrated waveguide (SIW) circulator with a metallic-via inductive window is presented in [38] and investigated. The results show a 20dB isolation with a 13.7 percent fractional bandwidth at the

center frequency of 9.41 GHz. Additionally, a small SIW to microstrip transition with an embedded feed-line is included in this design to connect with microstrip circuits. As it can be seen from that work, the insertion loss is -0.317 dB. It is anticipated that by replacing the SIW structure of this circulator with a HSIW structure, the insertion loss will further reduced, since the transmission losses will be eliminated due to the hollow structure proposed in this thesis. Correspondingly it is anticipated that the return loss will further decrease, since more wave will be propagated effectively in the structure.

The article in [39], provides a thorough analysis of various SIW power dividers and discussed their evolution over the previous ten years. Effective power dividers/combiners are needed because there is such a high demand for creating mm-wave circuits and systems. This is where SIW technologies have had a huge impact. Such a SIW method removed the disadvantages of both microstrip and the traditional rectangular waveguide and combined their benefits. However, more research is needed to address the practical integration and fabrication issues. One significant improvement again here, is to utilized this thesis HSIW structure and hence the power dividers performance is expected to drastically improve. The Wilkinson power divider demonstrates an excellent insertion loss of 3.5 dB and this value can be further optimized with the substitution of SIW structure with the proposed HSIW.

In [40], a certain 5G frequency band is proposed to be covered by a simple, compact, wideband planar SIW phase shifter with the advantages of wide operation bandwidth, large phase shift range, and easy-to-make construction. Specifically, for the proposed SIW phase shifter, two slots are symmetrically etched on the top surface of SIW with microstrip feed line. The SIW is built on a dielectric substrate of RO4003C (the dielectric constant of 3.38, thickness of 0.508 mm, and loss tangent of 0.0027). These slots are contributing to the phase shift of the SIW phase shifter. This phase shifter has achieved a good performing insertion loss of 0.7 dB and a return loss of 15 dB. Both values could be further optimized by replacing the SIW structure of this phase shifter with the proposed HSIW structure.

Finally an SIW Horn antenna can be constructed using the proposed HSIW fabrication method. As it can be seen in [41], an SIW Horn antenna structure is designed, fabricated, and tested. It shows its best performance at the intended frequency at 30 GHz for over 1 GHz of bandwidth. Similarly, an HSIW horn antenna design can be built and optimized using the HSIW structure of this thesis. This is expected to furthermore decrease dielectric losses and improve the antenna gain response for the operating frequency range. A draft design has been completed in CST Studio as shown in Figure 5.1 In a nutshell, most passive and active devices which employ the

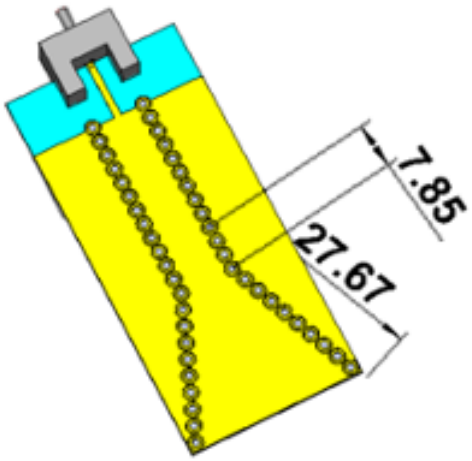

Figure 5.1: Proposed HSIW Horn Antenna

traditional PCB SIW topology, can be converted into the proposed HSIW design presented in this thesis.

Bibliography

[1] A. Kondur, "Evolution of wireless mobile communication networks and future of cellular market in india," vol. 2, Oct. 2012, pp. 453–462.

[2] R. Galazzo, *Timeline from 1g to 5g: A brief history on cell phones*, Jul. 2022.

[3] Q. Liu, S. Sarfraz, and S. Wang, "An overview of key technologies and challenges of 6g," Nov. 2020.

[4] X. Xu, B. Li, and Y. Wang, "Exploration of the principle of 6g communication technology and its development prospect," in *2022 International Conference on Electronics and Devices, Computational Science (ICEDCS)*, 2022, pp. 100–103.

[5] H. Cui *et al.*, "Space-air-ground integrated network (sagin) for 6g: Requirements, architecture and challenges," *China Communications*, vol. 19, no. 2, pp. 90–108, 2022.

[6] M. Dahiya, "Evolution of wireless lan in wireless networks," *International Journal on Computer Science and Engineering*, vol. 9, pp. 109–113, Mar. 2017.

[7] V. Santos and J. Neves, "Mobile satellite communications: An overview," May 2005.

[8] F. Vatalaro, G. Corazza, C. Caini, and C. Ferrarelli, "Analysis of leo, meo, and geo global mobile satellite systems in the presence of interference and fading," *IEEE Journal on Selected Areas in Communications*, vol. 13, no. 2, pp. 291–300, 1995.

[9] R. Esmailzadeh, "Satellite communications," in *Broadband Telecommunications Technologies and Management*. 2016, pp. 257–281.

[10] D. M. Pozar, *Microwave engineering*. John Wiley and Sons, ., 2005.

[11] I. Robertson, N. Somjit, and M. Chongcheawchamnan, *Microwave and Millimetre-wave design for wireless communications*. Wiley Blackwell, 2016.

[12] S. Direct, *Rectangular waveguide*, 2023.

[13] A. Verma, "Microstrip line," in Jun. 2021, pp. 261–299.

[14] F. Xu and K. Wu, "Guided-wave and leakage characteristics of substrate integrated waveguide," *IEEE Transactions on Microwave Theory and Techniques*, vol. 53, no. 1, pp. 66–73, 2005.

[15] D. Deslandes and K. Wu, "Integrated microstrip and rectangular waveguide in planar form," *IEEE Microwave and Wireless Components Letters*, vol. 11, no. 2, pp. 68–70, 2001.

[16] K. Wu, D. Deslandes, and Y. Cassivi, "The substrate integrated circuits - a new concept for high-frequency electronics and optoelectronics," in *6th International Conference on Telecommunications in Modern Satellite, Cable and Broadcasting Service, 2003. TELSIKS 2003.*, vol. 1, 2003, P–III.

[17] J. E. Rayas-Sanchez and V. Gutierrez-Ayala, "A general em-based design procedure for single-layer substrate integrated waveguide interconnects with microstrip transitions," in *2008 IEEE MTT-S International Microwave Symposium Digest*, 2008, pp. 983–986.

[18] S. Kumari and S. Srivastava, "Losses in waveguide and substrate integrated waveguide (siw) for ku band: A comparison," *International Journal of Modern Engineering Research (UMER)*, vol. 3, pp. 53–57, Jan. 2013.

[19] M. I. Nawaz, H. Zhao, and M. Kashif, "Substrate integrated waveguide (siw) to microstrip transition at x-band," Jul. 2021.

[20] M. Bozzi, M. Pasian, and L. Perregrini, "Modeling of losses in substrate integrated waveguide components," in *2014 International Conference on Numerical Electromagnetic Modeling and Optimization for RF, Microwave, and Terahertz Applications (NEMO)*, 2014, pp. 1–4.

[21] K. Güvenli, S. Yenikaya, and M. Seçmen, "Design and implementation of substrate integrated waveguide filter to work on x-band and ku-band," in *2018 9th International Conference on Ultrawideband and Ultrashort Impulse Signals (UWBUSIS)*, 2018, pp. 198–200.

[22] M. Bozzi, A. Georgiadis, and K. Wu, "Review of substrate-integrated waveguide circuits and antennas," *Microwaves, Antennas & Propagation, IET*, vol. 5, pp. 909 –920, Jul. 2011.

[23] Y. Fu, K. Y. Chan, M. G. Banciu, and R. Ramer, "Broadband y-type divider in ku-band using substrate integrated waveguide," in *2019 International Semiconductor Conference (CAS)*, 2019, pp. 57–60.

[24] W. Bo, Z. Xu, L. Hao, X. Meijuan, and J. Liao, "Substrate integrated waveguide cross-coupling filter with multilayer hexagonal cavity," in *2013 International Workshop on Microwave and Millimeter Wave Circuits and System Technology*, 2013, pp. 221–224.

[25] X.-P. Chen and K. Wu, "Substrate integrated waveguide filter: Basic design rules and fundamental structure features," *Microwave Magazine, IEEE*, vol. 15, pp. 108–116, Jul. 2014.

[26] N. Ranjkesh and M. Shahabadi, "Reduction of dielectric losses in substrate integrated waveguide," *Electronics Letters*, vol. 42, pp. 1230 –1231, Nov. 2006.

[27] F. Parment, A. Ghiotto, T.-P. Vuong, J.-M. Duchamp, and K. Wu, "Air-filled substrate integrated waveguide for low-loss and high power-handling millimeter-wave substrate integrated circuits," *IEEE Transactions on Microwave Theory and Techniques*, vol. 63, no. 4, pp. 1228–1238, 2015.

[28] N. H. Nguyen, F. Parment, A. Ghiotto, K. Wu, and T. P. Vuong, "A fifth-order air-filled siw filter for future 5g applications," in *2017 IEEE MTT-S International Microwave Workshop Series on Advanced Materials and Processes for RF and THz Applications (IMWS-AMP)*, 2017, pp. 1–3.

[29] A. Belenguer, H. Esteban, and V. E. Boria, "Novel empty substrate integrated waveguide for high-performance microwave integrated circuits," *IEEE Transactions on Microwave Theory and Techniques*, vol. 62, no. 4, pp. 832–839, 2014.

[30] L. Jin, R. M. A. Lee, and I. Robertson, "Analysis and design of a novel low-loss hollow substrate integrated waveguide," *IEEE Transactions on Microwave Theory and Techniques*, vol. 62, no. 8, pp. 1616–1624, 2014.

[31] A. Belenguer, A. L. Borja, H. Esteban, and V. E. Boria, "High-performance coplanar waveguide to empty substrate integrated coaxial line transition," *IEEE Transactions on Microwave Theory and Techniques*, vol. 63, no. 12, pp. 4027–4034, 2015.

[32] F. Bigelli *et al.*, "Design and fabrication of a dielectricless substrate-integrated waveguide," *IEEE Transactions on Components, Packaging and Manufacturing Technology*, vol. 6, no. 2, pp. 256–261, 2016.

[33] F. Parment, A. Ghiotto, T.-P. Vuong, J.-M. Duchamp, and K. Wu, "Air-filled siw transmission line and phase shifter for high-performance and low-cost u-band integrated circuits and systems," in *Global Symposium on Millimeter-Waves (GSMM)*, 2015, pp. 1–3.

[34] N. Nguyen, I. A. Ghiotto, A. Vilcot, K. Wu, and T. P. Vuong, "Half-mode slab air-filled substrate integrated waveguide (safsiw)," in *2021 IEEE MTT-S International Microwave Symposium (IMS)*, 2021, pp. 335–338.

[35] N. Shahrubudin, T. Lee, and R. Ramlan, "An overview on 3d printing technology: Technological, materials, and applications," *Procedia Manufacturing*, vol. 35, pp. 1286–1296, 2019, The 2nd International Conference on Sustainable Materials Processing and Manufacturing, SMPM 2019, 8-10 March 2019, Sun City, South Africa.

[36] S. S. Sabri, B. H. Ahmad, and A. R. B. Othman, "A review of substrate integrated waveguide (siw) bandpass filter based on different method and design," in *2012 IEEE Asia-Pacific Conference on Applied Electromagnetics (APACE)*, 2012, pp. 210–215.

[37] S. Moitra and A. Mukhopadhyay, "Ku-band substrate integrated waveguide (siw) slot array antenna for next generation networks," *Global Journal of Computer Science and Technology: E Network, Web & Security*, vol. 13, pp. 11–15, Oct. 2013.

[38] X. Jiang, C. J. You, and Z. Shao, "A compact x-band circulator with embedded feed line based on substrate integrated waveguide," in *2013 International Conference on Computational Problem-Solving (ICCP)*, 2013, pp. 58–60.

[39] S. H. Shehab, N. C. Karmakar, and J. Walker, "Substrate-integrated-waveguide power dividers: An overview of the current technology," *IEEE Antennas and Propagation Magazine*, vol. 62, no. 4, pp. 27–38, 2020.

[40] W. Zhang, Z. Shen, K. Xu, and J. Shi, "A compact wideband phase shifter using slotted substrate integrated waveguide," *IEEE Microwave and Wireless Components Letters*, vol. 29, no. 12, pp. 767–770, 2019.

[41] A. Araghi, M. Khalily, O. Yurduseven, P. Xiao, and R. Tafazolli, "Guided-wave manipulation in siw h-plane horn antenna by combining phase correction and holographic-based leakage," *Scientific Reports*, vol. 12, Jul. 2022.

Appendices

A.1 MATLAB Code

A.1.1 SIW cutoff calculation

```
function cutoff

a=input('input the siw effective width (mm) = ');
d=input('input the siw vias diameter (mm) = ');
p=input('input the siw vias pitch (mm) = ');
epsilon=input('input the siw substrate epsilon = ');

c = 3e8;

R = (1.08*(d^2/p));
Q = (0.1*(d^2/a));

A = (a - R + Q)^-1;
B = c/(2*(epsilon^0.5));

fc = A*B*1e3

end
```

A.1.2 Multi-line calibration propagation constant extraction algorithm

```
function MultilineByGiorgos
clear all
close all
% Get the files
[fileName1,pathname]=uigetfile({'*.s2p'},'multilin calibration','
    shorter line','MultiSelect','off')
cd(pathname)
[fileName2,pathname]=uigetfile({'*.s2p'},'multilin calibration','
    longer line','MultiSelect','off')
```

```
8
9  % Get difference in length. give the value in meters
10 % because the differencce is defined as the (Ti - Tj)
11 % where "i" is the long length and "j" is the short
12 % in our case the "i" is the short length, "j" is the big length
13 % therefore we get positive input and make it negative
14 dl=-input('input the length difference (positive in mm) = ')/1000;
15
16 % wether S parameters are symmetrical (simulation case)
17 sSymm=input('whether the s-parameters are symmeterical? (0 no; 1
       Yes) = ');
18
19 % read the touchstone file, create s-parameter object
20 ts1_Small=sparameters(fileName1);
21 ts2_Long=sparameters(fileName2);
22
23
24 % Get the S-parameter data from s-parameter object "ts1" and "ts2"
25 sParam_Small = ts1_Small.Parameters;
26 sParam_Long = ts2_Long.Parameters;
27
28 s21_Long = rfparam(ts2_Long,2,1); % Extract the s21 data
29 s21_Long_mag = abs(s21_Long);
30 s21_Long_db = 20*log10(s21_Long_mag);
31
32
33 s11_Long = rfparam(ts2_Long,1,1); % Extract the s21 data
34 s11_Long_mag = abs(s11_Long);
35 s11_Long_db = 20*log10(s11_Long_mag);
36
37
38 % get the frequency data from s-parameter object "ts1"
39 freq=ts1_Small.Frequencies;
40
41 % get the number of frequency points
42 numberOfFrequencyPoints=numel(freq);
43
44
45 % get the cutoff frequency point "cutoff" - min operating frequency
46 fmin = 21700000000.0000;
47 linearIndices = find(freq>fmin);
48 cutoffPoint = linearIndices(1:1);
49
50 % maximum operating frequency point
51 fmax = 33000000000.0000;
52 point = find(freq<fmax);
53 maxPoint = max(point);
```

```
54
55 % equate s-parameters in case they are symmetrical
56 switch sSymm
57     case 1
58         for i=1:numberOfFrequencyPoints
59             sParam_Small(1,2,i) = sParam_Small(2,1,i);
60             sParam_Small(2,2,i) = sParam_Small(1,1,i);
61             sParam_Long(1,2,i) = sParam_Long(2,1,i);
62             sParam_Long(2,2,i) = sParam_Long(1,1,i);
63         end
64 end
65
66
67
68 % Convert to T-parameters from s-parameters
69 t1 = s2t(sParam_Small);
70 t2 = s2t(sParam_Long);
71
72 %Multiline_Extraction
73 % Tij = Ti*((Tj)^-1)
74 for j=1:numberOfFrequencyPoints
75     tij(:,:,j)=t1(:,:,j)*(inv(t2(:,:,j)));
76 end
77 % Eigenvalue of Tij = e^(?*?l)
78 for k=1:numberOfFrequencyPoints
79     lda(:,k)=eig(tij(:,:,k));
80 end
81 % Get the average of eigenvalues
82 for k=1:numberOfFrequencyPoints
83     lambda2(k)= 0.5*((lda(1,k))+(1/lda(2,k)));
84 end
85
86 % gamma calculation,  gamma = log(lambda)/Dl
87 gamma = log(lambda2)/(dl);
88
89 % attenuation constant in nepper/meter
90 alpha = real(gamma(1,:));
91
92 % attenuation constant in dB/meter
93 alpha_dB = 20*log10(exp(1))*alpha;
94
95 % phase constant in rad/meter
96 beta = unwrap(imag(gamma(1,:)));
97
98 wave_number = beta;
99
100 % get the alpha mean value in Np/meter for the operating range
```

```
    21-31 GHz
averageAlpha = mean(alpha(cutoffPoint:maxPoint))

% Lattice constant.
a = 4.56e-3;
c = 3e8;

Frequency = freq/1e9;



%Plot loss
figure(3)
plot(Frequency,alpha)
title("Attenuation constant")
xlabel('Frequency (GHz)','fontsize',16)
ylabel('Attenuation constant (nepper/m)','fontsize',16)
set(gca,'fontsize',12)
grid on


%Plot loss
figure(4)
plot(Frequency,alpha)
title("Attenuation constant operating range")
xlabel('Frequency (GHz)','fontsize',16)
ylabel('Attenuation constant (nepper/m)','fontsize',16)
 xlim([18 33])
 ylim([-7 10])

end
```

A.1.3 Guided Wavelength Calculation

```
function guidedWavelength


lowerFrequency=input('input the lower frequency in GHz = ')*10^9; %
    GHz


higherFrequency=input('input the higher frequency in GHz = ')*10^9;
     %GHz


lc = 2*(8.6)*10^-3; % mm
```

```
11
12 c = 299702547;
13
14 fmean = sqrt(lowerFrequency*higherFrequency);
15
16 lo = c/fmean;
17
18 b_part = (lo/lc)^2;
19
20 a_part = sqrt(1-b_part)
21
22 lguided = lo/a_part;
23
24
25 optimumLambdaG = lguided/4
26
27 end
```

A.1.4 Dielectric properties extraction of dielectric materials

```
1  function dielectricExtract2
2  % for this code the Rohde Swarz manual has been used for dielectric
3  % measurement using waveguide section method
4
5  clear all
6  close all
7  % Get the files
8  [fileName1,pathname]=uigetfile({'*.s2p'},'Select S-parameters file'
       )
9  cd(pathname)
10
11 lengthOfSample=input('input the length of sample in cm = ');
12 lc = 0.01728409;
13
14 % read the touchstone file, create s-parameter object
15 ts1=sparameters(fileName1);
16
17
18
19 % get the frequency data from s-parameter object "ts1"
20 freq=ts1.Frequencies;
21 numberOfFrequencyPoints=numel(freq);
22
23 l0 = 3e8./freq;
24
25
```

```
% get the number of frequency points


% get the s21 and s11 parameters in an array
s21 = rfparam(ts1,2,1);

s11 = rfparam(ts1,1,1);

s21_mag = abs(s21);
s21_db = 20*log10(s21_mag);

s11_mag = abs(s11);
s11_db = 20*log10(s11_mag);


Xvalue = ((s11_db.^2)-(s21_db.^2)+1)./(2.*s11_db);
complexOfgamma = Xvalue+sqrt(Xvalue.^2-1);
magOfGamma = abs(complexOfgamma);

for i=1:numberOfFrequencyPoints
    if magOfGamma(i) > 1
            complexOfgamma(i) = Xvalue(i)-sqrt(Xvalue(i)^2-1);
            magOfGamma(i) = abs(complexOfgamma(i));
     end
end

tValue = zeros(1,3201);

tValue = (s11_db+s21_db-complexOfgamma)./(1-((s11_db+s21_db).*
    complexOfgamma));


a = 1/2*pi*lengthOfSample;

b = log(1./tValue);

c = -(a.*b).^2;

e = sqrt(c);

d = (1+complexOfgamma)./(1-complexOfgamma);

p = sqrt((1./(l0.^2)) - (1/(lc^2)));


permeability = e.*d./p;

```

```
q = 1/lc;

h = 10.^2;

permittivity = h.*q.*c./permeability;


realPartPermitivity = real(permittivity) % dielectric constant

AvgDielectricConstant = mean(realPartPermitivity)

end
```

A.1.5 SIW Impedance Calculation

```
function siw_impedance
alpha=input('input the siw te10 width (mm) = ');
H=input('input the siw height(mm)= ');
epsilon=input('input the siw substrate epsilon = ');
d =1.2;
p = 2.6;
c = 3e8;
aeff10 = alpha-(d^2/(0.95*p));

R1 = (1.08*(d^2/p));
Q1 = (0.1*(d^2/alpha));

R2 = d^2/(1.1*p);
Q2 = 0.1*d^3/(6.6*p^2);

A1 = (alpha - R1 + Q1)^-1;
B1 = c/(2*(epsilon^0.5));

A2 = (alpha-R2+Q2)^-1;

%fc10 = A1*B1*1e3
%fc20 = A2*B1*2*1e3


fc10=input('input the siw te10 cutoff frequency (GHz = ');
fc20=input('input the siw te20 cutoff frequency (GHz = ');



h=377;

```

```
a=2*h*H;

g = (2*fc10/(1.25*fc10+0.95*fc20))^2;

b =(1-g)^-0.5;

c=epsilon^0.5*aeff10;

z =  a*b/c

end
```

A.1.6 Skin Depth calculation for conductive materials

```

function skinDepth

rho=input('input the resistivity (Ohm/m) = ');

mi_r=input('input the relative permeability = ');

f=input('input the injected frequency (GHz) = ');


pi = 3.1415926535897;
m0 = 4*pi*1e-7;

delta_s  = sqrt(rho/(pi*f*1e9*m0*mi_r))

end
```